Title

Machine Learning Towards Large-scale Atomistic Simulation and Materials Discovery

Author

Zuo, Yunxing

Publication Date

2021

UNIVERSITY OF CALIFORNIA SAN DIEGO

Machine Learning Towards Large-scale Atomistic Simulation and Materials Discovery

A dissertation submitted in partial satisfaction of the
requirements for the degree
Doctor of Philosophy

in

NanoEngineering

by

Yunxing Zuo

Committee in charge:

Professor Shyue Ping Ong, Chair
Professor Jian Luo
Professor Francesco Paesani
Professor Tod Pascal
Professor Yu Qiao

2021

The dissertation of Yunxing Zuo is approved, and it is acceptable in quality and form for publication on microfilm and electronically.

University of California San Diego

2021

DEDICATION

To my beloved family and friends.

TABLE OF CONTENTS

LIST OF FIGURES

LIST OF TABLES

ACKNOWLEDGEMENTS

I would like to express my utmost gratitude to my advisor, Prof. Shyue Ping Ong, for his guidance and support throughout my graduate studies. Your passion and visions towards addressing real scientific problems have inspired me and your high standards for scientific rigor and professionalism have enlightened me throughout my PhD. It is always enjoyable to have discussions with you and to listen to your talks. Your precious and constructive suggestions for my studies and career pursuits have encouraged me to step out of my comfort zone and address challenging problems.

I would like to give my special thanks to my first teacher in the Materials Virtual Lab (MAVRL), Dr. Chi Chen. Thank you for patiently teaching me how to improve my coding skills and critical thinking through working and daily discussion.

I am grateful to my collaborators in the MAVRL, Dr. Xiangguo Li, Hui Zheng, Ji Qi, Weike Ye, Dr. Zhi Deng, Yiming Chen. Many of the works in this thesis would not have been possible without your efforts. I am also grateful for the constructive discussion with collaborators, including Prof. Jian Luo, Dr. Chongze Hu and Dr. Mingde Qin from University of California, San Diego, Prof. Jörg Behler from Universität Göttingen, Prof. Gábor Csányi from University of Cambridge, Prof. Alexander Shapeev from Skolkovo Institute of Science and Technology, Dr. Aidan Thompson and Dr. Mitchell Wood from Sandia National Laboratories, Prof. Robert Richie, Prof. Mark Asta, and Dr. Sheng Yin from University of California, Berkeley, Prof. Hui Xiong and Dr. Pete Barnes from Boise State University.

For all the MAVRLers, thank you for making my graduate life so much fun and interesting.

Chapter 2, in full, is a reprint of the material ”Performance and cost assessment of machine learning interatomic potentials” as it appears on The Journal of Physical Chemistry A, Yunxing Zuo, Chi Chen, Xiangguo Li, Zhi Deng, Yiming Chen, Jörg Behler, Gábor Csányi, Alexander V. Shapeev, Aidan P. Thompson, Mitchell A. Wood, Shyue Ping Ong, 2020, 124 (4), 731-745. The dissertation author was the primary investigator and author of this paper.

Chapter 3, in full, is submitted for publication of the material ”Atomistic simulations of dislocation mobility in refractory high-entropy alloys and the effect of chemical short-range order”, Sheng Yin, Yunxing Zuo, Anas Abu-Odeh, Hui Zheng, Xiangguo Li, Jun Ding, Shyue Ping Ong, Mark Asta, Robert O. Ritchie. The dissertation author contributed to the machine learning interatomic potential development and was the co-first author of this paper.

Chapter 4, in full, is a reprint of the preprinted material ”Accelerating Materials Discovery with Bayesian Optimization and Graph Deep Learning” as it appears on Arxiv, Yunxing Zuo, Mingde Qin, Chi Chen, Weike Ye, Xiangguo Li, Jian Luo, Shyue Ping Ong. The dissertation author was the primary investigator and author of this paper.

VITA

2016	B. S. in Physics, Nankai University
2019	M. S. in NanoEngineering, University of California San Diego
2021	Ph. D. in NanoEngineering, University of California San Diego

PUBLICATIONS

1. **Yunxing Zuo**, Chi Chen, Xiangguo Li, Zhi Deng, Yiming Chen, Jörg Behler, Gábor Csányi, Alexander V. Shapeev, Aidan P. Thompson, Mitchell A. Wood, Shyue Ping Ong ”Performance and cost assessment of machine learning interatomic potentials”, The Journal of Physical Chemistry A, 2020, 124 (4), 731-745.

2. Sheng Yin*, **Yunxing Zuo***, Anas Abu-Odeh, Hui Zheng, Xiangguo Li, Jun Ding, Shyue Ping Ong, Mark Asta, Robert O. Ritchie ”Atomistic simulations of dislocation mobility in refractory high-entropy alloys and the effect of chemical short-range order”, submitted. (*These authors contributed equally)

3. **Yunxing Zuo***, Mingde Qin*, Chi Chen, Weike Ye, Xiangguo Li, Jian Luo, Shyue Ping Ong ”Accelerating Materials Discovery with Bayesian Optimization and Graph Deep Learning”, submitted. (*These authors contributed equally)

ABSTRACT OF THE DISSERTATION

Machine Learning Towards Large-scale Atomistic Simulation and Materials Discovery

by

Yunxing Zuo

Doctor of Philosophy in NanoEngineering

University of California San Diego, 2021

Professor Shyue Ping Ong, Chair

In materials science, the first principles modeling, especially density functional theory (DFT), serves as the *de facto* tool in studying physical phenomena and properties of materials from the atomistic level. However, the high computational cost and poor scaling of DFT has limited its applications in two important scientific problems — large-scale atomistic simulations and high-throughput screening for materials discovery. This thesis demonstrates how the machine learning (ML) techniques enable atomistic simulations in large size and time scale with DFT-accuracy and accelerate materials discovery with the state-of-the-art graph neural network models. This thesis is divided into two topics.

In the first topic (Chapters 2 and 3), we will investigate how the machine learning interatomic potentials (ML-IAPs) are trained and provide a systematic assessment of the cost and accuracy performances for several major ML-IAPs. We have also implemented high-level Python interfaces for ML-IAPs development and materials properties calculators using a molecular dynamic (MD) engine. This toolkit enabled us to develop a highly accurate and efficient ML-IAP for refractory high-entropy alloy NbMoTaW, an important alloy system yielding exceptional mechanical properties under high temperature. We will demonstrate how the ML-IAP driven atomistic simulations help us understand the mobility of edge/screw dislocations with the presence of short-range order (SRO).

In the second topic (Chapter 4), we developed a Bayesian Optimization With Symmetry Relaxation (BOWSR) algorithm using MatErials Graph Network (MEGNet) energy model to obtain equilibrium crystal structures, bypassing the high-cost DFT relaxations. The BOWSR algorithm enabled us to screen $\sim$ 400,000 transition metal borides and carbides for ultra-incompressible hard materials. Attempts were made to synthesize the top ten candidates with the highest computed bulk modulus with eight unique compositions, and two new crystals yielding ultra-incompressibility were successfully synthesized.

Chapter 1

Introduction

1.1 Background

Materials design, including known materials optimization and new materials discovery, is among the most important subjects in materials science. For the past decades, the growing computational resources and the well-established quantum mechanical approximations to the Schrödinger's equation, in particular density functional theory (DFT)[1,2], has enabled the researchers to predict the physical and chemical properties of materials *in silico* and virtually guide the experimental efforts, in place of the historical trial-and-errors mode.

Despite the promising perspective of "virtual materials design" driven by the DFT, its high cost and poor scalability with the increase of number of electrons (typically $O(n_e^3)$ or higher)[3–5] fundamentally limits the simulations to ~ 1000 atoms and hundreds of picoseconds, even with the modern supercomputing power. In effect, this has hindered the development of two aspects of materials design. On the one hand, the optimization of known materials demands large-scale simulations for realistic systems far beyond ~ 1000 atoms, such as enhancing strength of alloys[6,7] and understanding diffusion mechanism of solid electrolytes[8**?**] . On the other hand, the chemistries and structures search spaces for new materials discovery are significantly constrained using the traditional high-throughput screening with DFT[9,10].

Recently, machine learning (ML) has emerged as a transformative paradigm in materials science[11,12]. The large materials data allow the ML models to learn the relationship between the materials descriptors and targets and thus enable the rapid property predictions for the unexplored space of materials without solving the Schrödinger's equation.

In this chapter, we first discuss the learning targets in materials optimization, especially the important role of ML models in large-scale atomistic simulation required for understanding and optimizing the properties of materials under various experimental conditions. Then, we analyze the strengths and weaknesses of the popular ML models for accurate materials property predictions and their potential application in new materials discovery. Finally, we conclude with the objectives and overview of this thesis.

1.2 Materials optimization

For the known materials to surpass the current performance, one strategy is optimizing the constituents and working conditions of the materials[13–16]. From an atomistic point of view, this generally requires large-scale simulations for realistic systems with $\sim O(10^5 - 10^6)$ atoms that are computationally intractable using DFT. Therefore, the molecular dynamic (MD) simulation coupled with empirical interatomic potentials (IAPs) emerged to address this problem for many common systems[17–22]. The empirical IAPs are typically parameterizations of the experimental or calculated observables based on physical functional forms and have linear scaling with respect to the number of atoms. Although the empirical IAPs have been widely used in large-scale simulations, their predictions are qualitative at best[23–25].

Recently, the development of ML algorithms coupled with atomic descriptors[26–31] has given rise to the surge of machine learning interatomic potentials (ML-IAPs). In principle, the potential energy surface (PES) of the material is described as a function of the local environment descriptors that are invariant to rotation, translation, and permutation of homonuclear atoms,[28,32] as shown in Fig. 1.1. The local environment descriptors for each central atom in the system encodes the information of neighboring atoms within the cutoff radius by incorporating their distances to the central atom and the angles formed in triplets that include the central atom and neighboring atoms. The ML model is then applied to learn the relationship between the descriptors and the targets, generally the DFT-calculated energy and atomic forces. Presumably, a well-performed ML-IAP can be used to simulate arbitrary atomic configurations (e.g., amorphous[33,34] and interfaces[35]) within the PES provided that the training data set covers a diverse space of atomic local environments. The ML-IAPs have shown remarkable improvement over the empirical IAPs in terms of achieving near-DFT accuracy at the linear scaling cost.

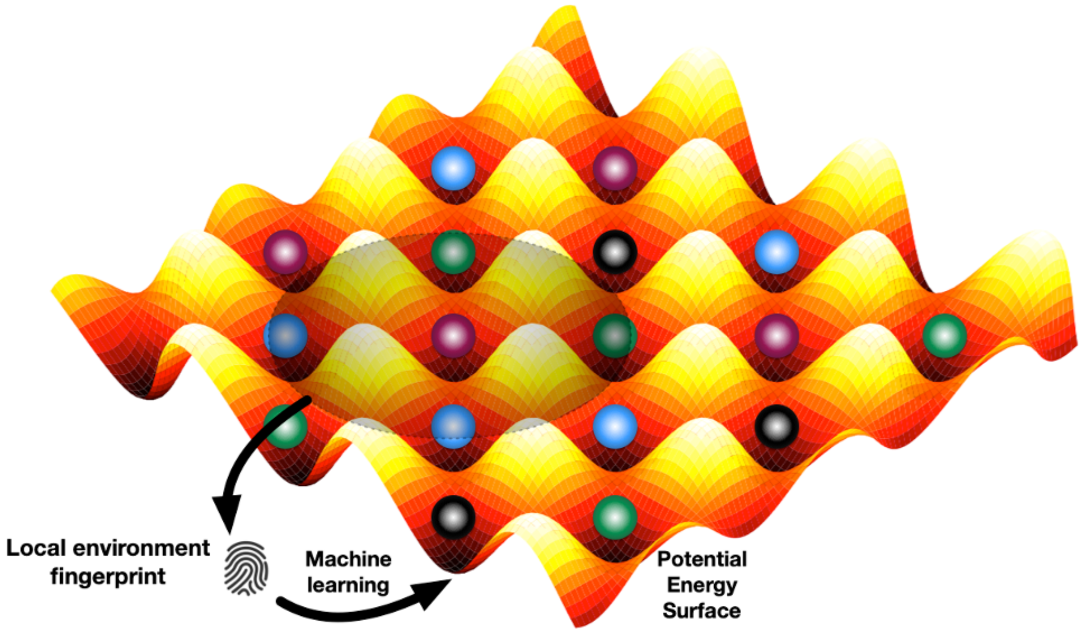

Figure 1.1: Schematic illustration of the PES and the mechanisms of ML-IAPs to approximate the PES.

There have been extensive studies on the development of ML-IAPs. Major ML-IAPs include neural network potential (NNP)[36,37], the Gaussian approximation potential (GAP)[28,38,39], the Spectral Neighbor Analysis Potential (SNAP)[30,40–42], moment tensor potentials (MTP),[29,43,44], deep potential (DP)[45] and etc. These ML-IAPs have shown great performance in understanding and optimizing the materials properties for various applications such as catalytic[35,46] and structural[7,47] and energy materials.[48]

1.3 Materials discovery

Another important aspect of materials design is new materials discovery. The process can be generally split into two steps: crystal structure generation and property predictions. Crystal structures can be generated through various strategies. While previous works show that heuristic methods such as evolutionary algorithm[49] and particle swarm optimization[50] are capable of identifying novel crystal structures, a dominant strategy of deriving new compounds comes from chemical substitution to the known structure prototypes[9,51,52], which is commonly used in high-throughput screening approach[53,54]. Recent development of ML generative algorithm has motivated the "inverse design" of new crystal structures[55,56] and attracted widespread interest.

For property predictions, DFT methods have been long considered as the *de facto* tools due to their high accuracy and transferability. However, the high cost and poor scaling of DFT have limited their broad application across vast chemistries and structures and confined the exploration space of traditional high-throughput screening for materials discovery. To date, numerous collective efforts have been made to assemble DFT-computed properties for over 10^5 known and hypothetical compounds[57–59]. Albeit, these are far from adequate compared to the gigantic unexplored chemical space ($\sim 10^{60}$). To address this challenge, ML has emerged as a new paradigm for developing efficient surrogate models for predicting materials properties at scale.

Among all of the materials properties, the formation energy is the most fundamental one as it is the key metric for the stability or synthesizability of a compound[52,60,61]. Hence, the development of surrogate ML models demands accurate predictions on formation energies, at the minimum. These ML models were usually trained on large databases[57–59] and can be divided into two categories. The models that take chemical compositions as input have shown relatively high accuracy over a broad range of structure prototypes[62–64]. However, the lack of structural information limits their application in distinguishing between polymorphs for the same composition. As a result, these models are poorly suited for materials discovery within specific chemical spaces. Recent advances of graph neural networks[65] give rise to the development of graph-based models for accurate property predictions for molecules[66–69] and crystals[70–72]. In particular, these models interpret the molecular or crystal structures by nodes and edges representing atoms and bonds, respectively. Training on the Materials Project database[57], the graph-based models have shown state-of-the-art performance in prediction of various materials properties[70–72].

1.4 Objectives

Despite the increasingly important role ML plays in materials design, major gaps remain in ML-IAPs for materials optimization and graph-based ML models for materials discovery. The blossom of different ML-IAPs provides multiple options for interested researchers and practitioners. However, the relative strengths and weaknesses of different ML-IAPs remain poorly assessed. The evaluation of the performances (e.g., accuracy and computational cost) of major ML-IAPs and the factors that determine these performances may provide a useful guideline in choosing different ML-IAPs for different applications. Moreover, ML-IAPs for the optimization of multiple-component systems (e.g., high-entropy alloys) remain rarely developed due to the demand of exponentially larger amount of training data.

Although the graph-based models have shown significantly high accuracy suited for targeted materials discovery, paradoxically, these models typically require accurate crystal structures, either from experimental measurements or DFT relaxations, as input. This requirement fundamentally limits the scope of application of these surrogates to well-explored chemical space as the relaxed crystal structures of hypothetical materials are unknown without DFT relaxations.

In this thesis, we attempt to address these gaps for both materials optimization and discovery. The thesis is divided into two topics. In the first topic, we will demonstrate a systematic assessment of accuracy and computational cost for the major ML-IAPs using a standardized data set. We also implemented high-level Python interfaces for seamless ML-IAPs development and materials property predictions. Using this toolkit, we developed a well-performed general-purpose ML-IAP for refractory high-entropy alloy system NbMoTaW. In the second topic, we propose the Bayesian Optimization With Symmetry Relaxation (BOWSR) algorithm for "DFT-free" relaxation of crystal structures using MatErials Graph Network (MEGNet) as energy estimator, breaking through the limitations of graph-based models in materials discovery. A brief description for each subsequent chapter is provided as follows:

- Chapter 2 presents an impartial comparison between four major ML-IAPs from several aspects: accuracy, data requirement, and computational cost. We also analyzed the factors that may determine their relative strengths and weaknesses and extended the concept of Pareto frontier in terms of accuracy and cost for ML-IAPs assessment.

- Chapter 3 presents a study on mechanism of plastic deformation of *bcc* refractory high-entropy alloy (RHEA) system MoNbTaW driven by ML-IAPs. The ML-IAP enabled us to perform MD simulations of over 500,000 atoms for understanding the mobility of edge/screw dislocation with respect to temperature and the presence of short-range order (SRO).

- Chapter 4 presents an algorithmic effort in developing BOWSR for crystal structure relaxation, bypassing the high-cost DFT. We showcased that BOWSR algorithm and the MEGNet models enabled us to identify eight new candidates out of $\sim$400,000 transition metal borides and carbides for ultra-incompressible hard materials. Two of them were successfully synthesized via *in-situ* reactive spark plasma sintering (SPS).

Chapter 2

Performance and cost assessment of machine learning interatomic potentials

2.1 Introduction

A fundamental input for atomistic simulations of materials is a description of the potential energy surface (PES) as a function of atomic positions. While quantum mechanics-based descriptions, such as those based on Kohn-Sham density functional theory (DFT)[2,73], are accurate and transferable across chemistries, their high cost and poor scaling (typically $O(n_e^3)$ or higher, where n_e is the number of electrons)[3–5] limits simulations to ~ 1000 atoms and hundreds of picoseconds. Hence, large-scale and long-time simulations traditionally rely on interatomic potentials (IAPs), which to date are in most cases empirical parameterizations of the PES based on physical functional forms that depend only on the atomic degrees of freedom.[18–20] IAPs gain linear scaling with respect to the number of atoms at the cost of accuracy and transferability.

In recent years, a modern alternative has emerged in the form of machine-learned IAPs (ML-IAPs), where the PES is described as a function of local environment descriptors that are invariant to translation, rotation and permutation of homonuclear atoms[28,32]. Examples of such potentials include the high-dimensional neural network potential (NNP)[36,37], the Gaussian approximation potential (GAP)[28,38,39], the Spectral Neighbor Analysis Potential (SNAP)[30,40–42], moment tensor potentials (MTP),[29,43,44] among others[74–79]. A typical approach to training such potentials involves the generation of a sufficiently large and diverse data set of atomic configurations with corresponding energies, forces and stresses from DFT calculations, which are then used in the training of the ML-IAP based on one or several target metrics, such as minimizing the mean absolute or squared errors in predicted energies, forces, stresses or derived properties (e.g. elastic constants). ML-IAPs have been shown to be a remarkable improvement over traditional IAPs, in general, achieving near-DFT accuracy in predicting energies and forces across diverse chemistries and atomic configurations. Despite the fact that recent benchmark efforts[80–82] have demonstrated the remarkable performance of ML-IAPs, a critical gap that remains is a rigorous assessment of the relative strengths and weaknesses of ML-IAPs across a standardized data set, similar to what has been done for classical IAPs.[83–85].

In this work, we present a comprehensive performance comparison of four major ML-IAPs — GAP, MTP, NNP and SNAP. The four IAPs were evaluated in terms of their accuracy in reproducing DFT energies and forces, as well as material properties such as the equations of state, lattice parameter and elastic constants. An attempt was also made to assess the training data requirements of each ML-IAP and the relative computational cost based on the best-available current implementations. To ensure a fair comparison, standardized DFT data sets of six elements (Li, Mo, Cu, Ni, Si and Ge) with the same training/test sampling and similar fitting approaches were used. The elements were chosen to span diverse chemistries and bonding, e.g., bcc and fcc metals, main group and transition metals, and group IV semiconductors.

2.2 Methods

2.2.1 Machine learning interatomic potentials

The four ML-IAPs investigated in this work have already been extensively discussed in previous works and reviews[28–30,32,36–44,86–89]. All ML-IAPs express the potential energy as a sum of atomic energies that are a function of the local environment around each atom, but differ in the descriptors for these local environments and the ML approach/functional expression used to map the descriptors to the potential energy. The detailed formalism of all four ML-IAPs are provided in the Supplementary Information. Here, only a concise summary of the key concepts and model parameters behind the ML-IAPs in chronological order of development is provided to aid the reader in following the remainder of this paper.

1. **High-dimensional neural network potential (NNP).** The NNP uses atom-centered symmetry functions (ACSF)[26] to represent the atomic local environments and fully connected neural networks to describe the PES with respect to symmetry functions[36,37]. A separate

neural network is used for each atom and each neural network processes the symmetry functions from local environments of the corresponding atom and outputs its atomic energy. The architecture of the neural network is defined by the number of hidden layers and the nodes in each layer, while the descriptor space is given by the following symmetry functions:

$$\begin{aligned} G_i^{\text{atom,rad}} &= \sum_{j\neq i}^{N_{\text{atom}}} e^{-\eta(R_{ij}-R_s)^2} \cdot f_c(R_{ij}), \\ G_i^{\text{atom,ang}} &= 2^{1-\zeta} \sum_{j,k\neq i}^{N_{\text{atom}}} (1+\lambda\cos\theta_{ijk})^{\zeta} \cdot e^{-\eta'(R_{ij}^2+R_{ik}^2+R_{jk}^2)} \cdot f_c(R_{ij}) \cdot f_c(R_{ik}) \cdot f_c(R_{jk}), \end{aligned}$$

where R_{ij} is the distance between atom i and neighbor atom j, η is the width of the Gaussian and R_s is the position shift over all neighboring atoms within the cutoff radius R_c, η' is the width of the Gaussian basis and ζ controls the angular resolution. $f_c(R_{ij})$ is a cutoff function, defined as follows:

$$f_c(R_{ij}) = \begin{cases} 0.5 \cdot [\cos(\frac{\pi R_{ij}}{R_c}) + 1], & \text{for } R_{ij} \leq R_c \\ 0.0, & \text{for } R_{ij} > R_c. \end{cases} \tag{2.1}$$

These hyperparameters were optimized to minimize the root-mean- square errors of energies and forces for each chemistry. The NNP model has shown great performance for Si[36], TiO_2[90], water[91] and solid-liquid interfaces[46], metal-organic frameworks[92], and has been extended to incorporate long-range electrostatics for ionic systems such as ZnO[93] and Li_3PO_4[94].

2. **Gaussian Approximation Potential (GAP).** The GAP calculates the similarity between atomic configurations based on a smooth-overlap of atomic positions (SOAP)[27,28] kernel, which is then used in a Gaussian process model. In SOAP, the Gaussian-smeared atomic

neighbor densities $\rho_i(R)$ are expanded in spherical harmonics as follows:

$$\rho_i(R) = \sum_j f_c(R_{ij}) \cdot \exp(-\frac{|R - R_{ij}|^2}{2\sigma_{\text{atom}}^2}) = \sum_{nlm} c_{nlm}\, g_n(R) Y_{lm}(\hat{R}), \tag{2.2}$$

The spherical power spectrum vector, which is in turn the square of expansion coefficients,

$$p_{n_1 n_2 l}(R_i) = \sum_{m=-l}^{l} c_{n_1 lm}^* c_{n_2 lm}, \tag{2.3}$$

can be used to construct the SOAP kernel while raised to a positive integer power ζ to accentuate the sensitivity of the kernel[28],

$$K(R, R') = \sum_{n_1 n_2 l} (p_{n_1 n_2 l}(R) p_{n_1 n_2 l}(R'))^{\zeta}, \tag{2.4}$$

In the above equations, σ_{atom} is a smoothness controlling the Gaussian smearing, and $n_{\max}$ and $l_{\max}$ determine the maximum powers for radial components and angular components in spherical harmonics expansion, respectively[28]. These hyperparameters, as well as the number of reference atomic configurations used in Gaussian process, are optimized in the fitting procedure to obtain optimal performance. The GAP has been developed for transition metals[38,39], main group elements[33,95,96], diamond semiconductors[34,97] as well as multi-component systems[88].

3. **Spectral Neighbor Analysis Potential (SNAP).** The SNAP uses the coefficients of the bispectrum of the atomic neighbor density functions[28] as descriptors. In the original formulation of SNAP, a linear model between energies and bispectrum components is assumed[30]. Recently, a quadratic model (denoted as qSNAP in this work)[98] has been developed, which extends the linear SNAP energy model to include all distinct pairwise products of bispectrum components. In this work, both linear and quadratic SNAP models were investigated. The critical hyperparameters influencing model performance are the

cutoff radius and $J_{\max}$, which limits the indices j_1, j_2, j in Clebsch-Gordan coupling coefficients $H^{jmm'}_{\substack{j_1 m_1 m'_1 \\ j_2 m_2 m'_2}}$ in construction of the bispectrum components:

$$\begin{aligned} B_{j_1,j_2,j} = &\sum_{m_1,m'_1=-j_1}^{j_1} \sum_{m_2,m'_2=-j_2}^{j_2} \sum_{m,m'=-j}^{j} (u^j_{m,m'})^* \\ &\times H^{jmm'}_{\substack{j_1 m_1 m'_1 \\ j_2 m_2 m'_2}} u^{j_1}_{m_1,m'_1} u^{j_2}_{m_2,m'_2}, \end{aligned} \tag{2.5}$$

where $u^j_{m,m'}$ are coefficients in 4-dimensional hyper-spherical harmonics expansion of neighbor density function:

$$\rho_i(\mathbf{R}) = \sum_{j=0}^{\infty} \sum_{m,m'=-j}^{j} u^j_{m,m'} U^j_{m,m'}, \tag{2.6}$$

The SNAP model as well as qSNAP model has demonstrated great success in transition metals[30,40,41,98] as well as binary systems[41,42,89].

4. **Moment Tensor Potential (MTP)**. The MTP[29] devises rotationally-covariant tensors

$$M_{\mu,\nu}(R) = \sum_j f_\mu(R_{ij}) \underbrace{R_{ij} \otimes \cdots \otimes R_{ij}}_{\nu \ times}, \tag{2.7}$$

to describe the atomic local environments. Here f_μ are the radial functions, and $R_{ij} \otimes \cdots \otimes R_{ij}$ are tensors of rank ν encoding angular information about the atomic environment. The rank ν can be large enough to approximate any arbitrary interactions. MTP then contracts these tensors to a scalar that yields rotationally-invariant basis functions, and applies linear regression to correlate the energies with the basis functions. The performance of MTP is controlled by the polynomial power-like metric, which defines what tensors and how many times are contracted. The MTP model has been successfully applied to metals[29,43,99], boron[100], binary and ternary alloys[44] as well as gas-phase chemical reactions[101].

2.2.2 DFT data sets

A comprehensive DFT data set was generated for six elements - Li, Mo, Ni, Cu, Si and Ge. These elements were chosen to span a variety of chemistries (main group metal, transition metal and semiconductor), crystal structures (bcc, fcc, and diamond) and bonding types (metallic and covalent). For each element, we generated a set of structures with diverse coverage of atomic local environment space, as follows:

(1) The ground-state crystal for each element.

(2) Strained structures constructed by applying strains of -10% to 10% at 2% intervals to the bulk supercell in six different modes, as described in the previous work[102]. The supercells used are the $3 \times 3 \times 3$, $3 \times 3 \times 3$ and $2 \times 2 \times 2$ of the conventional bcc, fcc and diamond unit cells, respectively.

(3) Slab structures up to a maximum Miller index of three, including (100), (110), (111), (210), (211), (310), (311), (320), (321), (322), (331), and (332), as obtained from the Crystalium database[103,104].

(4) *NVT ab initio* molecular dynamics (AIMD) simulations of the bulk supercells (similar to those in (2)) performed at 300 K and 0.5×, 0.9×, 1.5×, 2.0× of the melting point of each element with a time step of 2 fs. The bulk supercells were heated from 0 K to the target temperatures and equilibrated for 20,000 time steps. A total of 20 snapshots were obtained from the subsequent production run in each AIMD simulation at an interval of 0.1 ps. The radial distribution function (RDF) analysis confirms that the structures obtained from AIMD simulations above melting point are liquid-like in the atomic environments (see Figure A.1).

(5) *NVT* AIMD simulations of the bulk supercells (similar to those in (2)) with a single vacancy performed at 300 K and 2.0× of the melting point of each element. The bulk supercells

were heated from 0 K to the target temperatures and equilibrated for 20,000 time steps. A total of 40 snapshots were obtained from the subsequent production run of each AIMD simulation at an interval of 0.1 ps.

All DFT calculations were carried out using the Vienna *ab initio* simulation package (VASP)[105] version 5.4.1 within the projector augmented wave approach[106]. The Perdew-Burke-Ernzerhof (PBE) generalized gradient approximation (GGA)[107] was adopted for the exchange-correlation functional. The kinetic-energy cutoff was set to 520 eV and the *k*-point mesh was $4 \times 4 \times 4$ for the Mo, Ni, Cu, Si and Ge supercells, and $3 \times 3 \times 3$ for the Li supercells. The electronic energy and atomic force components were converged to within 10^{-5} eV and 0.02 eV/Å, respectively, in line with previous works[40,41]. The AIMD simulations were carried out with a single Γ *k* point and were non-spin-polarized, but static calculations using the same parameters as the rest of the data were carried out on the snapshots to obtain consistent energies and forces. All structure manipulations and analyses of DFT computations were carried out using Python Materials Genomics (Pymatgen)[108] library, and the automation of calculations was performed using the Fireworks software[109].

2.2.3 Optimization scheme

Figure 2.1 provides an overview of the general data generation and potential development scheme. The training data set was first generated via DFT static calculations on the four categories of structures. The optimization procedure comprised two loops. In the inner loop, sampled structures in the database were transformed into atomic descriptors (e.g., bispectrum components for SNAP and symmetry functions for NNP), which were then fed into the corresponding ML model together with the DFT energies, forces, and stresses as the targets of training. The data was apportioned into training and test sets with a 90:10 split. The parameters of the ML models were optimized during the training process. In the outer loop, the ML model trained in the inner loop was used to predict basic material properties (e.g., elastic tensors), and the differences between the predicted and reference values were then used to determine the optimal hyperparameters for each ML-IAPs. In this work, we adopted a combination of the grid search algorithm and differential evolution algorithm to perform hyperparameters optimization for different ML-IAPs.

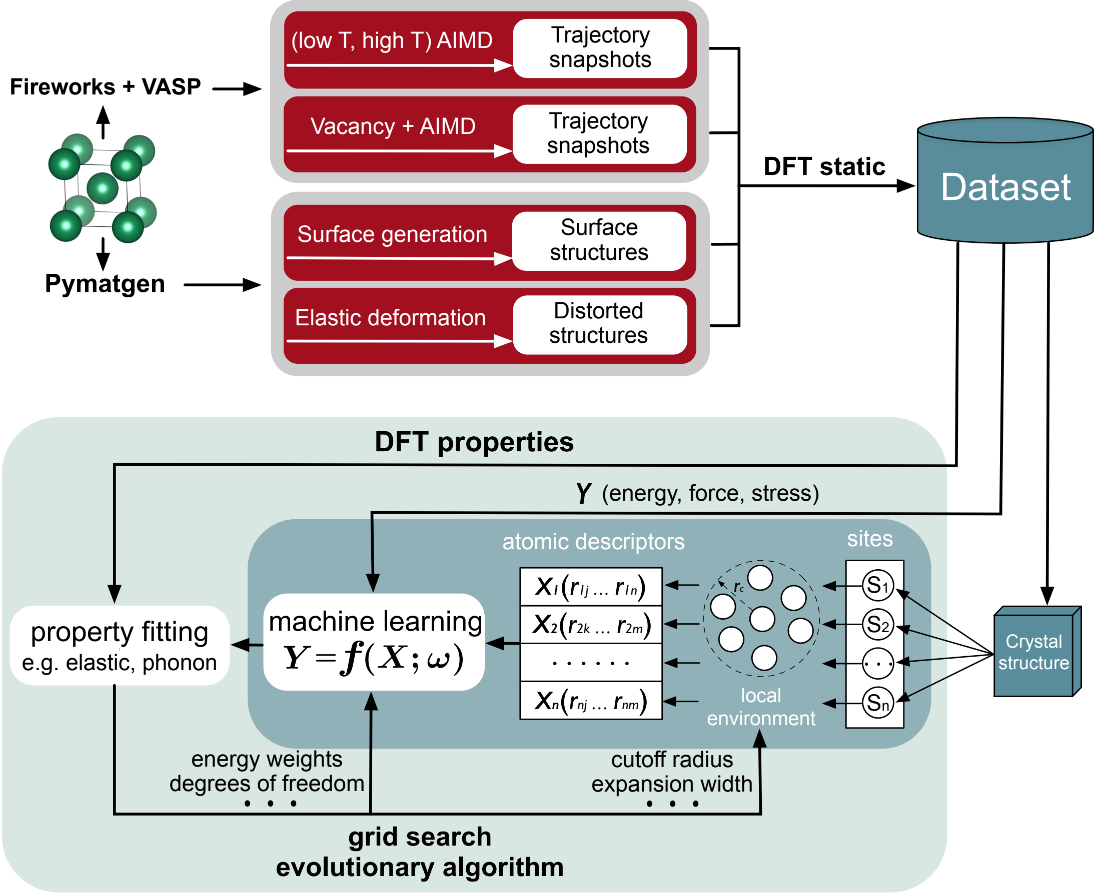

Figure 2.1: Machine-learning interatomic potential development workflow.

2.3 Results

2.3.1 Optimized model parameters

Here, we will limit our discussions to a parameter that is common to all ML-IAPs - the cutoff radius - and present a convergence study of each ML-IAP with the number of degrees of freedom of the model.

Table 2.1: Optimized cutoff radius for each element for each ML-IAP.

	fcc		**bcc**		**diamond**	
cutoff radius (Å)	Ni	Cu	Li	Mo	Si	Ge
GAP	3.9	3.9	4.8	5.2	5.4	5.4
MTP	4.0	3.9	5.1	5.2	4.7	5.1
NNP	3.9	4.1	5.2	5.2	5.5	5.6
SNAP	4.1	4.1	5.1	4.6	4.9	5.5
qSNAP	3.8	3.9	5.1	5.2	4.8	4.9

The cutoff radius determines the maximum range of interatomic interactions, and hence, has a critical effect on the prediction performance of ML-IAPs. Table 2.1 provides the optimized cutoff radii of different ML-IAPs across different chemistries. Different ML-IAPs yield similar optimized cutoff radii for the same elemental system. The optimized cutoff radii are between the second nearest neighbor (2NN) and 3NN distance for fcc elements (Cu, Ni), between 3NN and 4NN distances for the bcc (Li, Mo) and diamond (Ge and Si) elements. These observations are consistent with those from previous traditional and ML IAP development efforts, where typically 2NN interactions are found to suffice for fcc metals,[110,111] while contributions from 3NN cannot be ignored for bcc metals[29,38,43,112,113] and diamond systems[114,115].

The number of degrees of freedom (DOF), e.g., the number of weights and biases for the NNP and number of representative points in GAP, has a strong effect on the accuracy and computational cost of each ML-IAP. Figure 2.2 illustrates the trade-off between computational cost and test error under varying DOFs for each fitted Mo ML-IAP. It should be noted that the relative computational costs are based on the most efficient available implementations[28–30,98,116] of each ML-IAP at this time in LAMMPS[17] and performed on a single CPU core of Intel i7-6850k 3.6 GHz with 18 × 18 × 18 bulk supercell containing 11,664 atoms for Mo system. Future implementations and optimizations, such as to the evaluation of the local environment descriptor, may improve on these results, as discussed in a recent work[117]. A dashed Pareto frontier is drawn in Figure 2.2a to represent points at which better accuracy can only be attained at the price of greater computational cost[118] and the black arrows indicate "optimal" configurations for each model in terms of the trade-off between test error and computational cost. These "optimal" configurations were used for subsequent accuracy comparisons in energies, forces and properties. We find that the "optimal" MTP, NNP, SNAP and qSNAP models tend to be two orders of magnitude less computationally expensive than the "optimal" GAP model. The MTP models generally lie close to the Pareto frontier, exhibiting an excellent balance between model accuracy and computational efficiency. For the SNAP and qSNAP models, the descriptor space (i.e., bispectrum components) is determined by the parameter $J_{\max}$. We find that the rate-limiting step is the calculation of bispectrum and the computation of quadratic terms in qSNAP has only a marginal effect on the computational cost.[98]. However, we find that the substantial expansion in the number of DOF in the qSNAP model leads to over-fitting for larger values of $J_{\max}$ (see Figure 2.2b), which can be attributed to the large number of fitted coefficients of its formalism. For the GAP model, the computational cost is linearly related to the number of kernels used in Gaussian process regression.[38]. It should be noted that classical IAPs remain substantially lower in computational cost than ML-IAPs by 2-3 orders of magnitude.

2.3.2 Accuracy in energies and forces

Figure 2.3 provides a comparison of the root-mean-square errors (RMSEs) in energies and forces for the four ML-IAPs and best-available classical IAPs relative to DFT. All ML-IAPs show extremely good performance across all elements studied, achieving RMSEs in energies and forces that are far lower than best-available traditional IAPs for each element. It should be noted that differences in RMSEs between ML-IAPs are on the scale of meV atom^{-1} in energies and 0.1 eV Å^{-1} in forces; hence, any subsequent discussion on the relative performances of the ML-IAPs should be viewed in the context that even the largest differences in accuracy between the ML-IAPs

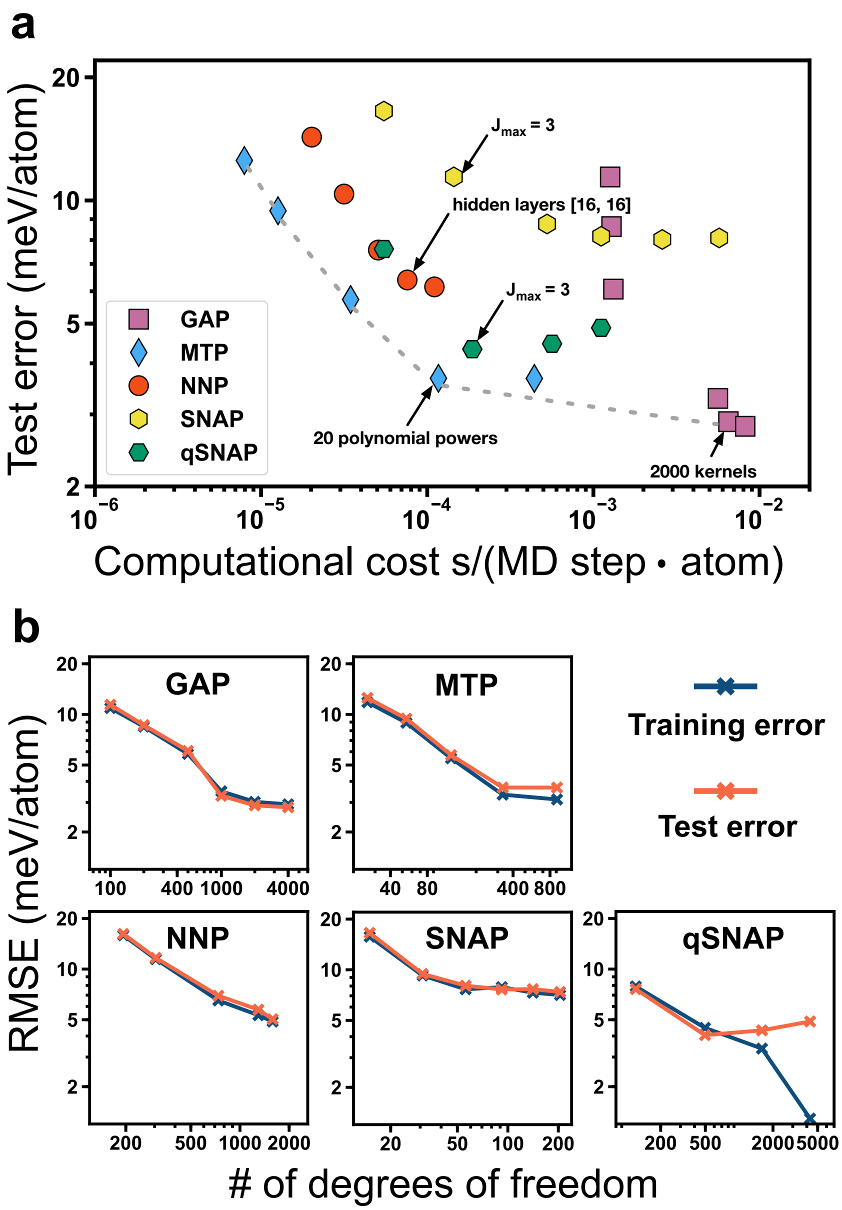

Figure 2.2: Trade-offs between accuracy and computational cost for ML-IAPs. (a) Test error versus computational cost for the Mo system. The grey dashed line indicates an approximate Pareto frontier formed by the convex hull of points lying on the bottom left of the chart. This Pareto frontier represents an optimal trade-off between accuracy and computational cost. Timings were performed by LAMMPS calculations on a single CPU core of Intel i7-6850k 3.6 GHz. Black arrows denote the "optimal" configuration for each ML-IAP that was used in subsequent comparisons. (b) Plots of the training and test errors versus the number of degrees of freedom for each ML-IAP.

are already close to the limits of DFT error. In all cases, the training and test errors are similar, indicating no over-fitting for the optimized ML-IAPs. The energy and force errors of ML-IAPs are marginally larger than those reported in a recent work[119] on Cu and Ge. However, this is likely due to the fact that the data in this work contains a diverse range of structures sampled from AIMD simulations at a much larger time intervals (0.1 ps vs 10 fs in the previous work) as well as strained structures, surface structures and vacancy-containing structures.

The GAP and MTP models generally have the lowest RMSEs in energies and forces. The highest RMSEs in energies are observed for the SNAP models and NNP models. It is well-known that neural network-based models often require larger data sets for best performance; previous NNP models have been trained on thousands or tens of thousands of structures[80,120], while only hundreds of structures are used in training the current ML-IAPs. Nevertheless, the NNP models still show surprisingly good performance for bcc systems. The qSNAP models' performances are between those of the GAP and NNP. In general, the qSNAP models have moderately lower RMSEs than the linear SNAP, though at the expense of a large expansion in the number of parameters.

In terms of chemistries, we find that the lowest RMSEs in energies are observed for the fcc systems, followed by the bcc systems, and the highest RMSEs are observed for the diamond systems. Very low RMSEs in forces are observed across all ML-IAPs for Cu, Ni and Li, while relatively higher RMSEs in forces are observed for Mo, a metal with higher modulus and larger force distributions. Higher RMSEs in forces are also observed for the diamond semiconductors. These trends are generally consistent across all ML-IAPs studied. The RMSEs normalized to the ground state energy per atom for each element is given in Figure A.2) further supports the better accuracy for the metals (both fcc and bcc) relative to the diamond systems, and the much better performance of the ML-IAPs over the classical IAPs.

We have also performed a study of the convergence of the ML-IAPs with training data size using Mo as the benchmark system given that it is a bcc metal (for which traditional IAPs

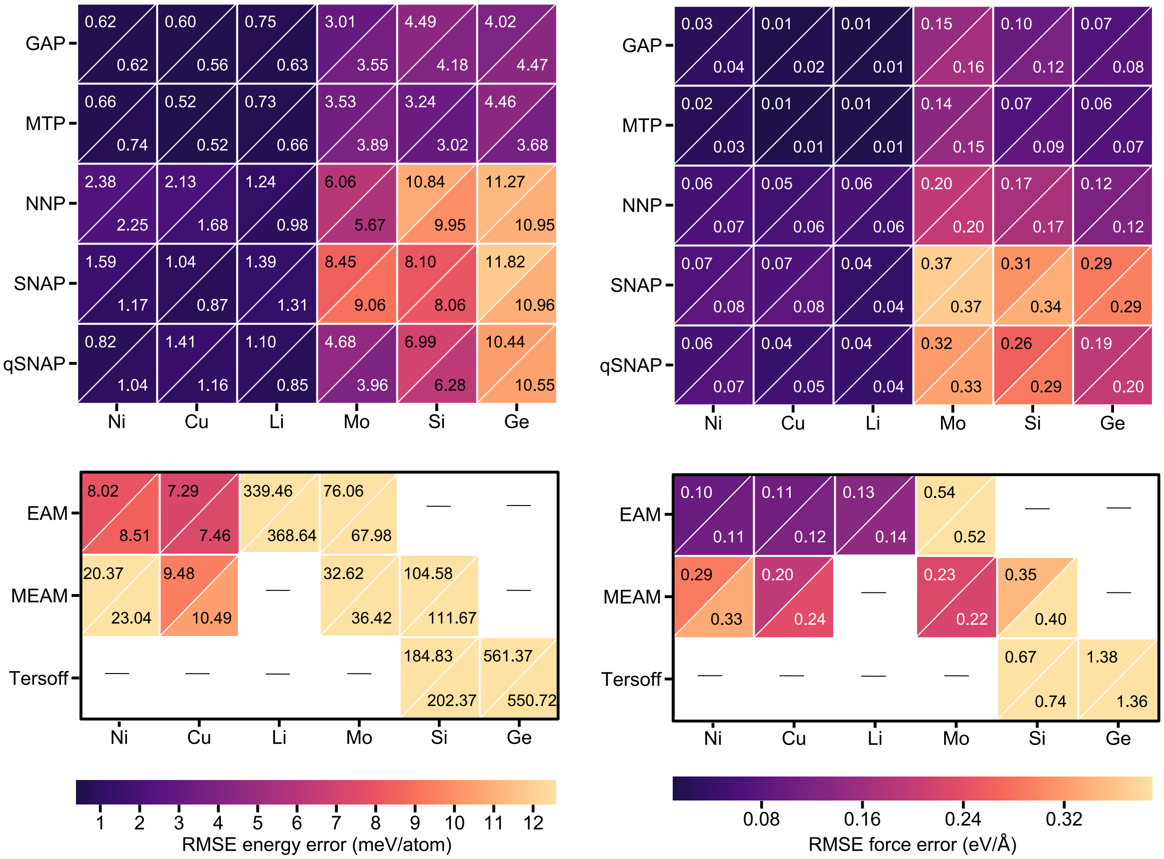

Figure 2.3: Root-mean-square errors in (a) predicted energies (b) predicted forces for all four ML-IAPs as well as traditional IAPs (EAM[121,122], MEAM[123–125], Tersoff[126,127]). The upper left and lower right triangles within each cell represent training and test errors, respectively.

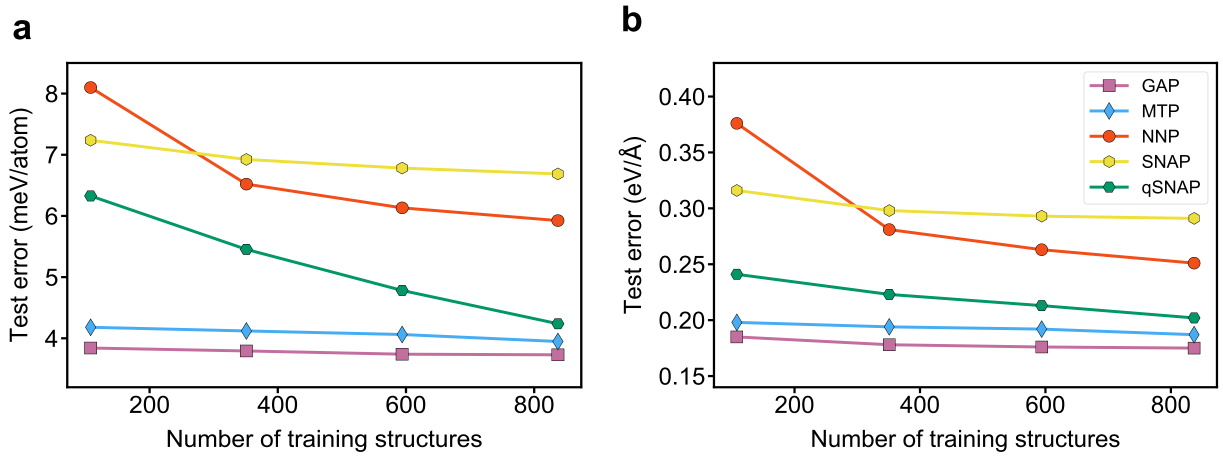

Figure 2.4: RMSEs in predicted (a) energies (b) forces of the test set versus the size of the training data for the ML-IAP Mo models.

tend to perform poorly) with large force distributions. Here, the length of the AIMD simulations was increased four-fold, and more training structures were sampled at the same time interval. The convergence results are shown in Figure 2.4. While the prediction errors of all models decrease with increase in the number of training structures, the most substantial improvements in accuracy, especially in predicted energies, are observed for the NNP and qSNAP models. The SNAP Mo model appears to have converged in energy and force at a training data size of ~ 400 structures, respectively. For the qSNAP, additional training structures offer modest improvements in force accuracy, but large improvements in energy accuracy, which implies qSNAP has a higher "learning rate" in terms of energy accuracy and a lower "learning rate" in terms of force accuracy than NNP. This can also be seen in Figure A.3, which showed the log-log plot of accuracies versus the size of training data and the slope of the line as the "learning capability" of different ML-IAPs. Indeed, it is possible that the NNP and qSNAP Mo models have not been converged with respect to accuracy in energies even at ~ 800 training structures. We have not attempted to further converge these models in view of the computational expense involved.

2.3.3 Accuracy in material properties

The accuracy in predicting basic material properties is critical for evaluating the performance of ML-IAPs. Here, we perform the climbing-image nudged elastic band (CI-NEB) method[128] as well as molecular dynamics (MD) with ML-IAPs to obtain the cubic lattice parameter, elastic constants, migration energies and vacancy formation energies. The comparison of these predicted material properties with respect to the DFT values is provided in Table 2.2. The performances of all ML-IAPs are generally excellent, with lattice parameters within 0.1-2.0% of the DFT values and elastic constants that are typically within 10% of DFT values. It should be noted that the large percentage error in Li for elastic constants is due to the small reference values. The MTP, SNAP and qSNAP models perform well on elastic constants on fcc and bcc systems, but exhibit slightly higher prediction errors in the diamond systems. A possible explanation for the slightly poorer prediction of elastic constants of the NNP model could be the limitation of the size of training data, which restricts the potential of a fully connected neural network. However, it should be noted that despite the slightly higher prediction errors of elastic components for the NNP model, its prediction errors of Voigt-Reuss-Hill approximated bulk modulus[129] across various elemental systems are in good agreement with DFT reference values.

In terms of diffusion properties, the GAP and MTP models perform well across different chemistries, with most of the prediction errors within 10% of DFT values, albeit with a moderate underestimate of the migration energy for diamond systems, in line with the previous study[34]. While SNAP and qSNAP models show high accuracy in predicting diffusion properties for fcc systems, they considerably underestimate the vacancy formation energy as well as activation barrier for diamond systems. It is noteworthy that all ML-IAPs overestimate the migration energy of Mo system by more than 20%, which has also been observed in a previous work[40].

Table 2.2: Calculated cubic lattice parameter a, elastic constants (c_{ij}), Voigt-Reuss-Hill bulk modulus B_{VRH}, migration energy (E_m), vacancy formation energy (E_v) as well as activation barrier for vacancy diffusion ($E_a = E_v + E_m$) with DFT and the four ML-IAPs. Lowest absolute errors with respect to DFT for each property are bolded for ease of reference. Error percentages with respect to DFT values are shown in parentheses.

	DFT	**GAP**	**MTP**	**NNP**	**SNAP**	**qSNAP**
Ni						
a (Å)	3.508	3.523 (0.4%)	3.522 (0.4%)	3.523 (0.4%)	3.522 (0.4%)	**3.521 (0.4%)**
c_{11} (GPa)	276	281 (1.8%)	284 (2.9%)	**274 (-0.8%)**	283 (2.5%)	267 (−3.3%)
c_{12} (GPa)	159	**159 (0.0%)**	172 (8.2%)	169 (6.3%)	168 (5.7%)	155 (−2.5%)
c_{44} (GPa)	132	126 (−4.5%)	127 (-3.8%)	113 (−14.4%)	**129 (-2.3%)**	125 (−5.3%)
B_{VRH} (GPa)	198	**200 (1.0%)**	209 (5.6%)	204 (3.0%)	206 (4.0%)	193 (−2.5%)
E_v (eV)	1.49	1.46 (−2.0%)	1.43 (−4.0%)	1.65 (10.7%)	**1.47 (-1.3%)**	**1.47 (-1.3%)**
E_m (eV)	1.12	1.14 (1.8%)	1.11 (−0.9%)	1.14 (1.8%)	**1.12 (0.0%)**	1.05 (−6.3%)
E_a (eV)	2.61	**2.60 (-0.4%)**	2.54 (−2.7%)	2.79 (6.9%)	2.59 (−0.8%)	2.52 (−3.4%)
Cu						
a (Å)	3.621	**3.634 (0.4%)**	3.636 (0.4%)	3.637 (0.4%)	3.634 (0.4%)	**3.636 (0.4%)**
c_{11} (GPa)	173	**175 (1.2%)**	177 (2.3%)	182 (5.2%)	178 (2.9%)	178 (2.9%)
c_{12} (GPa)	133	120 (−9.8%)	120 (9.8%)	125 (−6.0%)	**126** (−5.3%)	124 (−6.8%)
c_{44} (GPa)	88	82 (−6.8%)	81 (−8.0%)	76 (−13.6%)	**86 (-2.3%)**	82 (−6.8%)
B_{VRH} (GPa)	146	138 (−5.5%)	139 (−4.8%)	**144 (-1.4%)**	143 (−2.1%)	142 (−2.7%)
E_v (eV)	1.15	1.05 (−8.7%)	1.10 (−4.3%)	1.23 (7.0%)	1.19 (3.5%)	**1.15 (0.0%)**
E_m (eV)	0.79	0.76 (−3.8%)	**0.77 (-2.5%)**	**0.77 (-2.5%)**	0.82 (3.8%)	0.74 (−6.3%)
E_a (eV)	1.94	1.81 (−6.7%)	1.87 (−3.6%)	2.00 (3.1%)	2.01 (3.6%)	**1.89 (-2.6%)**
Li						
a (Å)	3.427	3.450 (0.7%)	3.446 (0.6%)	**3.434 (0.2%)**	3.506 (2.3%)	3.469 (1.2%)
c_{11} (GPa)	15	18 (20.0%)	**14 (-6.7%)**	17 (13.3%)	18 (20.0%)	12 (−20.0%)
c_{12} (GPa)	13	14 (7.7%)	**13 (0.0%)**	12 (−7.7%)	7 (−46.2%)	6 (−53.8%)
c_{44} (GPa)	11	12 (9.1%)	**11 (0.0%)**	12 (9.1%)	10 (−9.1%)	**11 (0.0%)**
B_{VRH} (GPa)	14	**15 (7.1%)**	**13 (-7.1%)**	**13 (-7.1%)**	11 (−21.4%)	8 (−42.9%)

Continued on next page

Table 2.2 – continued from previous page

	DFT	GAP	MTP	NNP	SNAP	qSNAP
E_v (eV)	0.62	0.56 (−9.7%)	0.53 (−14.5%)	0.50 (−19.4%)	**0.63 (1.6%)**	0.58 (−6.5%)
E_m (eV)	0.06	**0.06 (0.0%)**	0.08 (33.3%)	0.05 (−16.7%)	0.09 (50.0%)	0.09 (50.0%)
E_a (eV)	0.68	0.62 (−8.8%)	0.61 (−10.3%)	0.55 (−19.1%)	0.72 (5.9%)	**0.67 (-1.5%)**
Mo						
a (Å)	3.168	**3.168 (0.0%)**	3.169 (0.0%)	3.165 (−0.1%)	3.169 (0.0%)	3.170 (0.1%)
c_{11} (GPa)	472	481 (1.9%)	**472 (0.0%)**	441 (−6.6%)	457 (−3.2%)	436 (−7.6%)
c_{12} (GPa)	158	169 (7.0%)	154 (−2.5%)	192 (21.5%)	**158 (0.0%)**	166 (5.1%)
c_{44} (GPa)	106	112 (5.7%)	103 (−2.8%)	114 (7.5%)	109 (2.8%)	**104 (-1.9%)**
B_{VRH} (GPa)	263	271 (3.8%)	**260 (-1.1%)**	**266 (1.1%)**	258 (−1.9%)	256 (−2.7%)
E_v (eV)	2.70	**2.68 (-0.7%)**	2.61 (−3.3%)	2.94 (8.9%)	**2.72 (0.7%)**	2.79 (3.3%)
E_m (eV)	1.22	1.60 (31.1%)	1.51 (23.8%)	1.59 (30.3%)	**1.49 (22.1%)**	1.50 (23.0%)
E_a (eV)	3.92	4.28 (9.2%)	**4.12 (5.1%)**	4.53 (15.6%)	4.21 (7.4%)	4.29 (9.4%)
Si						
a (Å)	5.469	5.458 (−0.2%)	**5.465 (-0.1%)**	5.501 (0.6%)	5.466 (0.1%)	5.464 (-0.1%)
c_{11} (GPa)	156	168 (7.7%)	**155 (-0.6%)**	141 (−9.6%)	128 (−17.9%)	**155 (-0.6%)**
c_{12} (GPa)	65	**62 (-4.6%)**	76 (16.9%)	**62 (-4.6%)**	75 (15.4%)	58 (−10.8%)
c_{44} (GPa)	76	69 (−9.2%)	**75 (-1.3%)**	55 (−27.6%)	71 (−6.6%)	69 (−9.2%)
B_{VRH} (GPa)	95	**97 (2.1%)**	102 (7.4%)	89 (−6.3%)	**93 (-2.1%)**	90 (−5.3%)
E_v (eV)	3.25	3.04 (−6.5%)	**3.11 (-4.3%)**	2.60 (−20.0%)	2.71 (−16.6%)	2.37 (−27.1%)
E_m (eV)	0.21	**0.21 (0.0%)**	0.16 (−23.8%)	**0.21 (0.0%)**	0.26 (23.8%)	0.20 (−4.7%)
E_a (eV)	3.46	3.25 (−6.1%)	**3.27 (-5.5%)**	2.81 (−18.8%)	2.97 (−14.2%)	2.57 (−25.7%)
Ge						
a (Å)	5.763	5.777 (0.2%)	**5.770 (0.1%)**	5.789 (0.5%)	5.773 (0.2%)	5.775 (0.2%)
c_{11} (GPa)	116	127 (9.5%)	106 (−8.6%)	98 (−15.5%)	101 (−12.9%)	**121 (4.3%)**
c_{12} (GPa)	48	**45 (-6.3%)**	54 (12.5%)	54 (12.5%)	41 (−14.6%)	43 (−10.4%)
c_{44} (GPa)	58	54 (−6.9%)	**55 (-5.2%)**	43 (−25.9%)	54 (−6.9%)	50 (−13.8%)
B_{VRH} (GPa)	71	72 (1.4%)	**71 (0.0%)**	69(−2.8%)	61 (−14.1%)	69 (−2.8%)

Continued on next page

Table 2.2 – continued from previous page

	DFT	GAP	MTP	NNP	SNAP	qSNAP
E_v (eV)	2.19	**2.10 (-4.1%)**	1.98 (−9.6%)	1.97 (−10.0%)	1.77 (−19.2%)	1.67 (−23.7%)
E_m (eV)	0.19	0.17 (−10.5%)	0.17 (−10.5%)	**0.20 (5.3%)**	0.28 (47.4%)	**0.18 (-5.3%)**
E_a (eV)	2.38	**2.27 (-4.6%)**	2.15 (−9.7%)	2.18 (−8.8%)	2.05 (−13.9)	1.85 (−22.3%)

We have also calculated the relaxed (011) γ surface for the generalized stacking faults (GSFs) along the $[\bar{1}\bar{1}1]$ direction[124,130] for Mo, (111) glide plane along the [112] direction[34,131] for Si, and (111) γ surface along the [112] direction[132,133] for Ni and Cu, as these have been already been studied extensively in previous works.[34,124,130–133]. From Figure 2.5 and Table 2.3, it can be observed that all ML-IAPs are able to reproduce the major qualitative features of the relaxed (011) γ surface and the correct trend in the unstable stacking fault energy for all four systems. The MTP models generally yield γ_{us} that are closest to DFT for Si (111)[112], Ni(111)[112] and Cu(111)[112]. All ML-IAPs significantly underestimate the Mo(011)$[\bar{1}\bar{1}1]$ γ surface, which is consistent with previous ML-IAP studies of bcc metals[30]. The NNP models exhibit the largest deviation from DFT for Mo(011)[112], Ni(111)[112] and Cu(111)[112] γ surfaces. In particular, the NNP models predict a symmetric γ surface with a near-zero intrinsic stacking fault energy for the fcc metals Ni and Cu.

2.3.4 Accuracy in equations of state

To provide an evaluation of the performance of ML-IAPs far from equilibrium, we have computed a pairwise comparison of the equation of state (EOS) curves for all elements studied using the Δ_{EOS} gauge of Lejaeghere et al.[134–136] The Δ_{EOS} gauge, which has been used to evaluate

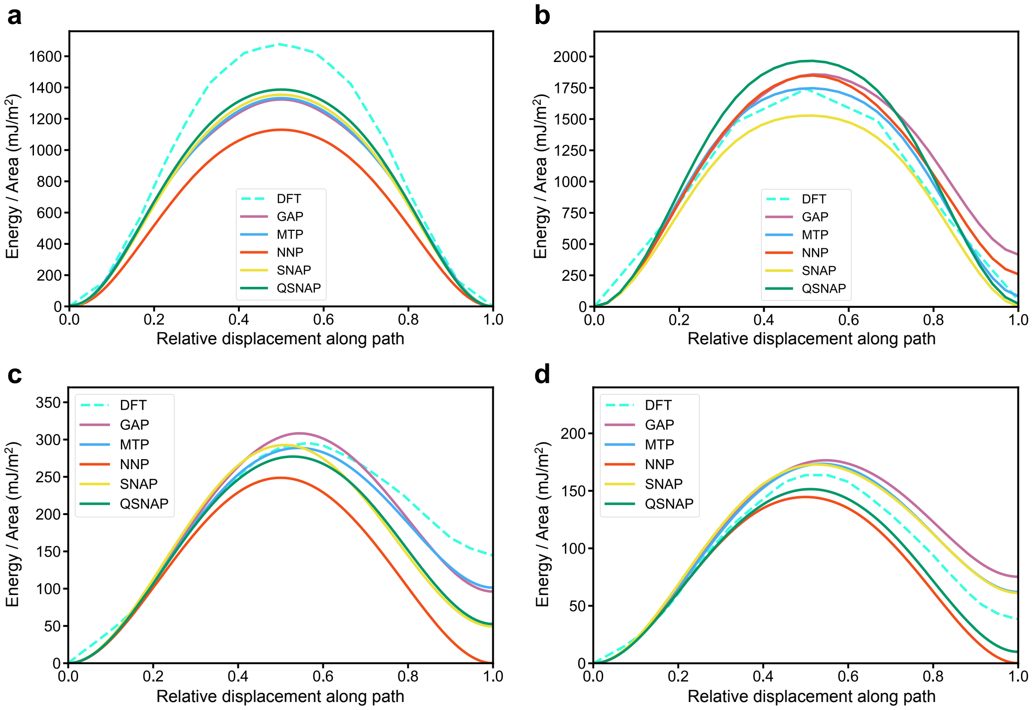

Figure 2.5: Cross sections of the relaxed γ surfaces calculated with all four ML-IAPs with respect to DFT reference data.[34,124,133]. (a) The relaxed (011) γ surface along the $[\bar{1}\bar{1}1]$ direction for Mo. (b) The relaxed (111) glide plane along the [112] direction for Si. (c) The relaxed (111) γ surface along the [112] direction for Ni. (d) The relaxed (111) γ surface along the [112] direction for Cu.

Table 2.3: Calculated unstable stacking fault energy γ_{us} of (011) γ surface along the $[\bar{1}\bar{1}1]$ direction for Mo, (111) glide plane along the [112] direction for Si and (111) γ surface along the [112] direction for Ni and Cu. Lowest absolute errors with respect to DFT are bolded for ease of reference. Error percentages with respect to DFT values are shown in parentheses.

$\gamma_{\text{us}}(\text{mJ/m}^2)$	Mo (011) $[\bar{1}\bar{1}1]$	Si (111) [112]	Ni (111) [112]	Cu (111) [112]
DFT	1677[124]	1740[34]	289[133]	164[133]
GAP	1324 (−21.0%)	1858 (6.8%)	308 (6.6%)	177 (7.9%)
MTP	1333 (−20.5%)	**1747 (0.4%)**	**288 (-0.3%)**	173 (5.5%)
NNP	1130 (−32.6%)	1849 (6.3%)	248 (−14.2%)	145 (−11.6%)
SNAP	1354 (−19.3%)	1528 (−12.2%)	292 (1.0%)	**172 (4.9%)**
qSNAP	**1387 (-17.3%)**	1965 (12.9%)	277 (−4.2%)	151 (−7.9%)

accuracy differences between DFT codes, is the root-mean-square difference between two EOS curves over a $\pm 6\%$ interval around the equilibrium volume, defined as follows:

$$\Delta_{\mathrm{EOS}} = \sqrt{\frac{\int_{0.94V_0}^{1.06V_0} [E^{\mathrm{a}}(V) - E^{\mathrm{b}}(V)]^2 dV}{0.12V_0}} \tag{2.8}$$

where E^{a} and E^{b} denote energies computed using methods a and b, respectively.

Figure **??** shows the Δ_{EOS} values of various machine learning models with respect to DFT reference data for different elemental systems as well as the EOS curves of these ML-IAPs. In all cases, the Δ_{EOS} for all ML-IAPs for all elements are within 2 meV/atom, which is the threshold for "indistinguishable EOS" previously used in evaluating different DFT codes[137]. It is noteworthy that despite the relatively high prediction errors of SNAP models presented in Figure 2.3a, they perform considerably better in predicting the EOS curves, with all the Δ_{EOS} lower than 1 meV/atom across different chemistries. The NNP models deviate slightly from DFT curves at both tensile and compressive strains for fcc systems, while for diamond systems, the deviation of the NNP models from DFT curve is comparable with those of GAP and MTP models, as evidenced in Δ gauge comparison. In general, it is more challenging to give highly accurate predictions of EOS in diamond system than in fcc and bcc systems.

2.3.5 Accuracy in molecular dynamics (MD) trajectories

One of the principal applications of ML-IAPs is in molecular dynamics (MD) simulations. To assess the ability of the ML-IAPs to provide stable MD trajectories, we carried out NVT MD simulations at 1,300 K ($0.5\times$ melting point) on a $3 \times 3 \times 3$ 54-atoms supercell of bulk Mo for 0.25 ns using LAMMPS with the different ML-IAPs. A total of 40 snapshots at an interval of 2.5 ps were sampled from each MD trajectory, and DFT static calculations were performed on these snapshots. Figure 2.7 shows the distribution of the errors in the energies and forces of sampled structures. In line with the previous results, the GAP and MTP models generally exhibit smaller

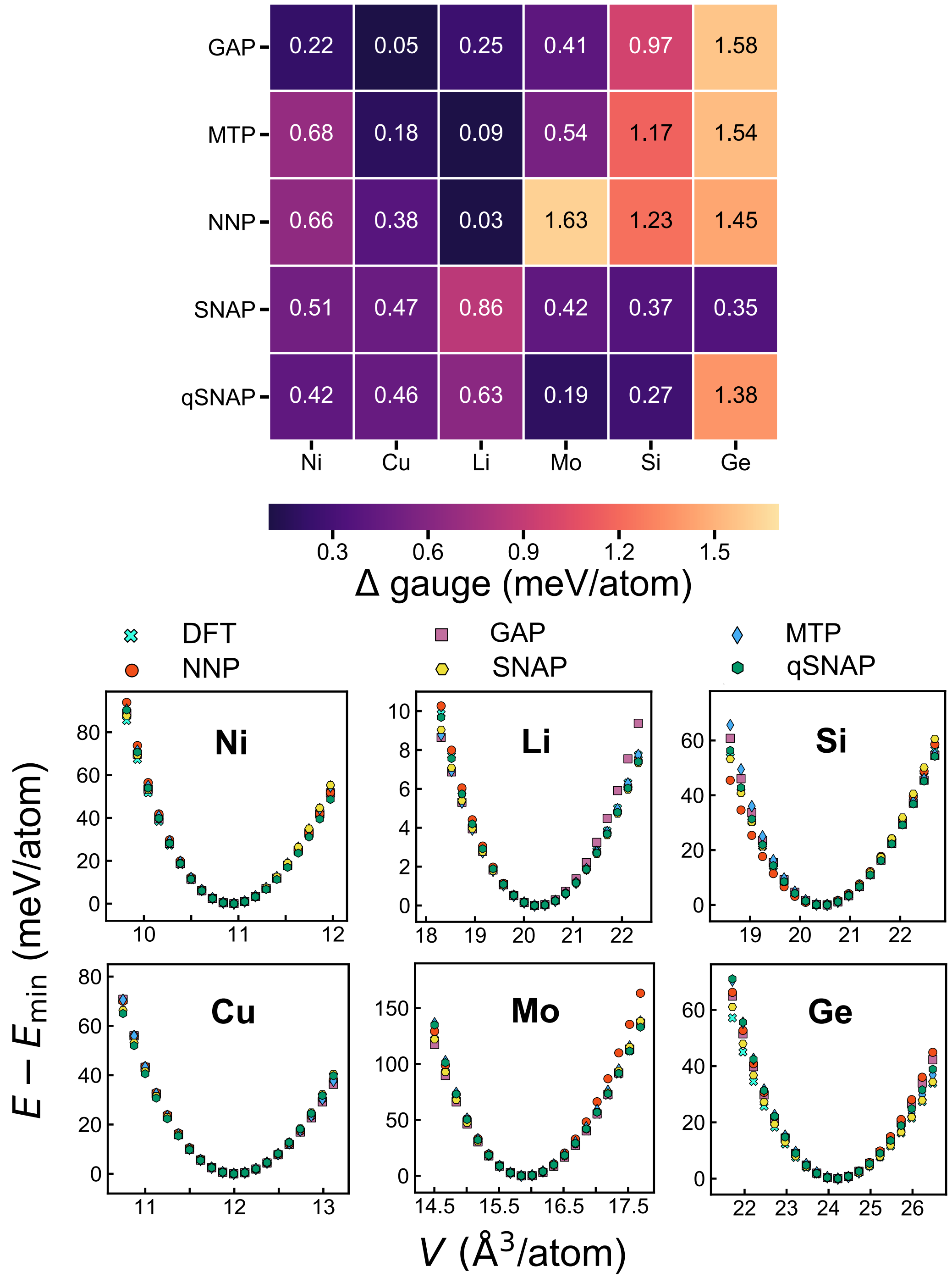

	Ni	Cu	Li	Mo	Si	Ge
GAP	0.22	0.05	0.25	0.41	0.97	1.58
MTP	0.68	0.18	0.09	0.54	1.17	1.54
NNP	0.66	0.38	0.03	1.63	1.23	1.45
SNAP	0.51	0.47	0.86	0.42	0.37	0.35
qSNAP	0.42	0.46	0.63	0.19	0.27	1.38

Figure 2.6: Assessment of accuracy of ML-IAPs in predicting equation of state. (a) Δ gauge comparison provides quantitative estimate of deviation between the EOS curve from each ML-IAP with that of DFT. (b) EOS curves for all six elements using DFT and the four ML-IAPs.

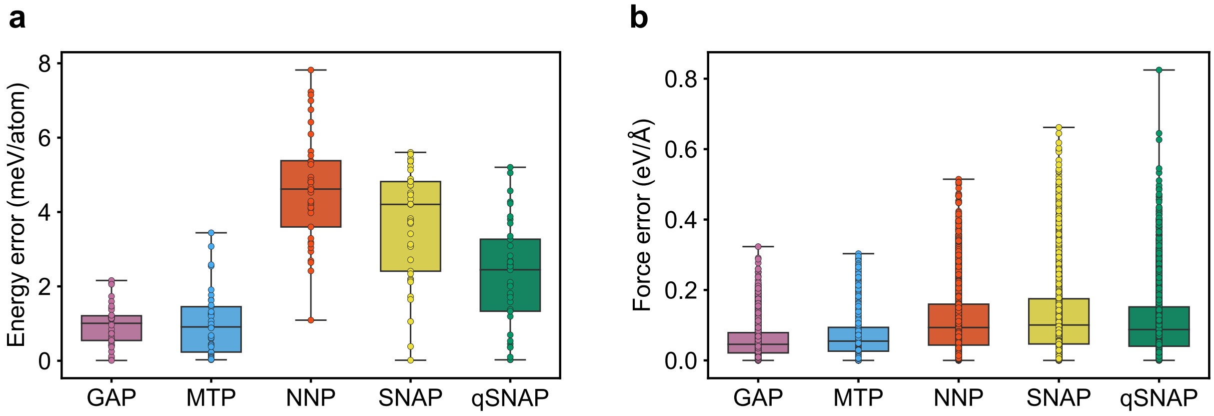

Figure 2.7: Error distributions in (a) predicted energies (b) predicted forces for sampled structures from MD simulations using each ML-IAP. The rectangular box indicates the interquartile range (IQR), while the line within the box indicates the median.

errors in the energies and forces than the NNP, SNAP and qSNAP models. The GAP model has not only the lowest median but also the smallest interquartile range (IQR) in the errors in energies and forces. Somewhat interestingly, the NNP model has higher energy errors, but smaller force errors than SNAP and qSNAP. For consistency of comparison, all models shown here are the "optimal" models based on ~ 100 training structures. It is likely that a larger training set would improve the performance of the NNP and qSNAP models. (Figure 2.4).

2.3.6 Accuracy in polymorphic energy differences

To evaluate the ability of the ML-IAPs to extrapolate to unseen data, we have computed the energy differences between the DFT ground state polymorph and a low-energy polymorph for each element, presented in Figure 2.8. The low-energy polymorphs correspond to the bcc, fcc, and wurtzite (hexagonal diamond) structures for the fcc, bcc, and diamond systems, respectively. It should be noted that only the ground state structures were used in training the ML-IAPs, and these low-energy polymorphs were not present in the training structures. Except for Li which has an extremely small energy difference between the fcc and bcc structures in DFT, all ML-IAPs are able to reproduce qualitatively the energy difference between polymorphs. For most systems, the ML-IAPs are able to reproduce energy differences between the polymorphs to within 10-20 meV/atom; the main exception is Mo, which exhibits a large energy difference between the fcc and bcc structures. One notable observation is that the GAP model shows the largest error in predicting the energy difference between the wurtzite and diamond structures in Si and Ge compared to the other ML-IAPs, despite having relatively low RMSE in predicted energies in these systems (see Figure 2.3a). We believe that this may be due to the fact that the active features in GAP diamond models did not cover the polymorph phase region and the Gaussian process is sensitive to unseen data, while the other IAPs are able to extrapolate the interactions to this unseen configuration more effectively. To test this hypothesis, we have constructed two additional Si GAP models derived by augmenting the original Si GAP model with (a) features close to the wurtzite polymorph, and (b) features that are exactly correspond to the wurtzite polymorph. As seen from Figure A.4, the predicted energy differences between the wurtzite and diamond polymorphs are much closer to the DFT values for the augmented Si GAP models. A principal component analysis further shows that the wurtzite polymorph lies in a feature space that is not covered by the original training data. Somewhat surprisingly, the linear SNAP model exhibits among the best performance in reproducing the polymorphic energy differences across all systems, outperforming even the GAP and MTP for Mo, Si and Ge, despite having substantially larger RMSEs in energies and forces.

2.4 Conclusions

We have performed a comprehensive unbiased evaluation of the GAP, MTP, NNP, SNAP, and qSNAP ML-IAP models using consistently-generated DFT data on six elemental systems spanning different crystal structures (fcc, bcc, and diamond), chemistries (main group metals, transition metals and semiconductors) and bonding (metallic and covalent). This evaluation is carried out across three key metrics that are of critical importance for any potential user of these

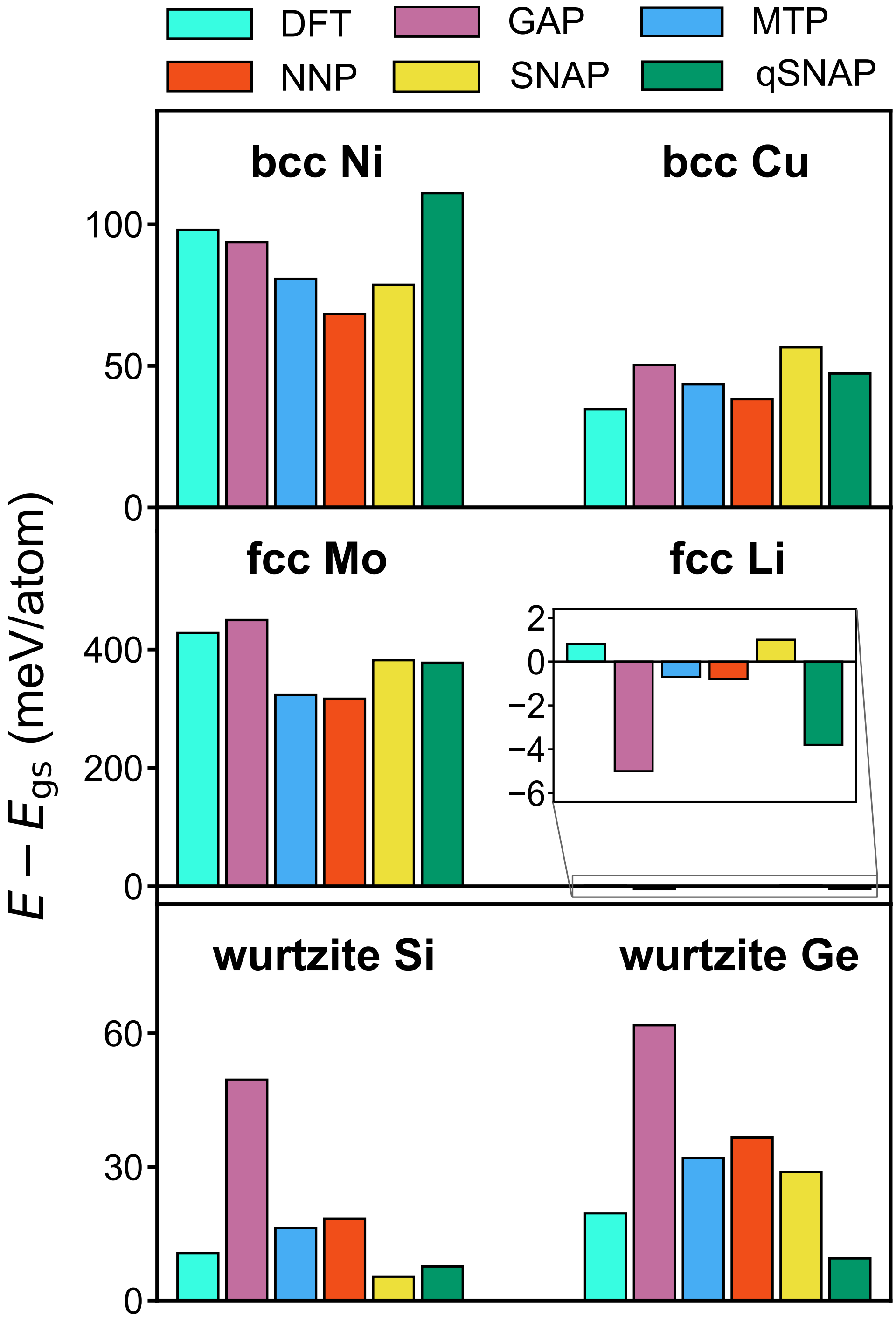

Figure 2.8: Calculated energetic differences between the typical low energy polymorph and ground-state polymorph of each elemental system. The inset shows the magnified bar chart for Li system due to its relatively small range. The typical low energy polymorph is indicated with the label above each bar chart.

ML-IAPs:

1. Accuracy in predicted energies, forces and properties for both seen and unseen structures;
2. Training data requirements, which influence the number of expensive DFT computations that have to be performed to train an ML-IAP to a given accuracy; and
3. Computational cost, which influences the size of the systems on which computations can be performed for a given computing budget.

These three metrics are inextricably linked - for all the four ML-IAPs, an increase in number of DOF (with increase in computational cost) and increase in training structures generally leads to higher accuracy, though diminishing returns are observed beyond a certain number of DOFs. We demonstrate the application of the Pareto frontier as a means to identify the optimal trade-offs between these metrics. For all ML-IAPs, we find that there is an "optimal" configuration at which further expansion of the number of DOF yields little improvement in accuracy with increases in computational cost. We find that all ML-IAPs are able to achieve near-DFT accuracy in predicting energies, forces and material properties, substantially outperforming traditional IAPs. The GAP and MTP models exhibit the smallest RMSEs in energies and forces. However, the GAP models are among the most computationally expensive for a given accuracy (based on current implementations) and show poor extrapolability to higher energy polymorphs in the diamond systems. Indeed, the simple linear SNAP model, which has among the highest RMSEs in predicted energies and forces, show the best extrapolability to higher energy polymorphs as well as reproducing the equations of state for the diamond systems. The NNP and qSNAP models show relatively high RMSEs in energies with small data sizes, but these can be mitigated with increases in training data.

Another somewhat surprising conclusion is also that even with relatively small training data sets of $\sim$100-200 structures, the GAP, MTP and SNAP models appear to be reasonably well-converged to meV atom^{-1} accuracy in energies and 0.01 eV Å^{-1} accuracy in forces. The

NNP and qSNAP models can be further improved with larger training data sets, but the RMSEs even at $\sim$ 100 structures are not excessively high. As training cost is a key performance metric, we have not attempted to further converge the NNP and qSNAP models beyond $\sim$ 800 structures (Figure 2.4), which is already several times the benchmarked training data set size. We attribute this performance to the training data generation procedure, which is aimed at sampling a diversity of structures from both ground state and multi-temperature AIMD simulations. In other words, the diversity of training data is arguably a more important consideration than quantity.

Finally, we will note several limitations of this study, which are possible avenues for future work. Firstly, no attempt was made include non-elemental (binary, ternaries, etc.) systems in this study for practical considerations of computational cost in generating the large number of training structures needed and the diverse range of bonding types (e.g., metallic, ionic, covalent, and van der Waals, or a mixture of these). Second, we have chosen to focus on only ML-IAPs based on local environment descriptors. It should be noted that there are similarities between some of the descriptors. Both the SOAP and bispectrum (SNAP) descriptors are derived from the local atomic density function, while the NNP and MTP are based on parameterizations of the radial and angular distributions using various basis functions. There are alternative ML-IAPs that rely on global representations[138] that were not covered in this work. Finally, we have not attempted to combine the different local environment descriptors (symmetry functions, SOAP, bispectrum, moment tensors) with different ML frameworks (linear regression, Gaussian process regression, neural network, etc.). Instead, we rely on existing implementations of ML-IAPs as reported. The choice of descriptor affects how efficiently diverse local environments can be encoded, while the choice of ML framework determines the functional flexibility in mapping the relationship between descriptors and energies/forces. Ultimately, the performance of an ML-IAP is related to the atomic environment descriptor and the ML methodology. Our work has identified some differences in performances as being related to the choice of the ML model. For example, the quadratic qSNAP model can be converged to substantially higher accuracies than the linear

SNAP model, albeit at increased risk of overfitting. The poorer extrapolability in the diamond systems and higher computational cost of the GAP can be traced to the use of Gaussian process regression. Constructing ML-IAPs using descriptor-model combinations can potentially yield further insights into the interplay between atomic descriptor and ML framework as well as better trade-offs between accuracy and cost for a particular application.

Chapter 2 presents an impartial comparison between four major ML-IAPs from several aspects: accuracy, data requirement, and computational cost. We also analyzed the factors that may determine their relative strengths and weaknesses and extended the concept of Pareto frontier in terms of accuracy and cost for ML-IAPs assessment.

Chapter 3

Atomistic simulations of dislocation mobility in refractory high-entropy alloys and the effect of chemical short-range order

3.1 Introduction

Metallic alloys containing multiple principal alloying elements, which are known as high-entropy alloys (HEAs)[13,139,140], have attracted extensive research interest in recent years with many studies focused on their microstructure, mechanical properties and underlying deformation mechanisms[141–143]. For example, as a new class of structural materials, certain face-centered cubic (fcc) alloys, in particular CrCoNi-based HEAs, have been shown to possess improved strength and exceptional damage tolerance, especially at cryogenic temperatures[144,145]. A second prominent class of HEA systems are refractory high-entropy alloys (RHEAs), which comprise mostly refractory elements and invariably crystallize as body-centered cubic (bcc) solid-solutions; these alloys have been considered as promising candidate materials for elevated-temperature applications due to their exceptional resistance to softening and extremely high melting points[146–148]. Although many practical challenges remain in processing of RHEAs due to their brittleness and oxidation susceptibility[149], numerous RHEAs have been designed, fabricated and assessed experimentally, with additional insight coming from computational approaches[150–154]. Specifically, to investigate the deformation of RHEAs, transmission electron microscopy (TEM) studies on RHEAs have shown a dominant role of screw dislocations with increasing plastic strain[155,156], and slip activity on high-order-planes has been observed through in situ scanning electron microscopy experiments[153]; indeed, strong intrinsic lattice resistance has been generally found in these alloys[156,157]. Theoretical models for strengthening in RHEAs by screw dislocations have been developed[6,158], and atomistic simulations of dislocation properties using molecular dynamics (MD) and density functional theory (DFT) calculations have been undertaken[7,159–162]. However, compared to single-phase *bcc* metals, there are still limited studies on the unique deformation behavior of *bcc* RHEAs. Although HEAs possess crystalline order, but compositional disorder, they are not necessarily random solid solutions for every atomic species[163–172]. A further feature of HEAs is the presence of local chemical short-range order (SRO), which can affect defect properties and hence may influence mechanical properties. In previous studies, SRO effects in fcc or hcp alloys have been found to be able to change the dislocation morphology, i.e., from wavy to planar, and may impact twinning[173,174]. Recent experimental results have provided direct evidence for the presence of SRO in certain fcc HEAs and its correlation with mechanical properties[175,176]. Moreover, for RHEAs, such as the MoNbTaW, numerical studies have revealed a significant energetic driving force for SRO[162–164,177]. The effect of such SRO is thus a relevant issue that requires further investigation for *bcc*-RHEAs. To date, there are to our knowledge no detailed investigations of the effects of SRO on larger-scale defect properties, especially dislocation mobility, for *bcc*-RHEAs. This situation provides the motivation for the current study. Accordingly, our objective here is to employ MD simulations, based on a machine-learning interatomic potential developed for this purpose, to investigate in detail the mechanisms of the movement of dislocations as a function of temperature in *bcc* RHEAs, focusing on the MoNbTaW system, with specific emphasis on the effect of SRO on dislocation mobility.

3.2 Methods

3.2.1 Machine-learning interatomic potential

The MTP model and its formalism have been extensively studied and applied in previous work4[29,43,44,100]. The MTP essentially constructs contracted rotationally invariant local environment descriptors for each atom in the system and builds a polynomial regressed correlation between the potential energy surface (PES) and these descriptors. The descriptors, named moment tensors, are devised as follows:

$$M_{\mu,\nu}(\mathbf{R}) = \sum_j f_\mu(R_{ij})\ \underbrace{\mathbf{R}_{ij} \otimes \cdots \otimes \mathbf{R}_{ij}}_{\nu\ times}, \tag{3.1}$$

where the functions f_μ are the radial distribution of local environment around atom i and these functions are specified according to the atomic type of the neighbor atom j. The terms $R_{ij} \otimes \cdots \otimes R_{ij}$ are tensors of rank ν encoding the angular information about the local environment. The basis functions $B(R)$ are formulated by contracting the moment tensors $M_{\mu,\nu}$ to a scalar, and the potential energy of atom i are linearly expanded on a set of the basis functions:

$$E_i(\mathbf{R}) = \sum_l \beta_l B(\mathbf{R}) \tag{3.2}$$

There are two key hyperparameters that determine the performance of the accuracy and computational cost of the MTP: the radius cutoff (R_{cut}) and maximum level (lev_{max}). The R_{cut} encodes the extent of atomic interactions in the local environment, and the lev_{max} controls the completeness of the basis functions $B(R)$, which in turn influences the computational cost and likelihood of over-fitting. In this work, we adopted the grid search method to examine the choice of hyperparameters by evaluating the performance on reproducing the basic materials properties, e.g., elastic constants and stacking fault energies. The R_{cut} and lev_{max} were set to 4.7 Å and 14, respectively. The energy and force data were assigned weights of 1 and 0.01 respectively, in line with previous studies[25].

3.2.2 Local chemical short-range order parameter

The Warren Cowley order parameter[178], $\alpha_{ij} = 1 - \frac{P_{j,i}}{c_j}$, was used to quantify the SRO in each specific nearest-neighbouring shell. $P_{j,i}$ is the fraction of species j in the nearest-neighbouring shell around i, and c_j is the concentration of j. To indication the overall degree of SRO, we make use of a quantity given as the sum of all the $|\alpha_{ij}|$ for all species at nearest-neighbor shell ($\sum_{i,j} |\alpha_{ij}|$).

3.2.3 Molecular dynamic simulation

MD simulations were performed using the software package LAMMPS[17,179] and the atomic configurations were displayed by OVITO68. The simulation cells are illustrated in B.1, with dimensions of approximately 150 Å in x, 320 Å in y, 200 Å in z and contains 573672 atoms.

3.2.4 MC/MD simulation

The MC/MD simulations were first conducted to equilibration the SRO before the dislocation line was inserted in the cell. The periodic boundary conditions are set for all three directions. The samples were initially relaxed and equilibrated at 800K and zero pressure under the NPT ensemble through MD. After that MC steps consistent of attempted atom swaps were conducted, hybrid with MD. In each MC step, a swap of one random atom with the other random atom of different type is conducted based on the Metropolis algorithm. 10^2 MC swaps were conducted at every 103 MD steps and the time step is 0.001 ps during the simulation.

3.2.5 Dislocation Mobility Simulation

The dislocation line was inserted in the simulation cell based on the Burgers vector[180,181] for both RSS and the SRO sample after MD/MC relaxation. Periodic boundary conditions were imposed along x- and y-directions and shrink-wrapped non-periodic boundary condition in z-direction. The samples were initially relaxed and equilibrated at the targeted temperature and pressure in the x- and y-direction was equilibrated to zero through NPT ensemble for 50 ps. During the loading step, the bottom two layers of atoms in z-direction were fixed and the top two layers of atoms were treated as rigid body with different levels of shear stresses applied, while NVT ensemble was applied to other atoms. To minimize the effect of stress waves and oscillation of the shear stress, the applied shear stress was gradually ramped from zero at a rate of 20MPa per 1.5 ps. When the shear stress reached the target value, it was held constant for 150 ps while the dislocation positions were recorded.

3.3 Results

3.3.1 Machine-learning interatomic potential

In this section we discuss results of the development of the interatomic-potential model used to enable the application of MD simulations of dislocation properties in *bcc* MoNbTaW. We employ the general framework of machine-learning (ML) based approaches, which have emerged recently as a systematic framework to develop potentials with accuracies near that of the underlying DFT calculations for elemental and multi-component systems[7,25,29,30,43]. Here, using training data reported previously[7] for elemental, binary, ternary, and quaternary systems in Nb-Ta-Mo-W, we developed a potential for the MoNbTaW RHEA based on the moment tensor potential (MTP) formalism, which has been found to feature an excellent balance between accuracy and computational cost[25]. The flowchart for constructing the MTP is shown in Fig. 3.1a with the methodological details provided in the Methods section. The basic materials property predictions of the MTP model are provided in B.1. Figures 3.1b-c show a comparison of the DFT- and MTP-predicted energies and forces for both training and test sets. While the mean absolute errors (MAEs) of energies of 4.6 and 4.3 meV $atom^{-1}$ for respective training and test data are similar to those reported for previously developed potentials[7], the MAEs of forces were decreased by half using the present implementation of MTP, compared to the previous spectral neighbor analysis potential (SNAP).[7] In addition, since the current work aims to investigate dislocation properties through MD simulations, we have also undertaken further validation studies of the MTP for dislocation energetics. Specifically, we consider the distribution of excess energies for supercells with a dislocation dipole, as the dislocation cores are moved to different local environments within the cell, as calculated in recent DFT calculations for systems with varying degrees of SRO[162]. The distribution of dislocation dipole energies obtained with the MTP are found to be in excellent agreement with these previous DFT results, as shown in B.2. These results suggest that the MTP provides an accurate model for the variation in dislocation core energies as a function of local environment, motivating its use in the current MD studies of dislocation mobilities.

3.3.2 Local chemical short-range order in MoNbTaW RHEA

To enable investigation of the effect of SRO on dislocation mobility, we develop two simulation cells that can be used for such simulations in MD, one corresponding to a random-solid-solution (RSS), and another corresponding to an equilibrium state of SRO at a temperature of 800K (this temperature is chosen as one where SRO is relatively strong, but above that associated long-range-ordering transitions). To equilibrate the SRO state, we apply a hybrid MD/Monte Carlo (MD/MC) approach. Details of the simulations and the nature of the equilibrium SRO are described in the Methods section.

We note that in the studies of dislocation mobility at different temperatures presented below, we compare results for both RSS and systems with SRO equilibrated at 800K. The purpose of this comparison is to explore the effect of SRO, and the SRO state at 800K is chosen as a representative configuration where SRO is pronounced. Thus, in this scenario we are simulating the effect of SRO derived from annealing the sample at one single temperature (800K), on the subsequent motion of dislocations over a range of deformation temperatures.

3.3.3 Screw dislocation velocities and the influence of SRO

A screw dislocation line is created in both the RSS and SRO simulation supercells. Shear stresses with a range of different values are applied at different temperatures to drive the motion of the screw dislocations and characterize their mobility (see Methods section). It is worth mentioning that due to practical considerations of computation cost, the current work considers

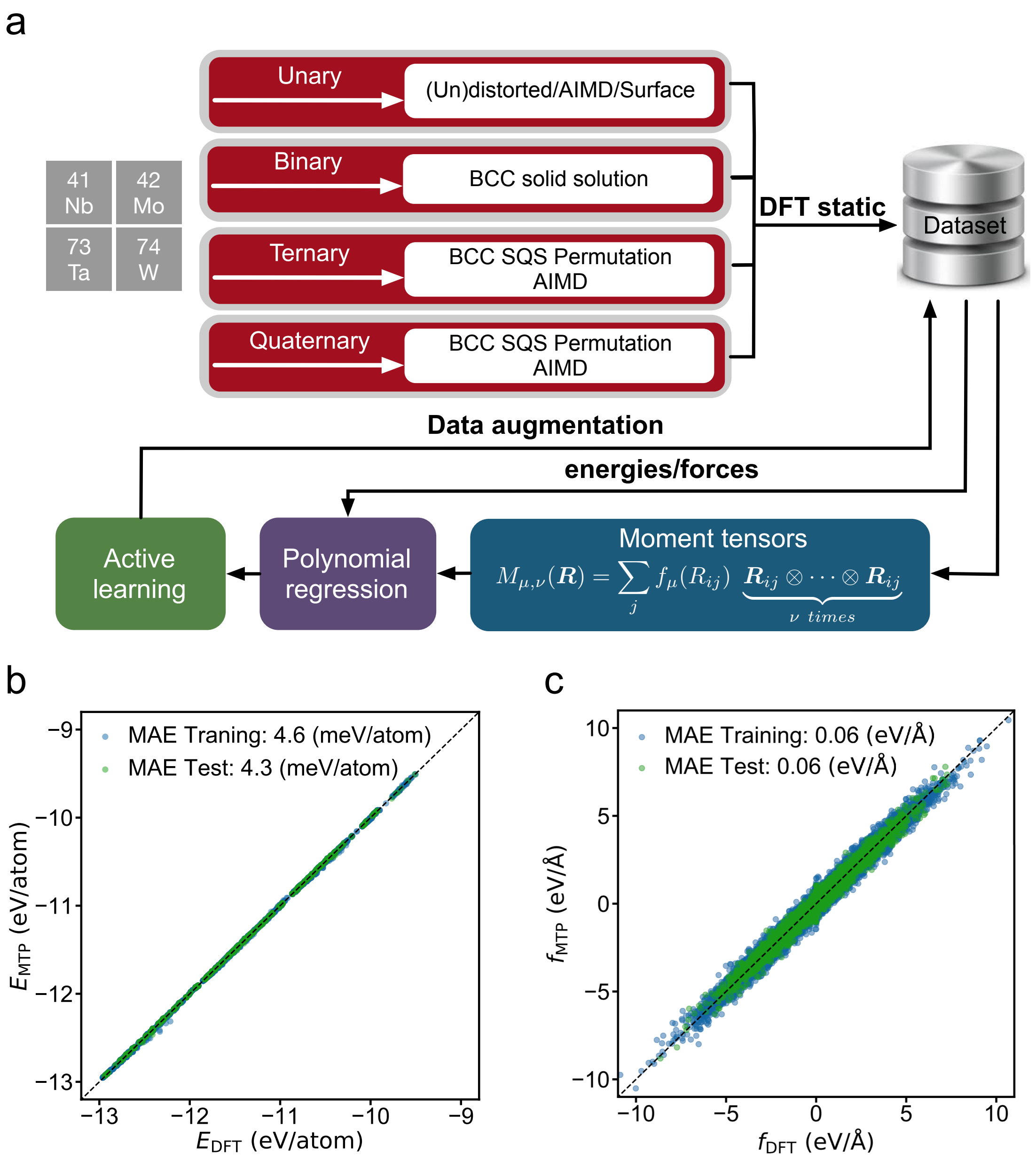

Figure 3.1: Machine learning interatomic potential development and evaluation. a Flowchart of constructing the moment tensor potential (MTP) for the NbMoTaW RHEA. Parity plots of the MTP prediction on b, energies and c, forces for training and test data are shown.

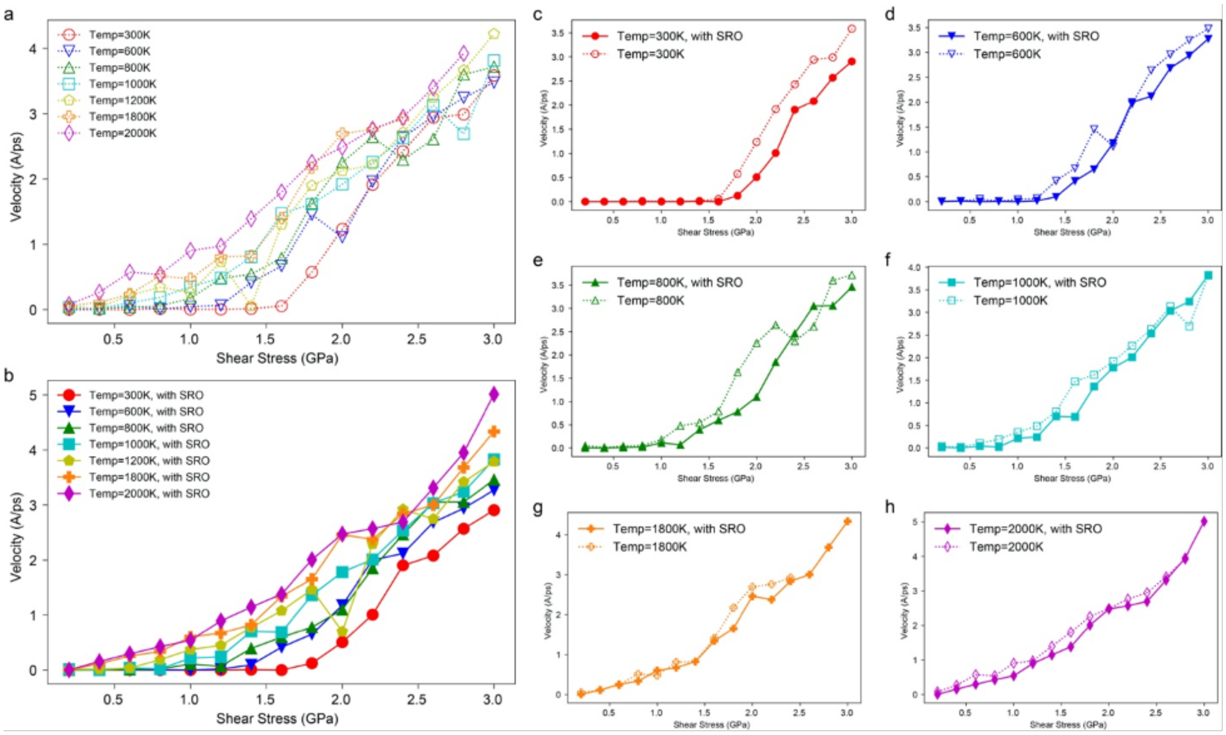

Figure 3.2: Simulation results for the effect of SRO on the velocities of screw dislocations as a function of applied shear stress over a range of temperatures. a, Velocities of screw dislocations in the RSS sample as a function of applied shear strain. b, Velocities of screw dislocations versus shear stress in the sample with local chemical SRO equilibrated at 800K. c-h, Detailed comparisons of the influence of SRO at different temperatures from 300K to 2000K. Lines between scattered data are guides to the eyes and do not correspond to fits of theoretical models.

a periodic length along the dislocation line direction of approximately 15 nm. The simulations thus investigate mobilities for dislocations with line lengths that are quite short compared with those characteristics of realistic experimental conditions, and considered in theoretical models[158]. The mobilities calculated in current setup are expected to be dependent on length in the range of size employed in this work[180]. Thus, the focus in the present work is on understanding intrinsic strengthening mechanisms and the associated effects of SRO; detailed comparisons of mobility magnitudes would require use of this information in theoretical models than can be extrapolated to larger line lengths.

Figure 3.2 shows the velocities of screw dislocations as a function of applied shear stress, in cells with and without SRO at various temperatures. In Fig. 3.2a, the dashed lines represent the velocity vs. stress data for a screw dislocation in the RSS sample under applied stresses ranging from 0 to 3.0 GPa, at temperatures from 300K to 2000K, whereas the solid lines in Fig. 3.2b represent the corresponding results for a screw dislocation in the sample with SRO under the same conditions. The results show that, at low temperatures, the screw dislocation does not move under low values of the applied stress within the simulation timescale. When the stress is increased above some critical level, we can observe the initiation of screw dislocation movement at a velocity that increases with the magnitude of the applied shear stress. As the temperature increases, the critical stress to initiate screw dislocation glide is progressively reduced. When the temperature reaches 1800K or 2000K, even at the lowest applied stress of 200 MPa in our simulation, screw dislocation glide can be clearly observed within the simulation time scale. Overall, the results demonstrate that screw dislocation glide in the MoNbTaW RHEA exhibits strongly temperature-dependent behavior.

Figures 3.2c-h compare the screw-dislocation velocities with and without SRO at different temperatures. At 300K (Fig. 3.2c), the influence of SRO is clearly apparent; based on the shift in the velocity curve, we can estimate the extra strengthening from SRO to be $\sim$180 MPa. We can attribute the extra strengthening from SRO to be associated with the break-up of local chemical order which creates diffuse antiphase boundaries (DAPBs)[182]. When the screw dislocation glides in a system containing SRO, the order will be partially destroyed and a DAPB will be created along the glide plane, with an energy cost per area γ_{DAPB}. A classical estimation of this strengthening effect of SRO by Fisher48 can be written as: $\Delta\tau = \gamma_{\text{DAPB}}/b$, where $\Delta\tau$ is the stress increment due to SRO and b is the Burgers vector. Using the value of the γ_{DAPB} from Figure B.3, the stress increment based on Fisher's relationship is approximately 130 MPa, which is comparable to the strengthening estimated from the MD simulations in Fig. 3.2c-d at temperatures of 300K and 600K. However, in this model the strengthening effect of SRO is athermal and should also be observed at higher temperatures, contrary to the current simulation data. The influence of SRO at higher temperatures is illustrated in Fig. 3.2e-f, for temperatures ranging from T = 800K to 2000K. There is a clear attenuation of the SRO strengthening in these figures as temperature is increased. Indeed, when the temperature reaches 2000K, the dashed and solid lines in Fig. 3.2f, respectively representing the screw dislocation mobility in the RSS and SRO samples, essentially overlap. A theoretical framework for interpreting the effect of temperature on the level of SRO strengthening is presented below.

3.3.4 Screw dislocation glide mechanism and strengthening through cross-slip locking

An analysis of the atomic configurations during screw dislocation glide reveals that the dominant mechanism underlying dislocation motion in the lower-to middle temperature and stress regimes corresponds to thermally-activated kink-pair nucleation and migration[183,184], with a strong temperature-dependence similar to that seen in pure *bcc* metals. Figures 3.3a(i-iv) display a sequence of snapshots from the simulations highlighting kink-pair nucleation and migration along the dislocation line.

From an analysis of the velocity data for various temperatures and stresses from all simulations, it is found that certain simulations show anomalously low average dislocation velocities compared to other data. For example, in Fig. 3.3b the velocities at 1200K in both RSS and SRO samples exhibit two data points with very low velocity values, as highlighted by the dashed circles. Figure 3.3c shows the displacement vs. time results for a screw dislocation in the simulation with 1.4 GPa shear stress in the RSS sample, where it can be seen that the dislocation moves initially at a constant velocity via the kink-pair nucleation and migration mechanism; however, at a certain point, this glide is arrested due to the formation of a locking mechanism such that no further glide is observed.

In *bcc* metals, cross-kinks are formed when multiple kink-pairs nucleate on the same dislocation line but on different slip planes; breaking free from such cross-kink pinning sites requires higher stress or thermal activation. This phenomenon thus provides extra strengthening

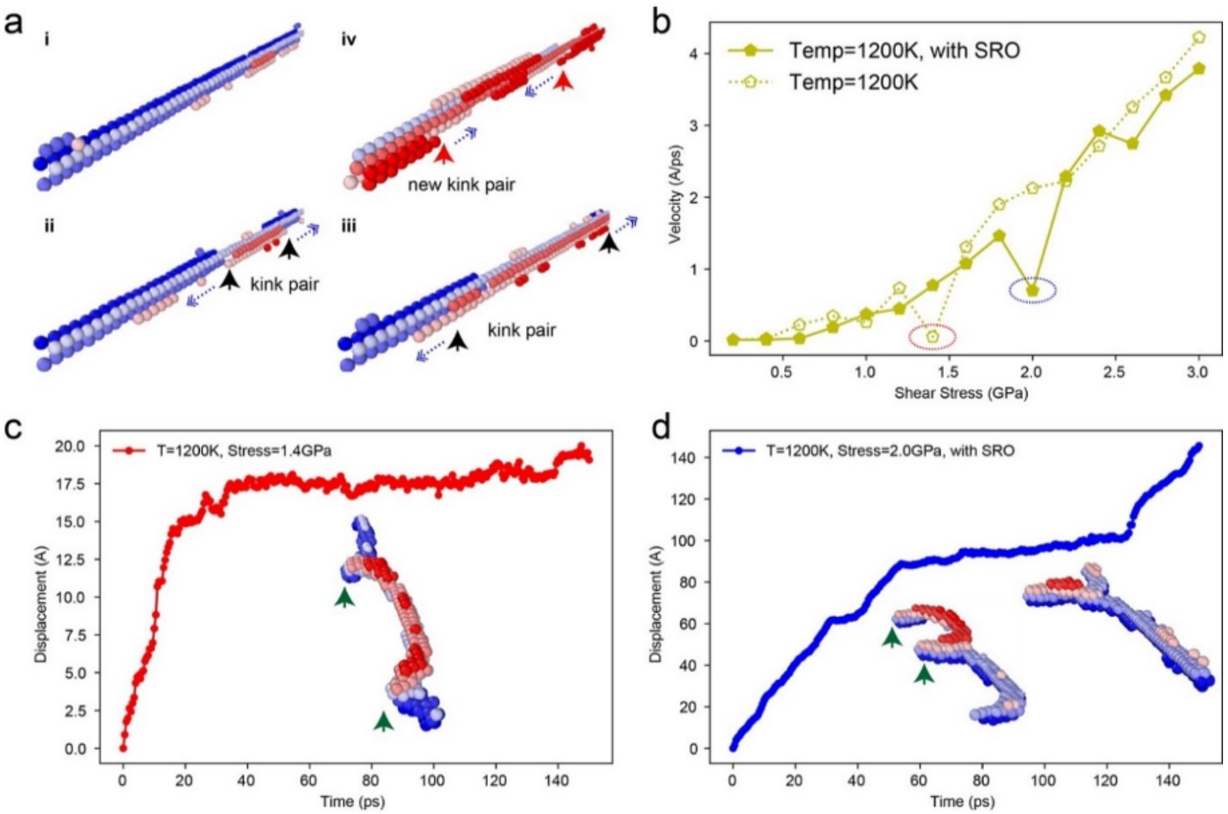

Figure 3.3: Kink nucleation mechanism and the observation of cross-slip locking providing extra strengthening during screw dislocation glide. a, Snapshots of atomic configurations along the screw dislocation, illustrating kink nucleation during glide. (i) The initial straight screw dislocation line. (ii) A kink pair nucleates (indicated by the black arrows) and migrates along the dislocation line (dashed arrow). (iii) Kink pair migration leads to net motion of the screw dislocation line. (iv) Another kink pair nucleates (indicated by the red arrows) and migrates. Only the dislocation core atoms are shown and the atoms are colored by coordinates in the glide direction $[1\bar{1}2]$. b, Simulation velocity vs. stress results for the screw dislocation at 1200K; the circles show anomalous points yielding significantly lower average velocity, associated with the formation of cross-slip locking. Details of the dislocation configurations are shown in c-d. c, Displacement vs. time curve of a screw dislocation under a shear stress of 1.4 GPa at 1200K in the random sample. The insert shows the formation of cross-slip locking during screw dislocation glide. d, Corresponding displacement vs. time curve of a screw dislocation under a shear stress of 2.0 GPa at 1200K in the SRO sample. The insert figure shows the formation and unlocking of cross-slip locking during screw dislocation glide. The atoms in (c-d) are colored by the coordinates in the slip plane direction $[\bar{1}10]$].

and can lead to debris such as vacancies, interstitials and prismatic loops, as described in theoretical modeling[6], kinetic MC simulations[185] and directly observed in TEM experiments[157]. However, the cross-slip jogs observed here are somewhat more complex than these previously defined cross-kinks and appear to resemble the cross-slip controlled Kear-Wilsdorf (KW) type locks found in long-range-ordered $L1_2$ intermetallics[186,187], as shown by the insets in Fig. 3.3c. Specifically, this figure displays the screw dislocation line with periodic boundary conditions where the atoms are colored by the height of the slip planes in $[\bar{1}10]$. In the inset, one segment of the dislocation line has moved to the upper slip plane by cross-slip, represented by the red color, and two jogs are created at the intersections between the cross-slipped segment and the original blue segment, as shown by the two arrows in the inset figure. Extra stress is then required to break or move these jogs, as shown in the Figure B.4. In this case, the whole dislocation line is immobile due to the pinned jogs during the entire simulation time after they form. In another simulation shown in Fig. 3.3d for the sample with SRO, where the shear stress is higher (2.0 GPa) we can observe the locking formation and self-unlocking during the simulation. From the displacement vs. time curve in Fig. 3.3d, the dislocation first glides at a constant velocity and then becomes immobile due to the locking, as shown by the insets in the figure. Because of the high applied shear stress in this case, after some time the jogs become automatically unlocked such that the screw dislocation can resume gliding. Similar to KW locks, the formation and breaking of such jogs would provide extra strengthening for the RHEA. From the theoretical model of Maresca and Curtin[6], the frequency of such cross-kinks depends on the ratio of the kink energy and the solute-dislocation interaction energy; accordingly, the formation of such cross-kinks and jogs (superkinks) would be expected to be easier in the RHEA concentrated solid-solution compared to pure *bcc* metals or dilute binary alloys. In addition, the intrinsic fluctuation in energy along the dislocation line and rugged energy landscape for screw dislocation segments in RHEAs has been observed in previous DFT and MD simulations[160,162,188]; this can further facilitate cross slip along the dislocation line and cause the formation of jogs, which strongly implies that cross-kink and cross-slip locking plays a more important role in the deformation and strengthening of RHEAs, as compared to pure single-phase *bcc* metals.

3.3.5 Phenomenological dislocation mobility model

In this section we consider further the effect of SRO on dislocation mobilities presented above, employing a phenomenological theoretical model for screw dislocation velocities. In this analysis we exclude the effects of the cross-slip locking and focus on the data associated with dislocation glide in the absence of such pinning events. The goal is thus to understand the temperature-dependent SRO effects associated with dislocation glide through the kink-nucleation and growth mechanism. The MD results are analyzed within the theoretical framework developed in previous work[189], which is extended to account for the effect of SRO on the free energy of kink-pair nucleation. In the low temperature and low stress regime, dislocation mobility is deemed to be governed by kink-pair nucleation and migration, with the Gibbs free energy for kink-pair formation, ΔG_{kp}, written as:

$$\Delta G_{kp} = \Delta H_{kp} - T\Delta S_{kp} \tag{3.3}$$

where ΔH_{kp} is the formation enthalpy, and ΔS_{kp} is the corresponding entropy. The formation enthalpy is usually written as:

$$\Delta H_{kp} = \Delta H_0 \left[1 - (\frac{\tau}{\tau_0})^p\right]^q \tag{3.4}$$

where ΔH_0 is a pre-factor related to the kink-pair formation energy, p and q are fitting parameters, τ is the applied shear stress and τ_0 is the Peierls stress. The entropy term ΔS_{kp} is simplified and approximated as a constant term by: $\Delta S_{kp} = \frac{\Delta H_{kp}}{T_0}$, where T_0 is a characteristic temperature dependent on the composition of the material. Thus, the free energy of kink-pair formation becomes:

$$\Delta G_{kp}(\tau,T) = \Delta H_0 \Big[\big[1 - (\frac{\tau}{\tau_0})^p \big]^q - \frac{T}{T_0} \Big] \tag{3.5}$$

For the RHEA with local chemical SRO, the nucleation of each kink-pair will break the local order and create a small segment of DAPB, which needs to be included in the Gibbs free energy term. Here, we add an extra term ΔH_{DAPB} to the free energy of kink-pair nucleation:

$$\Delta G_{kp}(\tau,T) = \Delta H_0 \Big[\big[1 - (\frac{\tau}{\tau_0})^p \big]^q - \frac{T}{T_0} \Big] + \Delta H_{\mathrm{DAPB}} \tag{3.6}$$

where $\Delta H_{\mathrm{DAPB}} = 0$ in the RSS sample, and ΔH_{DAPB} as a fitting constant for the sample with a fixed amount of SRO. The value of ΔH_{DAPB} should scale with γ_{DAPB} and the characteristic length scale of kink-pair nucleus, such as width and height of the kink-pair nucleus.

It is clear that for $\Delta G_{kp}(\tau,T) > 0$, the mobility is dominated by the kink-pair nucleation and migration mechanism. According to previous work[189], the velocity of the screw dislocation can be written as:

$$\nu(\tau,T) = \frac{\tau b}{B(\tau,T)} = \exp\big(- \frac{\Delta G_{kp}(\tau,T)}{2k_B T} \big) \tag{3.7}$$

Here, $B(\tau,T) = \frac{a\left[2a\exp\left(\frac{\Delta G_{kp}(\tau,T)}{2k_BT}\right)+L\right]}{2hL} B_k$, where a is the lattice parameter, k_B is the Boltzmann constant, L is the length of the screw dislocation line, h is height of a kink in the glide direction and B_k is a fitted kink drag coefficient. The effect of DAPB during kink-pair migration along the dislocation line is assumed to be small compared to the kink-pair nucleation; it is thus not included in the current model, which leads to a fixed B_k. As the stress and temperature increases, the $\Delta G_{kp}(\tau,T)$ term will decrease and dislocation motion will transfer into a phonon-drag regime, which leads to $\nu(\tau,T) = \tau b / B(\tau,T)$, with the classic drag coefficients as $B(\tau,T) = B_0 + B_1 T$, where B_0 and B_1 are fitting parameters. Here we have neglected the effect of the DAPB strengthening, which will be small relative to the values of τ where phonon drag is observed. In summary, the following phenomenological mobility law for screw dislocation motion is fitted to our simulation results:

$$\nu(\tau,T)=\begin{cases}\frac{\tau b}{B(\tau,T)}\exp\left(-\frac{\Delta G_{kp}(\tau,T)}{2k_BT}\right) & \text{if } \Delta G_{kp}(\tau,T)>0\\ \frac{\tau b}{B(\tau,T)} & \text{if } \Delta G_{kp}(\tau,T)\leq 0\end{cases} \tag{3.8}$$

$$B(\tau,T)=\begin{cases}\frac{a\left[2a\exp\left(\frac{\Delta G_{kp}(\tau,T)}{2k_BT}\right)+L\right]}{2hL}B_k & \text{if } \Delta G_{kp}(\tau,T)>0\\ B_0+B_1T & \text{if } \Delta G_{kp}(\tau,T)\leq 0\end{cases} \tag{3.9}$$

$$\Delta G_{kp}(\tau,T)=\Delta H_0\left[\left[1-(\frac{\tau}{\tau_0})^p\right]^q-\frac{T}{T_0}\right]+\Delta H_{\mathrm{DAPB}} \tag{3.10}$$

where a sigmoidal function centered around $\Delta G_{kp}(\tau,T)=0$ was used to interpolate the transition smoothly for $\nu(\tau,T)$ and $B(\tau,T)$.

The fitted velocity model is plotted with the simulation results in Fig. 3.4a. We note that the parameters in the phenomenological model used here to fit the MD data, such as kink-pair formation enthalpy, are effective values and do not represent the fact that these quantities will be possess a statistical distribution in a RHEA. To investigate the underlying physics of the temperature-dependent SRO effect that we observe from the MD-derived dislocation velocity data, we have included a SRO enthalpic term ΔH_{DAPB} in the free energy of kink-pair nucleation, to represent the extra energy required to disrupt the SRO during the kink-pair formation process. In so doing, we assume that the dominant effect of SRO is on the kink-pair formation energy, and neglect its effect on kink motion after formation.

With the fitted parameters from the RSS samples, we keep all other parameters in the model fixed and only fit the ΔH_{DAPB} for the SRO samples. Figure 4b shows the fitted model along with the simulation results for the systems with SRO. From the current model, ΔH_{DAPB} should be positively correlated with the degree of SRO in the sample; a higher value of ΔH_{DAPB} would lead to a higher SRO-strengthening effect. With respect to the temperature-dependence of the SRO effect, the mobility curves based on the model for two temperatures, 300K and 2000K, are plotted on Fig. 3.4c, with the dashed lines representing the RSS cases ($\Delta H_{DAPB} = 0$) and the solid lines considering the SRO effect ($\Delta H_{DAPB} = 4\%\Delta H_0$). The model also shows that at high temperature (2000K), the strengthening effect from SRO is significantly diminished compared to behavior at room temperature (300K), which is consistent with the MD results. Based on the model, we can attribute this attenuation to the thermal entropy term ΔS_{kp}. With increasing temperature, the contribution from ΔS_{kp} to the kink-pair formation free energy ΔG_{kp} increases linearly, causing ΔG_{kp} to decrease to zero at lower stresses as the temperature is raised. The contribution of ΔH_{DAPB} will thus be weakened due to the larger contribution from the entropy term at high temperatures, and this is reflected in the dislocation mobility curves in Fig. 3.4c. In summary, in this section, we have fit screw dislocation mobility laws in the MoNbTaW-RHEA with a phenomenological model that includes the effect of SRO on the formation energy for a double kink. The strengthening induced by the presence of the local chemical SRO is found to be highly temperature-dependent; specifically, it is found to decrease at high homologous temperatures.

3.3.6 Edge dislocation velocities and the influence of SRO

We consider next MD results for edge-dislocation motion in both RSS and SRO samples. Figure 3.5 shows the MD simulation results over a range of temperatures. Figure 3.5a represents the mobility data in the RSS sample with the stress ranging from 0 to 1.0 GPa, at temperatures from 300K to 2000K, with Fig. 3.5b representing results for the sample with SRO. Comparing the behavior of the screw and edge dislocation, it is clear that the mobility of the edge dislocations is much higher than that of the screw dislocations under similar applied stresses. Different from the kink-pair nucleation mechanism in screw dislocations, the glide of edge dislocations in *bcc* metals is generally believed to be governed by solute drag, phonon drag and wave speed limitation over different velocity regimes[190].

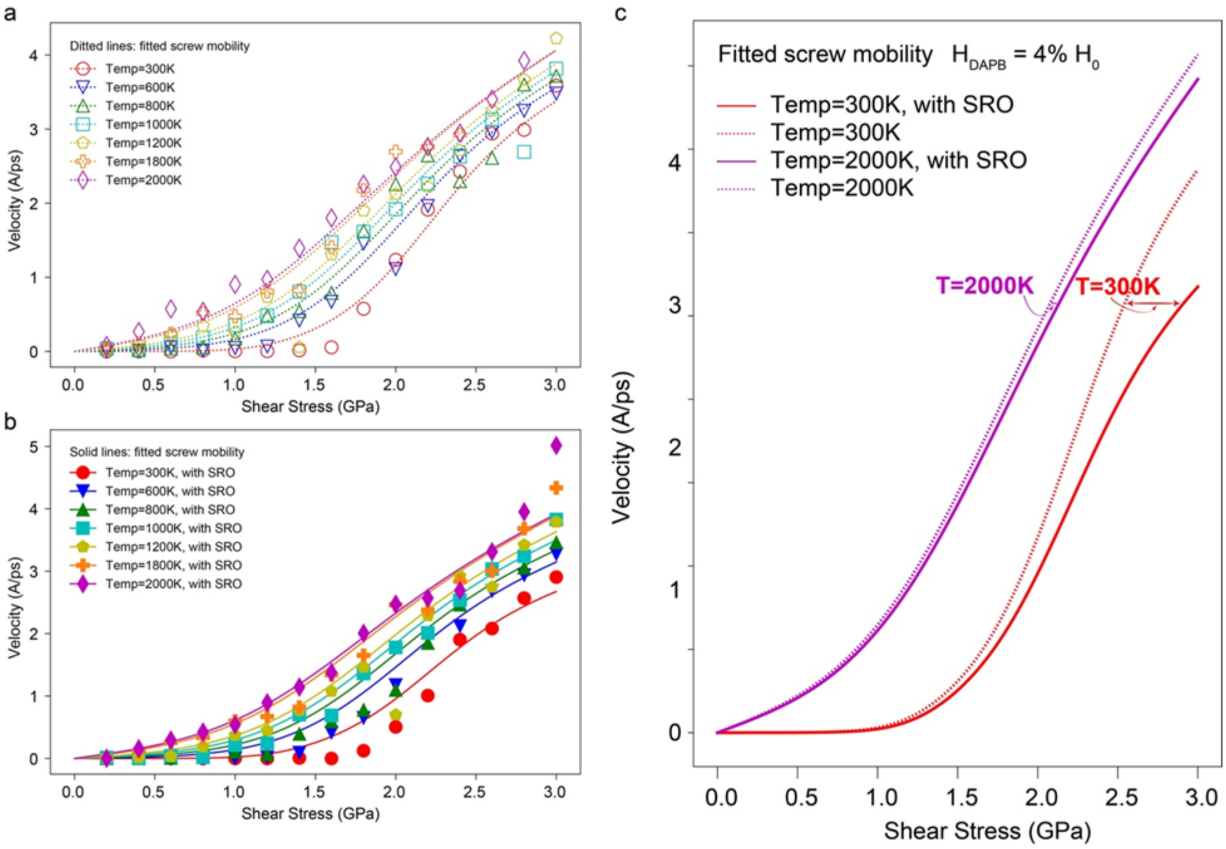

Figure 3.4: Fitted screw dislocation mobility model and the influence of thermal entropy on the SRO strengthening effect. a, Velocity vs. stress results over a range of temperatures for screw dislocation in the RSS sample. The open symbols are the simulation data, and the dashed lines are the fits of the phenomenological model described in the text. b, Velocity vs. stress results over a range of temperatures for screw dislocation in the systems with SRO. The solid lines are the fitted screw mobility based on the phenomenological model with the ΔH_{DAPB} term included in the kink-pair formation free energy. c, The influence of temperature on the SRO strengthening of the screw dislocation. Solid lines represent the fitted model results for the sample with SRO and the dashed lines represent the fitted model for the RSS sample. The strengthening effect due to SRO attenuates when temperature increases from 300K to 2000K.

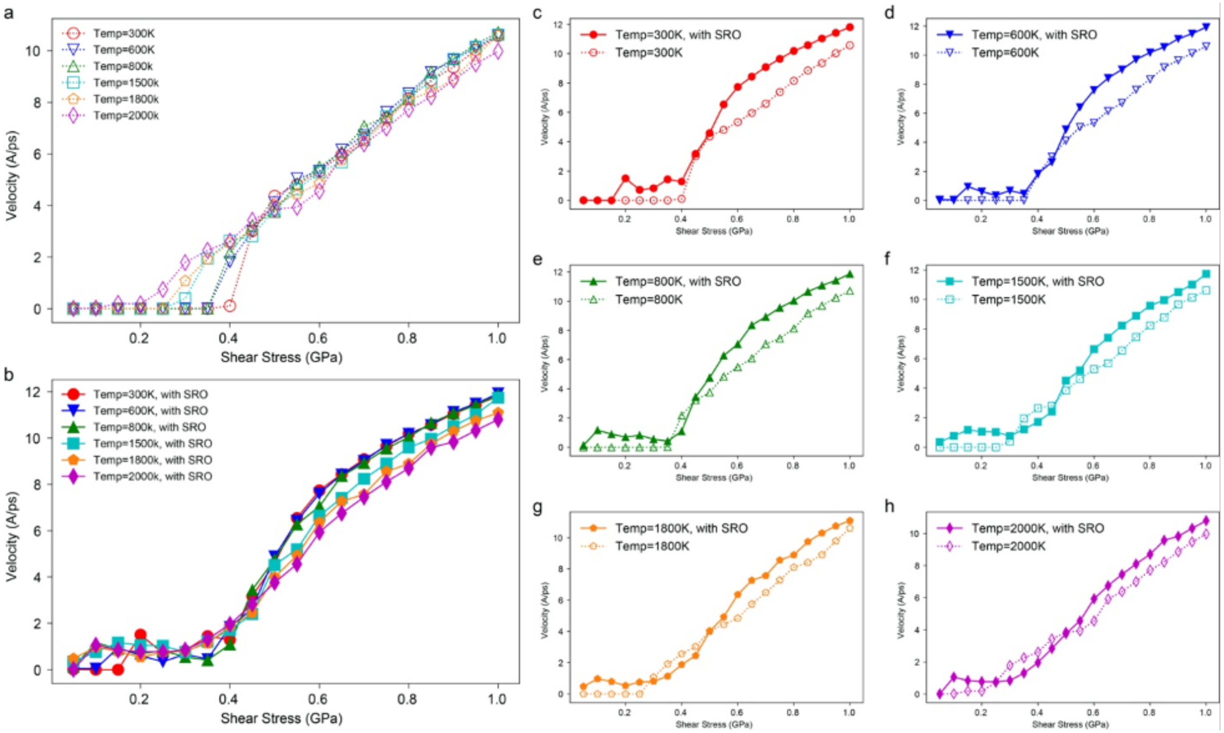

Figure 3.5: Simulation results illustrating the effect of SRO on the velocities of edge dislocations as a function of applied shear stress over a range of temperatures. a Velocity vs. stress results from the simulations of edge dislocations in the RSS sample are shown with open symbols with data for each temperature connected by dashed lines that represent guides to the eye. b Similar results as in panel (a), but for edge dislocations in the sample with chemical SRO. c-h Detailed comparisons of the influence of SRO at representative temperatures, from 300K to 2000K.

The influence of SRO on the edge dislocation mobility is investigated by comparing the mobility curves in Fig. 3.5a and b. For both low and intermediate stress regimes, the edge dislocation mobilities for the system with SRO differ significantly from those in the RSS sample. In the low stress regime, the glide of an edge dislocation in the RSS sample shows the "friction stress" effect, where the dislocation stays immobile until the applied shear stress exceeds a critical value; this critical stress decreases as the temperature increases. A similar phenomenon has been observed in other alloy systems[180,191,192], which can be attributed to the pinning of the dislocation due to the collective interaction of random solute atoms. However, in Fig. 5b, with the presence of SRO, the friction phenomenon is not as effective as in the RSS sample. Instead, the edge dislocation is not immobile, but glides at a very low velocity (¡ 2 Å/ps) in the low stress regime. This is in contradiction with previous understanding that the onset of dislocation glide necessitates the break-up of local order on the slip plane, which requires extra energy and stress. Consequently, there must be another competing mechanism that enhances the dislocation mobility through the SRO at the same time.

A detailed comparison of edge dislocation velocities at different temperatures in Fig. 3.5c-h reveals that in the high stress regime, the influence of SRO on the motion of the edge dislocation is the direct opposite from that for the screw dislocation, in that the mobility of the edges is enhanced in the SRO sample compared to that in the RSS sample. It is important to note, however, that in the simulations in the high stress regime, the edge dislocation must glide through the periodic boundary multiple times, such that the SRO on the specific slip plane will have already been destroyed after the edge first crosses through the cell. Nevertheless, although the local slip plane becomes randomized, there is still a significant difference in the velocities of the edge dislocation in the SRO versus the RSS samples, such that we conjecture that the SRO in the neighboring planes could influence the edge dislocation even when the order on the glide plane has been disrupted by dislocation motion. In this case, there is then the question of how the existence of SRO can influence edge dislocation mobility and what characteristic length-scale is associated with the influence of SRO for an edge dislocation.

One reasonable hypothesis is that the existence of SRO can also influence the solute interactions and, as such, lower the solute drag effect to enhance the mobility of the edge dislocation. From the nature of SRO, the ordered sample will always have lower configurational energy; furthermore, our previous DFT study showed a flattened energy landscape for the screw dislocation cores in the RHEA due to the presence of SRO[162], which can be assumed also to be of relevance to edge dislocations. Here, the effect of SRO inducing a considerably flattened energy landscape (lower solute drag effect) could offset the extra energy cost to create a DAPB, such that the dislocation mobility will be enhanced by SRO to give a lower friction effect and higher averaged velocity.

Accordingly, additional simulations were conducted to substantiate the hypothesis. We show in Fig. 3.6a-b schematics representing the state of SRO in the sample, where the dashed lines represent the atomic planes, the blue section represents a region where equilibrated SRO is maintained, and the cyan represents regions where the SRO has been destroyed. For the system with SRO, when the edge dislocation crosses through the periodic boundary multiple times, as noted above, the order on its slip plane actually has already been destroyed, but the solute configurations of the atoms in the neighboring regions still display SRO, as shown in Fig. 3.6a. In addition to comparing with the fully RSS sample, we can manually randomize several layers of atoms around the original slip plane to create an RSS region of limited size. Specifically, if n layers of atoms are randomized, $n+1$ layers of ordering will be destroyed, as illustrated in Fig. 3.6b. Thus, for the additional simulations, 1, 2 and 4 layers of atoms are manually randomized to create an RSS region of limited size so that the average edge dislocation velocity within these regions can be calculated and compared with the samples with complete SRO and the RSS samples.

Figure 3.6c shows the position vs. time curves of an edge dislocation in the five different samples described above with an applied 0.6 GPa shear stress at 300K. The fitted average

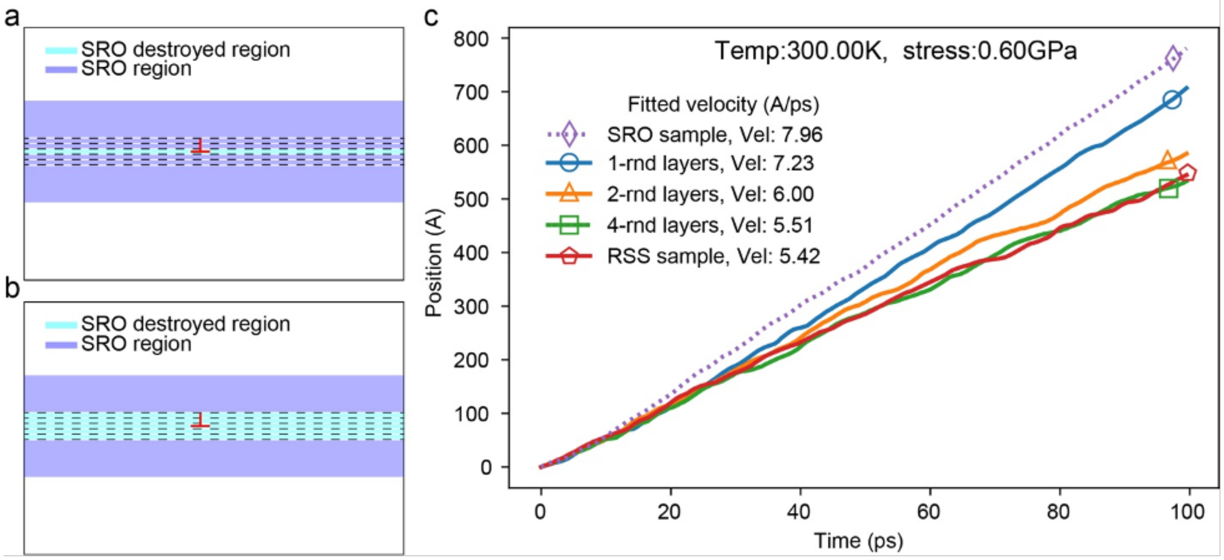

Figure 3.6: Attenuated drag effect for the edge dislocation induced by SRO in layers neighboring the guide plane. a, The schematic figure illustrates the state of SRO in the sample. The edge dislocation is represented in red, indicating the position of the glide plane, and the dashed lines are the corresponding atomic planes parallel to the guide plane. The cyan color represents that the SRO on the slip plane has been destroyed after the edge dislocation glides across the whole periodic cell. The blue regions reflect planes where the SRO remains present. b, This panel represents the situation for simulations in which SRO is destroyed not only along the slip plane, but in neighboring parallel planes. c, The effect of the SRO state around the neighboring slip planes of the edge dislocation motion (distance vs. time). The dashed line represents the average velocity of the edge dislocation in a sample where SRO is destroyed only within the guide plane (corresponding to panel (a)). The solid lines represent the edge dislocation motion in the samples with controlled number of destroyed SRO layers, i.e., for different thicknesses of the cyan region in panel (b). Also shown are results obtained for the RSS sample where SRO is not present on any planes in the system.

dislocation velocities are shown in the inset to Fig. 3.6c. It is observed that the dislocation velocity is highest in the sample with full SRO, i.e., only order on the slip plane has been destroyed. With more layers of atoms around the slip plane being randomized, the RSS region becomes thicker and the average dislocation velocity keeps decreasing. When four layers of atoms are randomized in the SRO sample, the thickness of the RSS region is 1.2 nm and the average velocity of the dislocation nearly converges to the velocity in the sample with complete random disorder. This result confirms our hypothesis that SRO would reduce the solute drag interaction for the edge dislocation, and shows that this effect extends to a characteristic length scale of $\sim$1.2 nm. Thus, different from the strengthening effect due to SRO for screw dislocations, the existence of SRO is found to enhance the mobility of edge dislocations in the RHEA.

3.3.7 Mobility of screw vs. edge dislocations in the MoNbTaW-RHEA and pure Mo and Nb metals as a function of temperature

In addition to the RHEA, the dislocation mobilities in pure Mo and Nb are also calculated for reference, in the same manner described in the Methods section using the MTP. Figure 3.7a displays the mobility of the edge dislocation in the RSS RHEA as compared to pure Mo and Nb at temperatures of 300K and 2000K. The most notable difference in this comparison is that there is no threshold stress effect in the pure metals, associated with solute drag. The mobilities in Mo and Nb show a significant influence of phonon drag, which increases with increasing temperature. The mobility in Mo is much lower than that in Nb but still higher compared to the RSS-RHEA. However, this difference in dislocation mobility in the RHEA and Mo diminishes as the temperature is increased; specifically, the velocity difference between the RHEA and pure metal is far smaller at 2000K than that at 300K.

Figure 3.7b shows the velocity results for screw dislocations in the RSS-RHEA as compared to pure Mo and Nb at temperatures of 300K and 2000K. Since the glide of screws is dominated by kink-pair nucleation, the motion in both the RHEA and the pure metals display the

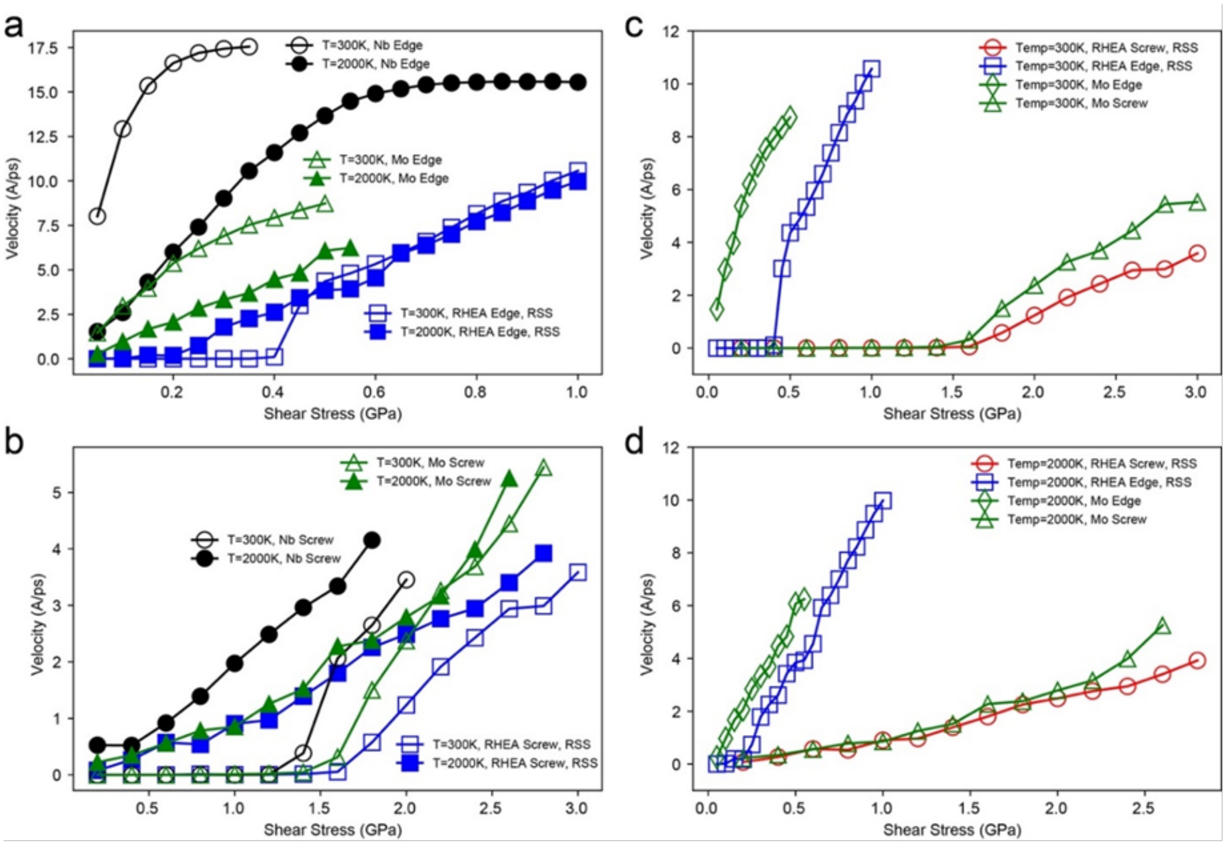

Figure 3.7: Comparison of the simulation results for dislocation velocities for edge and screw dislocations in the MoNbTaW RHEA and pure Mo and Nb *bcc* metals at different temperatures. Velocity as a function of stress for a, edge dislocations and b, screw dislocations in the RHEA and pure Mo and Nb at temperatures of T = 300K and 2000K. Velocity as a function of stress for edge and screw dislocations in the RHEA and pure Mo at temperatures of c, 300K and d, 2000K. In all of the results the symbols are simulation data and the solid lines are guides to the eye, connecting results for a given dislocation character (edge or screw) and given temperature.

friction effect at 300K, although the friction stress disappears at 2000K in all cases. Similar to the edge dislocation, the velocities of the screw dislocations in the RHEA are lower than those in Mo and Nb at 300K. However, the difference in screw dislocation velocity in the RHEA and in Mo almost vanishes at this higher temperature.

Summarizing, at low temperature (300K) the mobility of both the edge and screw dislocations shows significant differences in the RHEA compared to that in the pure *bcc* metals. However, at high temperature (2000K), the mobility curves of the screw dislocation in the RHEA and pure Mo are almost identical, although the mobility of the edge dislocation in RHEA is still lower than that in the pure metals as it retains some friction stress due to the solute drag effect.

One might ask what the relevance is of such observations. RHEAs have been actively investigated due to their demonstrated high elevated-temperature strength[193] although the precise physical origins are still not fully understood. For pure *bcc* metals, it is well known, e.g., from in situ TEM experiments[183,194,195], that edge dislocations play a minor role in strengthening at low and moderate temperatures due to their higher mobility. However, from recent studies for *bcc*-RHEAs, the role of the edge dislocations is now believed to play a more important role in the high-temperature regime[158,161,196]; additionally, a large fraction of non-screw segments has been observed during the glide of dislocations in such alloys[153]. In this work, we have calculated the mobility of screw and edge dislocations over a wide range of temperatures in such a RHEA and have shown that the mobility of the edge dislocations does decrease with increasing temperature due to phonon drag; moreover, at the same time the mobility of the screw dislocations is found to increase with temperature due to a lowering of the free-energy barrier for kink-pair nucleation.

Figure 3.7c-d shows the representative velocity versus stress curves for screw and edge dislocations in the MoNbTaW and Mo at 300K and 2000K. The ratio of the edge-to-screw velocities does indeed decrease as the temperature is raised, as can be seen by the fact that the angle between the velocity versus stress curves for the screw and edge dislocations in MoNbTaW becomes smaller from Fig. 3.7c to Fig. 3.7d. The edge-to-screw mobility ratio is around 20 at

300K, which decreases to 11 when temperature is raised to 2000K. However, the mobility of the edge dislocation remains much higher than that of the screw dislocation. The discrepancy between the current edge-to-screw velocity ratios compared with the CoFeNiTi system studied in previous work[196] might be due to the different levels of lattice distortion in the two alloy systems. A similar trend in decreasing mobility ratios with increasing temperature is also observed in pure Mo, as shown in Fig. 3.7c-d, which indicates that this is not a unique feature of RHEAs. One significant temperature-dependent property that differentiates the mobility of screw and edge dislocations, which is also a unique property in the RHEAs, is the enhanced friction stress. For edge dislocations, the friction is zero in pure metals for edge dislocations, whereas due to solute drag interactions we can clearly observe a temperature-dependent friction stress for edge in the RHEA, as shown in Fig. 3.5a and Fig. 3.7. For screw dislocations, the friction phenomenon is due to the energy barrier associated with kink-pair nucleation, which holds for both pure metals and RHEAs. Accordingly, the differing mechanisms of the friction effect for edge and screw dislocations naturally leads to different dependences of the critical friction stress on temperature. Here, the critical friction stress is determined as the stress for which the velocity reaches 0.2 Å/ps for screw dislocations and 1.0 Å/ps for edge dislocations.

Figure 3.8a shows the critical stress as a function of temperature for the screw dislocation in the RSS-RHEA, which are fit well by an exponential decay curve, whereas in Fig. 3.8b, the critical stress for the edge dislocation is well fit by a function that decreases linearly with temperature. Moreover, the critical stress for the screw dislocation is more sensitive to the increment of temperature and, as such, decays at a much higher rate compared with the edge dislocation. According to our simulation data, from 300K to 2000K the critical friction stress decreases by 140 MPa for the edge dislocation, whereas the decrease is almost an order of magnitude larger at 1.3 GPa for the screw dislocation. Although the initial friction is much higher for the screw dislocation at room temperature, the screw and edge critical stresses decay to approximately the same level at roughly 2000K (Fig. 3.8c).

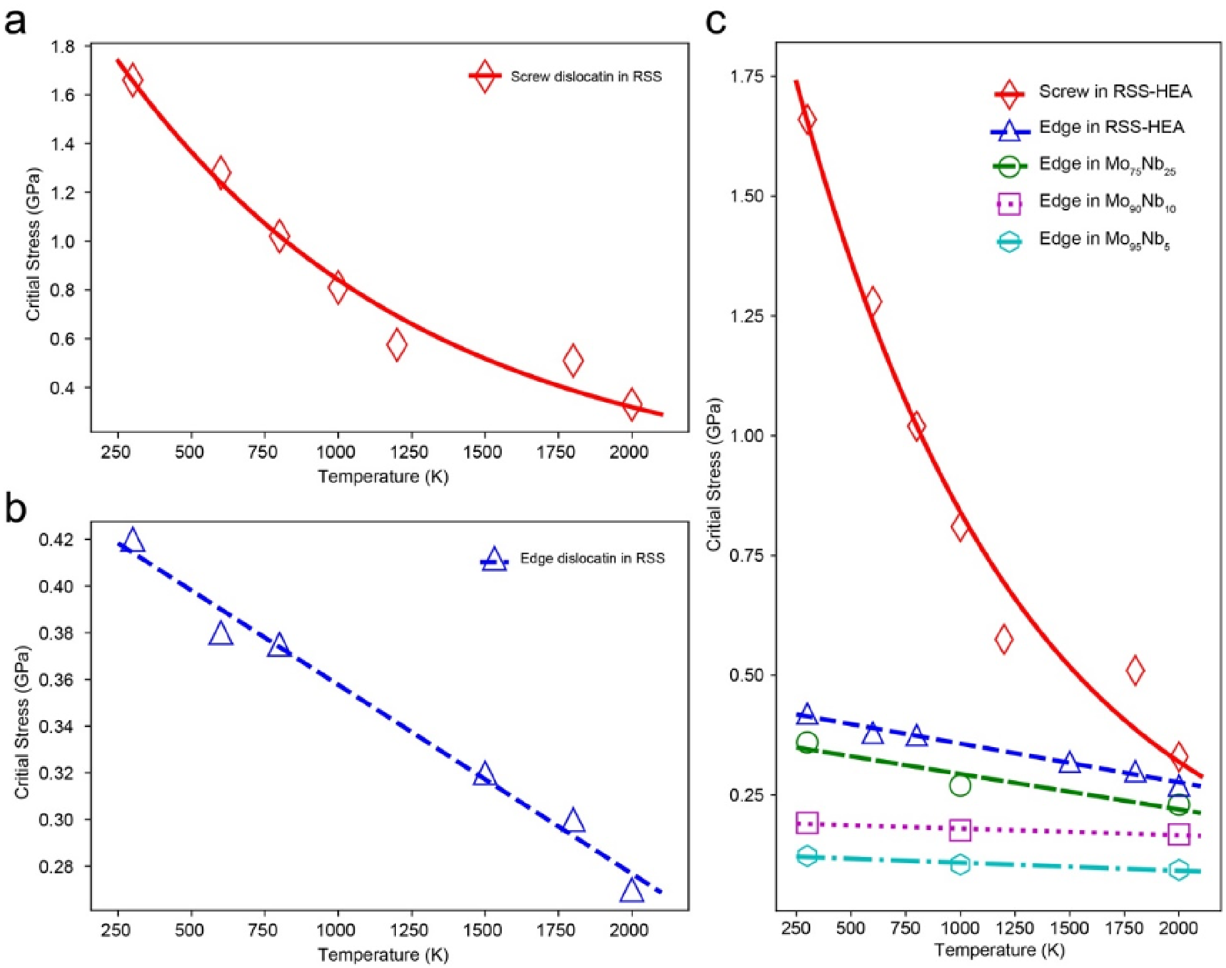

Figure 3.8: Critical friction stress as a function of temperature for screw and edge dislocations. a, Critical stress as a function of temperature for the screw dislocation in RSS samples obtained from MD simulations (open symbols), fitted with an exponential function (solid line). b, Critical stress as a function of temperature for the edge dislocation in RSS samples obtained from MD simulations (open symbols), fitted with a linear function (solid line). c, Comparison of critical stresses for screw and edge dislocations as a function of temperature. The critical stresses for edge dislocations in Mo-Nb binary alloys are included for comparison.

For comparison and to further show the unique features of the RHEA, we also calculated friction stresses of some binary alloys through same procedures, from $Mo_{95}Nb_5$ to $Mo_{75}Nb_{25}$. Figure 3.8c shows that the overall values of the critical friction stresses in the binary alloys are lower compared with the RHEA, and the slope of the critical stress is also decreasing with decreasing solute concentration, where the friction stress is expected to converge to horizontal line with zero friction stress in the pure *bcc* metal for edge dislocation motion. However, due to the kink nucleation barrier, the screw dislocation will still maintain an observable level of critical friction stress in the pure *bcc* metal.

3.4 Conclusion

In summary, we have developed a new machine-learning interatomic potential and used it as the basis for systematic MD studies of the mobility of edge and screw dislocations over a wide range of temperatures in a *bcc* MoNbTaW refractory high-entropy alloy (RHEA). Screw dislocations in the MoNbTaW RHEA move through kink-pair nucleation and migration; additionally, a cross-slip locking mechanism is observed in the simulations, which can be attributed to the intrinsic fluctuation of energy along the dislocation line and rugged energy landscape in the system, which will provide extra strengthening to the RHEA. Short-range order (SRO) is found to induce a temperature-dependent strengthening effect on the screw dislocations moving through the kink-pair nucleation mechanism, while accelerating the edge dislocation movement through an attenuation of the magnitude of the solute interactions. A phenomenological model for the mobility of screw dislocations has been constructed to reveal the origin of the temperature-dependent SRO effect for screw dislocation motion through kink-nucleation mechanism, which arises from the contribution of SRO to the free energy barrier for kink-pair nucleation. With increasing temperature, a reduced edge-to-screw mobility ratio was discovered in both pure *bcc* metals and in the MoNbTaW-RHEA. A different temperature sensitivity for the critical stress to initialize dislocation motion is found but only in the RHEA; the critical friction stress for the edge dislocation decays much slower than it does for the screw dislocation with increasing temperature, and it becomes comparable in magnitude for both edge and screws at 2000K. These findings demonstrate the salient mechanisms and specific influences of temperature and local chemical order on the mobility of edge and screw dislocations in RHEAs, all of which can have a significant impact on the mechanical properties of RHEAs.

Chapter 3 presents a study on mechanism of plastic deformation of *bcc* refractory high-entropy alloy (RHEA) system MoNbTaW driven by ML-IAPs. The ML-IAP enabled us to perform MD simulations of over 500,000 atoms for understanding the mobility of edge/screw dislocation with respect to temperature and the presence of short-range order (SRO).

Chapter 4

Accelerating materials discovery with bayesian optimization and graph deep learning

4.1 Introduction

The accurate prediction of novel stable crystals and their properties is a fundamental goal in computation-guided materials discovery. While *ab initio* approaches such as density functional theory (DFT)[1,2] have been phenomenally successful in this regard[53,197–199], their high computational cost and poor scalability have limited the broad application across vast chemical and structural spaces. As a result, high-throughput DFT screening has been mostly performed on $\sim O(100-1000)$ crystals with relatively small unit cells.

To circumvent this limitation, machine learning (ML) has emerged as a new paradigm for developing efficient surrogate models for predicting materials properties at scale.[200–205] Such ML models are usually trained on large databases of materials properties[57–59] to learn the relationship between input chemical and/or structural features and target properties (e.g., formation energies, band gaps, elastic moduli, etc.). Only ML models utilizing structural as well as chemical features can distinguish between polymorphs and be universally applied in materials discovery across diverse crystal structures. In particular, graph neural networks, where atoms and bonds in crystals are represented as nodes and edges in a mathematical graph, have emerged as a particularly promising approach with state-of-the-art accuracy in predicting a broad range of energetic, electronic and mechanical properties.[66,67,69–72,206,207]

Ironically, a critical bottleneck in the application of structure-based ML models for materials discovery is the requirement for equilibrium crystal structures as the inputs. These are obtained by "relaxing" initial input structures along their potential energy surfaces, which are typically computed via expensive DFT calculations. While there have been recent efforts[208,209] at deriving accurate interatomic forces from graph representations, the application has been limited to a few molecular systems or constrained chemical spaces.

Here, we propose a Bayesian Optimization With Symmetry Relaxation (BOWSR) algorithm to obtain equilibrium crystal structures for accurate ML property predictions without DFT.

Utilizing a highly efficient MatErials Graph Network (MEGNet) formation energy model,[72] we demonstrate that BOWSR-relaxed structures can serve as accurate inputs to ML property models, yielding far higher accuracy in the prediction of various materials properties. Finally, we demonstrate the power of this approach by screening ∼400,000 transition metal borides and carbides for ultra-incompressible hard materials. Two new materials with relatively low predicted energy above hull[60] were successfully synthesized and demonstrated to have exceptional mechanical properties, in line with the ML prediction.

4.2 Methods

4.2.1 Bayesian optimization with symmetry relaxation algorithm

Geometry relaxation of a crystal structure requires the optimization of up to $3N+6$ variables - six lattice parameters and three fractional coordinates for each of the N atoms. By constraining the symmetry to remain unchanged during relaxation can reduce the number of independent variables considerably.[50,210,211] The open-source *spglib*[212] package was used for symmetry determination. The search for optimized symmetry-constrained lattice parameters and atomic coordinates that minimize the total energy was then carried out via Bayesian optimization (BO). The changes in the variables were used as the optimization inputs to reduce the tendency of the BO process being dominated by parameters with large magnitudes. This approach has been previously used for geometry optimization along the imaginary phonon modes.[211]

Using a Latin hypercube sampling, a set of training observations $D \sim \{(x_i, U(x_i))\ i = 1 : m\}$ were initialized, where the x_i are the m independent lattice parameters and atomic coordinates and $U(.)$ is the energy of the corresponding structure evaluated by the surrogate model (see Equations 4.4 and 4.5). The BO strategy comprises two steps[213]:

1. A Gaussian process (GP) model is trained on the initialized training observations D to

approximate the $U(x)$. The Rational Quadratic kernel[214] is adopted as the covariance function of GP. The noise level of GP model is set to the root mean square error (RMSE) of the energy model.

2. The acquisition function that balances the exploitation and exploration is calculated for samples in the search space apart from the training observations and the candidate with optimal acquisition function is proposed to be evaluated (formation energy prediction by surrogate ML model). Exploitation represents the samples with high predicted mean from the GP, and exploration accounts the samples with high predictive uncertainty.[215–217] Here, we chose the expected improvement as the acquisition function, which can be analytically expressed as[218,219]:

$$E[I(x)] = (\mu(x) - U(x^{+}) - \xi) \cdot \Phi(Z) + \sigma(x) \cdot \phi(Z) \tag{4.1}$$

and

$$x^{+} = \underset{i=1,\ldots,n}{\operatorname{argmax}} U(x_i) \tag{4.2}$$

$$Z = \frac{\mu(x) - U(x^{+}) - \xi}{\sigma(x)} \tag{4.3}$$

where $\mu(x)$ and $\sigma(x)$ are the mean and standard deviation of the posterior distribution on x from the GP, respectively, and $\Phi(x)$ and $\phi(x)$ are the cumulative distribution function (CDF) and probability density function (PDF), respectively. The ξ parameter can be tuned to balance the trade-off between the first term (exploitation) and the second term (exploration) in Equation (4.1). Until the maximum number of iteration steps is reached, the sample with optimal acquisition function was iteratively augmented to the training observations and used to update the GP surrogate model in the next loop.

It should be noted that by removing the symmetry constraint, i.e., treating all crystals as having triclinic $P1$ symmetry, the BO yields much higher errors (see Figure C.1) than that with symmetry constraints. This can be attributed to the limitation of BO in optimizing the high dimensional parameter space that scales linearly with the number of atoms in crystals without symmetry. In this work, the number of initialized training observations and the maximum number of iterations were both set at 100 to achieve the best trade-off between accuracy and efficiency (see Figure C.1). For property predictions, ξ was set to 0 as the dataset has been well explored by DFT calculations. For the discovery of new incompressible materials, ξ was set at 0.1 to allow the BO to have a higher likelihood of finding the global energy minimum in the exploration space with higher predictive uncertainty. In addition, the search space for optimized changes in the fractional coordinates, lattice lengths, and lattice angles variables was set to 0.2, 1.2 Å, and 5°, respectively. This search space is sufficiently large to have a reasonably high likelihood of including the global energy minimum while not overly large to be computationally intractable.

4.2.2 Materials graph network models

The Materials Graph Network (MEGNet) models used in this work are based on the same architecture as our previous work.[72] Briefly, three graph convolutional layers with [64, 64, 32] neurons were used in each update function, and the shifted softplus function was used as the non-linear activation function. A set2set readout function with two passes was used after the graph convolution steps. The cutoff radius for constructing the neighbor graph was 5 Å. The MEGNet formation energy (E_f) and elasticity (K_{VRH} and G_{VRH}) models were trained using the 2019.4.1 version of Materials Project database[57] containing 133,420 structure-formation energy and 12,179 structure-bulk/shear modulus data pairs. Each dataset was split into 80%:10%:10% train:validation:test ratios. During the model training, we used a batch size of 128 structures, and set the initial learning rate to 0.001 in the Adam optimizer. All models were trained for a maximum of 1500 epochs with an early stopping callback, which terminates the model training if the validation error does not reduce for 500 consecutive steps. The mean absolute errors (MAEs) of E_f, $\log_{10}(K_{\text{VRH}})$ and $\log_{10}(G_{\text{VRH}})$ models in test data are 26 meV atom^{-1}, 0.07, and 0.12, respectively.

4.2.3 DFT calculations

The DFT relaxations, energy and elastic tensor calculations for the small number of candidates that passed the ML screening were carried out using Vienna *ab initio* simulation package (VASP)[105] within the projector augmented wave approach.[106] The exchange-correlation interaction was described using the Perdew-Burke-Ernzerhof (PBE) generalized gradient approximation (GGA)[107] functional for structural relaxations and energy calculations. The plane wave energy cutoff was set to 520 eV, and the k-point density of at least 1,000 per number of atoms was used. All structures were relaxed with energies and forces converged to 10^{-5} eV and 0.01 eV/Å, respectively, consistent with the calculation setting used in the Materials Project.[57] The elastic tensor calculations were performed using the procedure described in previous work.[220] A tighter energy convergence criterion of 10^{-7} eV was used, and strains with magnitude of (-1%, -0.5%, 0.5%, 1%) were applied to each of the 6 independent components of strain tensor.

4.2.4 Synthesis

Bulk specimens of candidates ReOsB, ReOsB_2, MoWC_2, ReWB, $\text{Re}_{13}\text{WB}_9$, OsWB, $\text{Re}_6\text{W}_7\text{B}_8$, and ReW_2B_2 were synthesized via *in-situ* reactive spark plasma sintering (SPS). Elemental powders of Mo, W (>99.5% purity, ∼325 mesh, Alfa Aesar), Re (∼99.99% purity, ∼325 mesh, Strem Chemicals), Os (∼99.8% purity, ∼200 mesh, Alfa Aesar), boron (∼99% purity, 1-2 μm, US Research Nanomaterials), and graphite (∼99.9% purity, 0.4-1.2 μm, US Research Nanomaterials) were utilized as precursors. For each composition, stoichiometric amounts of elemental powders were weighted out in batches of 5 g. The powders were first mixed by a vortex mixer, and then high energy ball milled (HEBM) in a Spex 8000D mill (SpexCertPrep) by tungsten carbide lined stainless steel jars as well as 11.2 mm tungsten carbide milling media (ball-to-powder ratio $\approx$ 4.5:1) for 50 min. 0.05 g or $\sim$1 wt% of stearic acid was used as lubricant in the milling process. After HEMB, the as-milled powder mixtures were loaded into 10 mm graphite dies lined with graphite foils in batches of 2.5 g, and subsequently consolidated into dense pellets via SPS in vacuum ($< 10^{-2}$ Torr) by a Thermal Technologies 3000 series SPS machine. The HEBM and powder handing were conducted in an argon atmosphere (with O_2 level < 10 ppm) to prevent oxidation.

During the SPS, specimens were initially heated to 1400 °C at a rate of 100 °C/min under constant pressure of 10 MPa. For the final densification, the temperature was subsequently raised at a constant rate of 30 °C/min to a final isothermal sintering temperature, which was set at different levels for different target compositions — 1800 °C (ReWB), 1700 °C ($MoWC_2$ and $Re_6W_7B_8$), 1600 °C ($Re_{13}WB_9$ and ReW_2B_2), or 1500 °C (ReOsB, $ReOsB_2$, and OsWB), and maintained isothermally for 10 min. Meanwhile, the pressure was increased to 50 MPa at a ramp rate of 5 MPa/min. The final densification temperature was optimized for each specimen to achieve a high relative density while prevent specimen melting due to overheating. The *in-situ* reactions between elemental precursors likely took place during the initial temperature ramping. After sintering, the specimens were cooled down naturally inside the SPS machine (with power off).

4.2.5 Experimental characterization

Sintered specimens were first ground to remove the carbon-contaminated surface layer from the graphite tooling, and polished for further characterizations. X-ray diffraction (XRD) experiments were conducted using a Rigaku Miniflex diffractometer with the Cu Kα radiation at 30 kV and 15 mA. The Vickers microhardness tests were carried out on a LECO diamond microindentor with loading force varying from 0.49 N (50 gf) to 9.8 N (1 kgf) and constant holding time of 15 s, abiding by the ASTM Standard C1327. Over 20 measurements at different locations were conducted for each specimen at each indentation load to ensure statistical validity and minimize the microstructural and grain boundary effects. In particular, over 30 measurements were conducted for each specimen at 9.8 N indentation load.

The Young's and shear moduli of the specimens were calculated from the ultrasonic velocities measured with a Tektronix TDS 420A digital oscilloscope, following the ASTM standard A494-15. Multiple measurements were conducted at different locations.

4.3 Results

4.3.1 Bayesian optimization with symmetry relaxation algorithm

Bayesian optimization (BO) is an adaptive strategy for the global optimization of a function. In crystal structure relaxation, the function to be optimized is the potential energy surface, which expresses the energy of the crystal as a function of the lattice parameters and atomic coordinates. In the BOWSR algorithm, the symmetry (space group) of the lattice and the Wyckoff positions of the atoms are constrained during the relaxation process, i.e., only the independent lattice parameters and atomic coordinates are allowed to vary. The BO goal is then the minimization of the following mapping:

$$x := \{a, b, c, \alpha, \beta, \gamma, \vec{c}_1, \vec{c}_2, ...\} \tag{4.4}$$

$$x_{\mathrm{opt}} = \underset{x}{\operatorname{argmin}}\, U(x), U : R^n \to R \tag{4.5}$$

where $\{a, b, c, \alpha, \beta, \gamma\}$ and $\{\vec{c}_1, \vec{c}_2, ...\}$ represent the independent lattice parameters and the atomic positions for a $P1$ crystal, respectively, and $U(.)$ is the energy of the system. The schematic of the BOWSR algorithm as well as two examples of the geometry parameterization for a high-symmetry cubic crystal and a low-symmetry triclinic crystal are shown in Figure 4.1.

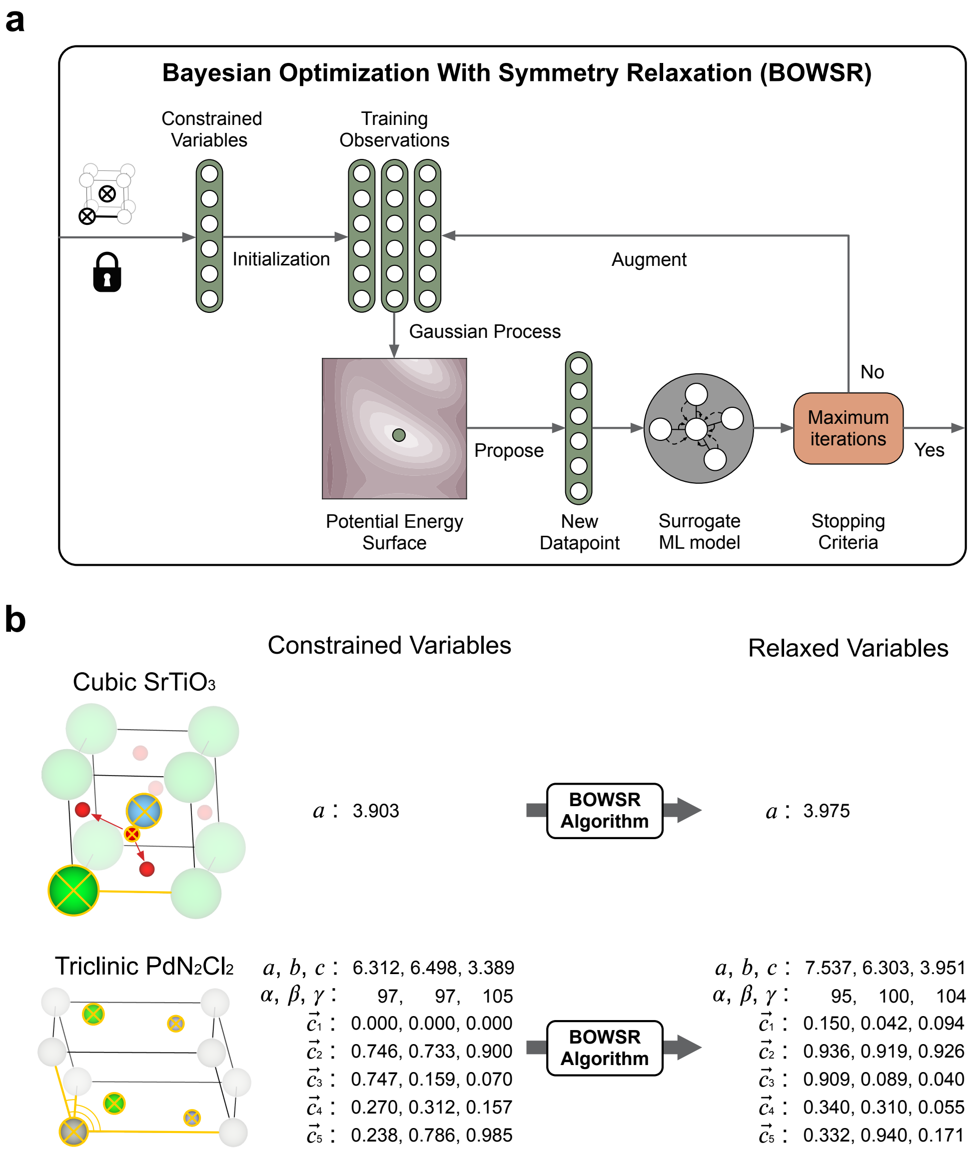

Figure 4.1: Bayesian Optimization With Symmetry Relaxation (BOWSR) algorithm. a, The BOWSR algorithm parameterizes each crystal based on the independent lattice parameters and atomic coordinates based on its space group. The potential energy surface is then approximated by initializing a set of training observations and energies from the ML energy model. Bayesian optimization is then used to iteratively propose lower energy geometries based on prior observations. b, Two examples of the geometry parameterization for cubic perovskite $SrTiO_3$ and triclinic PdN_2Cl_2. For the high-symmetry cubic perovskite, the lattice parameter a is the only independent parameter, and all atoms are in special Wyckoff positions with no degrees of freedom in the fractional coordinates. For the triclinic crystal, all six lattice parameters and all atomic coordinates are independent parameters.

The convergence accuracy and speed of BOWSR are set by the energy evaluator $U(.)$, which can be any computational model, including *ab initio* methods, empirical potentials, and surrogate ML models. In this work, we have elected to use a MatErials Graph Network (MEGNet) formation energy model previously trained on the DFT-computed formation energies of 133,420 Materials Project crystals.[57] This MEGNet model has a cross-validated mean absolute error (MAE) of 26 meV atom^{-1}, which is among the best accuracy among general ML models thus far.[70,71]. Examples of the convergence of the BOWSR algorithm using the MEGNet energy model are shown in Figure C.2.

4.3.2 Properties prediction

Elemental substitution is a common, chemically intuitive approach to deriving potential new compounds. For instance, the rock salt LiCl can be derived from rock salt NaCl by substituting Na for the chemically similar Li. Here, we demonstrate the potential for BOWSR to substantially enhance ML property predictions of the formation energies and elastic moduli (bulk and shear moduli) of substituted crystals. The dataset comprises a total of 12,277 and 1,672 unique crystals with pre-computed DFT formation energies and elastic moduli, respectively, from the Materials Project.[57] These crystals belong to 144 (35 binary, 91 ternary, and 18 quaternary) common structure prototypes in the Inorganic Crystal Structure Database (ICSD).[221,222] Each prototype comprises at least 30 compositions (statistical distribution shown in Figure C.3). For each crystal in the dataset (e.g., rock salt GeTe), another crystal with the same prototype but a different composition (e.g., rock salt NaCl) was selected at random and multi-element substitutions (Na$\rightarrow$Ge, Cl$\rightarrow$Te) were performed to arrive at an "unrelaxed" structure. The BOWSR algorithm was then applied to obtain a BOWSR-relaxed structure. The unrelaxed, BOWSR-relaxed, and the original DFT-relaxed structures were then used as inputs for property predictions using MEGNet models. These MEGNet models were trained on the DFT-computed formation energies and elastic moduli of 133,420 and 12,179 crystals, respectively, from the Materials Project.

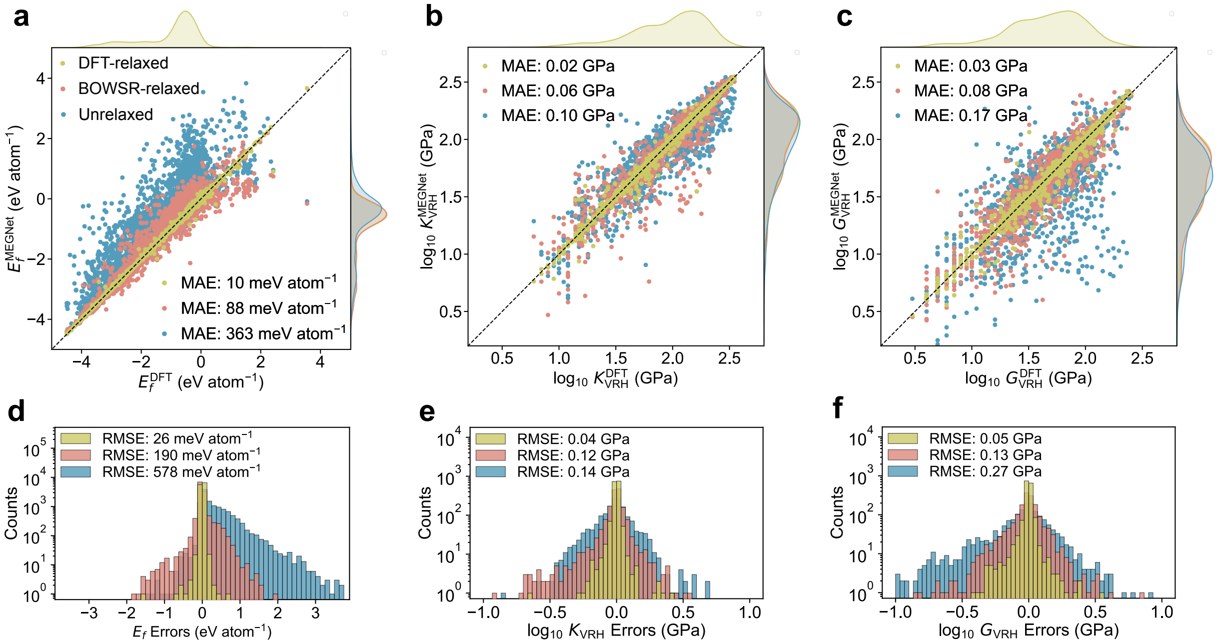

Figure 4.2: Performance of MEGNet materials properties predictions for three levels of relaxation. Three levels of relaxation are served as inputs for MEGNet materials properties predictions — unrelaxed, BOWSR-relaxed, and DFT-relaxed structures. a, b, and c show the parity plot of MEGNet prediction on formation energies, bulk moduli, and shear moduli, respectively. d, e, and f show the errors distribution on the corresponding materials property.

Figure 4.2 compares the MEGNet model predictions using the unrelaxed, BOWSR-relaxed, and DFT-relaxed structures as inputs with respect to DFT-computed values. The mean absolute errors (MAEs) of the MEGNet models using the DFT-relaxed structures provide a best-case performance baseline. It should be noted that the MEGNet models were trained using a superset of data from the Materials Project that includes the DFT-relaxed structures.[57] Hence, the reported MAEs of MEGNet predictions using DFT-relaxed structures in this work are much smaller than the previously reported MAEs of these MEGNet models from cross-validation and should not be considered as a metric for MEGNet performance. Using the unrelaxed structures as inputs results in much higher, positively skewed MAEs in the MEGNet formation energy prediction compared to using DFT-relaxed structures. This is because the unrelaxed structures have lattice parameters and atomic positions that can deviate substantially from the ground state DFT-relaxed structures, resulting in higher energies. Using the BOWSR-relaxed structures as inputs reduces the MAEs by a factor of four, from 363 meV atom^{-1} to 88 meV atom^{-1}. The R^2 also substantially increases from 0.67 to 0.96, and the error distribution is Gaussian-like with a mean close to 0. Similarly, large improvements in the MEGNet predictions of the elastic moduli are also observed using the BOWSR-relaxed structures compared to using unrelaxed structures, with MAEs in the $\log_{10} K_{\mathrm{VRH}}$ and $\log_{10} G_{\mathrm{VRH}}$ reducing by half. We tested the sensitivity of the BOWSR algorithm to the initial structures used to perform elemental substitution. Using four randomly chosen parent structures with different lattice parameters for each prototype, the above procedures were repeated and the results are shown in Figure C.4. The BOWSR-relaxed structures exhibit consistently low errors regardless of initial structure selection.

We also tested the sensitivity of the BOWSR algorithm to the accuracy of the energy evaluator by artificially introducing Gaussian noise into the MEGNet formation energy prediction. The energy errors from the BOWSR-relaxed structures are linearly correlated with the errors of the surrogate ML model with the root mean square error (RMSE) ranging from 27 to 1000 meV atom^{-1} (Figure C.5), which indicates the robustness of the BO propagation and the broad applicability of the BOWSR algorithm to any surrogate ML models. The same linear correlations are also observed between the elastic moduli errors and the errors of the surrogate ML model, as shown in Figure C.5c and d.

4.3.3 Discovery of ultra-incompressible hard materials

We used the BOWSR algorithm with the MEGNet models to rapidly screen hundreds of thousands of candidates for novel ultra-incompressible hard materials, as shown in Figure 4.3. Given that binary compounds have already been extensively explored in the literature[223,224], we targeted our search in 12 ternary $\mathrm{M}'_x\mathrm{M}''_y\mathrm{X}_z$ chemical spaces, where M$'$, M$''$ = Mo, W, Os, or Re and X = B or C. These elements were selected based on their common occurrences in ultra-incompressible hard binary compounds. By combinatorially applying elemental substitutions to 5,555 ternary structures prototypes in the ICSD,[221,222] 399,960 candidates were generated and relaxed using the BOWSR algorithm with the MEGNet energy model. The BOWSR-relaxed candidates were then screened for stability and mechanical properties using MEGNet property models. The stability metric used was the energy above hull $E_{\text{hull}}^{\text{MEGNet}}$, which was computed using the predicted formation energy $E_{\text{f}}^{\text{MEGNet}}$ with the 0 K phase diagram in the Materials Project database[52,57,60]. At this intermediate stage, a relatively generous threshold of $E_{\text{hull}}^{\text{MEGNet}} < 100$ meV atom^{-1} was used to obtain candidates that are likely to be thermodynamic stable.[61] Of these, candidates with relatively high MEGNet-predicted bulk and shear moduli ($K_{\text{VRH}}^{\text{MEGNet}} > 250$ GPa and $G_{\text{VRH}}^{\text{MEGNet}} > 100$ GPa) were identified. Similar to the stability criterion, the mechanical criteria used are slightly lower than the conventional threshold for ultra-incompressibility to account for the higher MAE of the MEGNet elastic moduli predictions.[224] DFT relaxations and energy calculations were then carried out on the 1,603 candidates that passed all three ML-based screening criteria. Subsequently, expensive DFT elastic tensor calculations[220] were performed on the 143 candidates that have DFT $E_{\text{hull}}^{\text{DFT}} < 100$ meV atom^{-1}.

Table 4.1 summarizes the computed elastic properties of the top ten candidates with the highest computed bulk modulus together with other well-known ultra-incompressible materials. Attempts were then made to synthesize all ten candidates with eight unique compositions via *in-situ* reactive spark plasma sintering (SPS) using elemental precursors in the appropriate ratios (see Methods). Two crystals, MoWC_2 ($P6_3/mmc$) and ReWB ($Pca2_1$), were successfully synthesized and confirmed via X-ray diffraction (XRD, Figure 4.4a) as single phase, while the synthesis of the other six compositions yielded multiple phases. Henceforth, we will refer to the two novel phases of MoWC_2 ($P6_3/mmc$) and ReWB ($Pca2_1$) simply as MoWC_2 and ReWB, respectively.

The mechanical properties of MoWC_2 and ReWB were measured using the pulse-echo method.[225,226] As shown in Figure 4.5a and b, the experimentally-measured bulk and shear moduli are in excellent agreement with both the MEGNet and DFT predictions. Both new materials exhibit ultra-incompressibility, with bulk modulus close to or larger than 300 GPa[224]. MoWC_2 also exhibits high estimated Vickers hardnesses H_v of 36.6 at 0.49 N indentation load and 20.9 GPa at 9.8 N load (Figure 4.5c). ReWB has a comparatively lower measured hardness of 29.5 at 0.49 N load and 17.6 GPa at 9.8 N load. The H_v values at 0.49 N load are within 20-25% of those derived from the MEGNet and DFT predicted shear moduli via the empirical relation $H_v = 0.151G$,[227] as shown in Figure 4.5d.

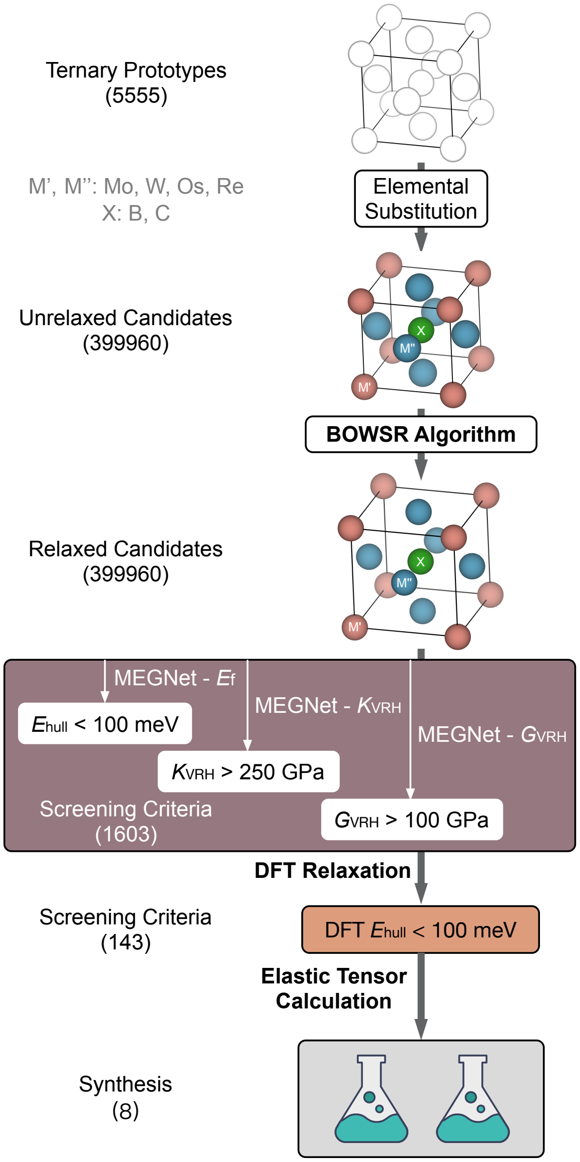

Figure 4.3: Flowchart of ultra-incompressible materials discovery leveraged by the BOWSR algorithm and MEGNet models. The materials candidates were generated by elemental substitution to structure prototypes. These candidates were relaxed by the BOWSR algorithm and subsequently screened by their predicted thermodynamic stability and mechanical properties. The screened candidates were further verified by DFT calculations, and the high-ranked candidates were directed to synthesis attempts. Quantity in the parenthesis shows the number of candidates at each stage.

Table 4.1: DFT-computed bulk modulus (K_{VRH}), shear modulus (G_{VRH}), Young's modulus (E_{VRH}), Poisson's ratio (ν) and energy above hull (E_{hull}) for the top 10 candidates with regard to K_{VRH} in descending order. $MoWC_2$ and ReWB are bolded as they are successfully synthesized by experiments. Some of the known ultra-incompressible materials are used as references.

	K_{VRH} (GPa)	G_{VRH} (GPa)	E_{VRH} (GPa)	ν	E_{hull} (meV)
Candidates					
ReOsB ($P\bar{6}m2$)	370.7	241.3	594.7	0.233	31.7
$ReOsB_2$ ($P6_3/mmc$)	367.3	220.9	552.0	0.250	87.8
$\mathbf{MoWC_2}$ ($\boldsymbol{P6_3/mmc}$)	**357.9**	**260.5**	**628.8**	**0.207**	**96.3**
ReWB ($Fddd$)	356.8	176.9	455.5	0.287	20.6
$Re_{13}WB_9$ ($P\bar{6}m2$)	353.1	177.0	455.1	0.285	88.4
ReWB ($\boldsymbol{Pca2_1}$)	**352.6**	**144.1**	**380.4**	**0.320**	**33.1**
OsWB ($Pbam$)	351.1	183.1	467.9	0.278	43.3
ReWB ($Cmce$)	350.9	161.5	420.1	0.301	32.6
$Re_6W_7B_8$ ($P6/m$)	348.4	182.8	466.8	0.277	22.2
ReW_2B_2 ($P4/mbm$)	345.8	156.0	406.8	0.304	72.1
Known incompressible materials					
C ($Fd\bar{3}m$)	430.3	503.6	1086.9	0.079	136.4
WC ($P\bar{6}m2$)	389.8	280.0	677.8	0.210	1.1
BN ($F\bar{4}3m$)	370.1	382.8	852.4	0.116	77.3
ReB_2 ($P6_3/mmc$)	334.9	272.3	642.7	0.180	4.7

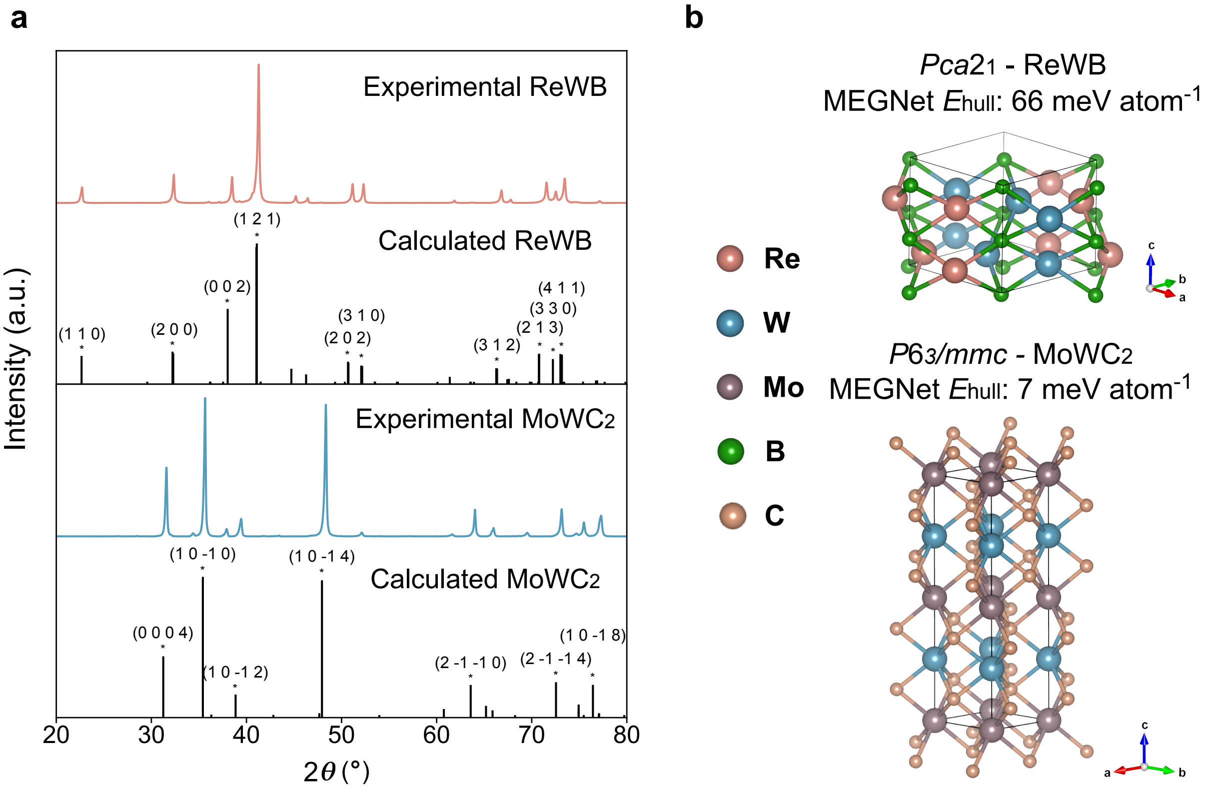

Figure 4.4: Two new materials proposed by the BOWSR algorithm and MEGNet prediction confirmed by XRD characterizations. a, Measured and calculated XRD patterns of two materials (ReWB and $MoWC_2$). The major peaks are indexed for reference. The pymatgen library [108] was used to calculate the XRD patterns of the DFT-relaxed crystal structures. Minor shifts in peak positions between the measured and calculated XRD patterns can be attributed to the systematic errors between DFT and experimentally-measured lattice parameters. b, Crystal structures and space group of these two materials. The predicted energy above hull for ReWB and $MoWC_2$ are 66 and 7 meV atom^{-1}, respectively.

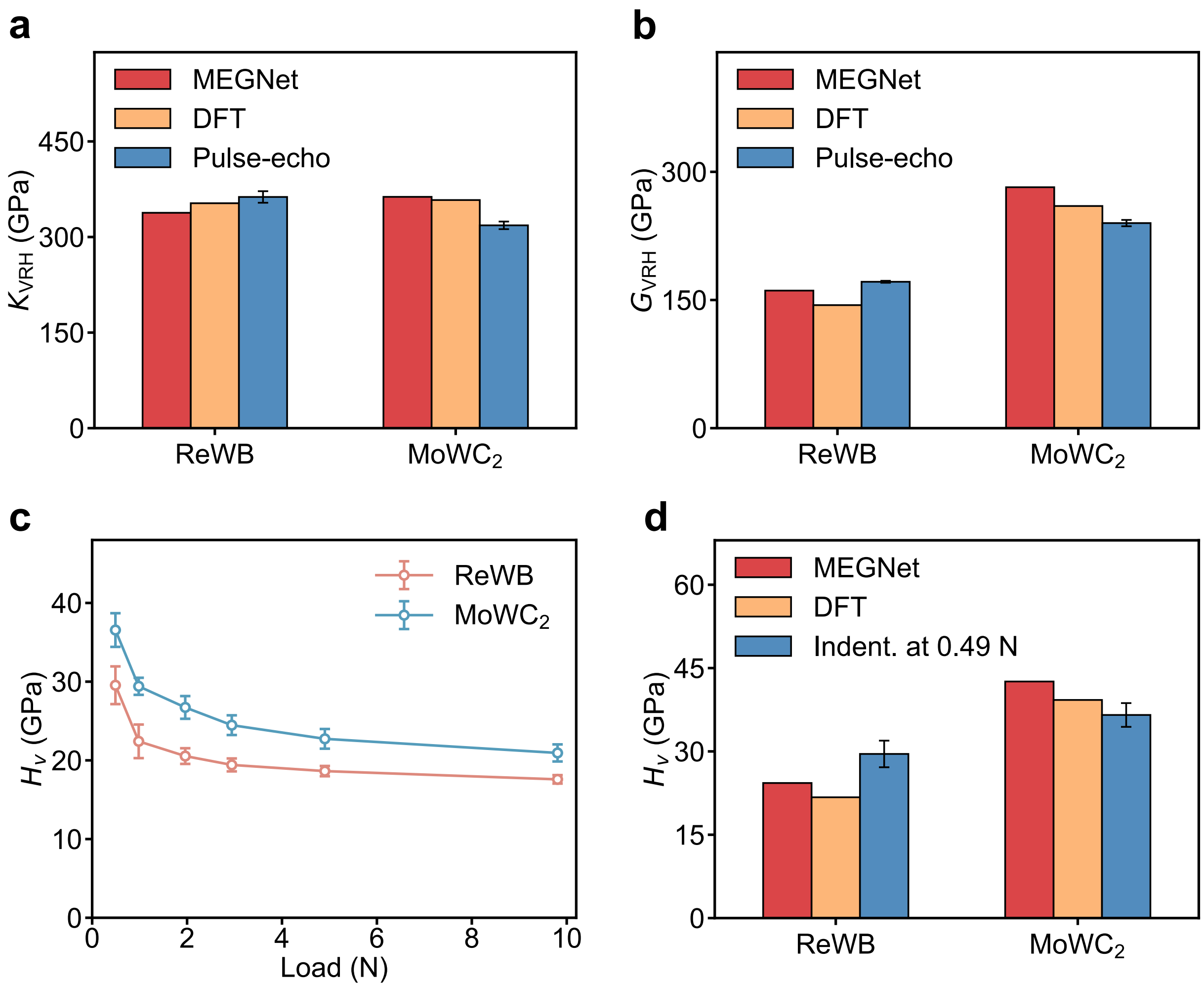

Figure 4.5: Experimental measurements and theoretical prediction of mechanical properties for the new materials. Comparisons of a, bulk moduli and b, shear moduli between MEGNet, DFT and pulse-echo measurements. c, Measured Vickers microhardness of ReWB and MoWC$_2$ under loads ranging from 0.49 N to 9.8 N. d, Comparisons between the hardness derived from MEGNet predicted bulk modulus and shear modulus[227] and the hardness measured by Vickers indentation at the low load (0.49 N). The DFT calculated results are referenced. The error bar represents the standard deviation of multiple experimental measurements.

4.4 Discussion

Many materials properties, such as formation energies, mechanical properties, etc., exhibit a strong dependence on the crystal structure. However, obtaining equilibrium crystal structures as inputs to accurate ML models still requires expensive *ab initio* computations. By coupling an accurate MEGNet energy model with Bayesian optimization of symmetry-constrained parameters, we demonstrate that the new algorithm can reasonably approximate equilibrium structures. The resulting substantial improvements in ML property predictions enable the rapid screening of ∼400,000 candidate crystals for stability and exceptional mechanical properties, 10^3 - 10^4 orders of magnitude larger than that accessible by high-throughput DFT calculations.

The effectiveness of the BOWSR algorithm is limited by the accuracy of the energy evaluator. While the MEGNet formation energy model has been selected in this work, we foresee that the future development of more accurate ML energy models may improve the quality of the BOWSR-relaxed structures, and subsequent ML property predictions, even further. Here, the search for ultra-incompressible materials has been chosen as a model problem due to the high cost of acquisition of elastic moduli via standard DFT approaches, but the approach outlined can be readily extended to any property for which a reliable ML model can be developed. It should be noted, however, that there is an inverse relationship between the cost of acquisition and the training data size; hence, datasets on expensive properties (e.g., elastic moduli, optical properties, etc.) tend to be much smaller in size compared to cheaper properties, making it more difficult to build reliable ML models for high-cost properties. While approaches such as transfer learning or multi-fidelity models have been shown to mitigate this trade-off to some extent,[72,206,228,229] the generally higher errors in ML models for high-cost properties should be factored into the screening process in the thresholds.

Chapter 4 presents an algorithmic effort in developing BOWSR for crystal structure relaxation, bypassing the high-cost DFT. We showcased that BOWSR algorithm and the MEGNet models enabled us to identify eight new candidates out of ∼400,000 transition metal borides and carbides for ultra-incompressible hard materials. Two of them were successfully synthesized via *in-situ* reactive spark plasma sintering (SPS).

Chapter 5

Summary and Outlook

Materials design remains one of the primary challenges in technological advancement. The optimization of the known materials and the discovery of the new materials are two key components. To approach these two major problems, ML is playing a transformative role because of the broad access of big materials data and the development of ML model frameworks. In this thesis, we highlight three works that assess the current ML models in large-scale atomistic simulations for materials optimization, and develop new ML algorithm for materials discovery.

In the first work, we perform a systematic unbiased evaluation of GAP, MTP, NNP, SNAP, and qSNAP ML-IAPs regarding three inextricably linked metrics — accuracy in materials property predictions, training data requirements, and computational cost. We show that an increase in the degree of freedom (DOF) and increase in training structures generally leads to higher accuracy for all ML-IAPs. By using the Pareto frontier to identify the trade-offs between accuracy and cost, we observe that there is an "optimal" configuration at which further expansion of the number of DOF yields little improvement in accuracy with increases in computational cost for each ML-IAPs. We also notice that even with relatively small training data sets of $\sim$100-200 structures, all ML-IAPs exhibit reasonably good accuracy, while further improvement can be achieved with larger training data sets for NNP and qSNAP due to their model complexity. We attribute this performance to the training data generation procedure intended to sample a diverse set of structures from multi-temperature AIMD and conclude that diversity of training data is arguably a more important consideration than quantity. These observations provide a critical guideline in choosing reasonable ML-IAPs for different applications of interest.

In the second work, we present an exemplified application of ML-IAP in studying the plastic deformation of RHEA system MoNbTaW using extensive MD simulations. We investigate the mobilities of screw and edge dislocations over various temperatures ranging from 300 K to 2000 K, and evaluate how these mobilities are affected by the presence of SRO. We notice that the movement of screw dislocations is driven by kink-pair nucleation and migration, while a cross-slip locking mechanism appears due to the intrinsic fluctuation of energy along the dislocation line and rugged energy landscape in the system. The SRO is found to induce a temperature-dependent strengthening effect on the screw dislocations moving through the kink-pair nucleation mechanism. This effect is further understood by a proposed phenomenological model, which shows that the SRO contributes to the free energy barrier for the kink-pair mechanism. These findings reveal the mechanism of influence of temperature and SRO on the plastic deformation of RHEAs, and serve as a useful guideline for optimizing the processing conditions for MoNbTaW as well as other high-entropy alloys.

In the third work, we propose the BOWSR algorithm to break through the limitations of graph-based models that require accurate crystal structures as inputs. Using the state-of-the-art MEGNet energy model with BO of symmetry-constrained parameters, we demonstrate that the BOWSR algorithm can reasonably approximate equilibrium structures originally obtained from the DFT relaxations. The ML property predictions for BOWSR-relaxed structures yield significantly lower errors compared to unrelaxed structures. The substantial improvements enable the rapid screening of $\sim$400,000 candidate crystals for stability and exceptional mechanical properties in ultra-incompressible hard materials discovery. Experimental attempts were made to synthesize the top 10 candidates with regard to the highest computed bulk modulus, and two novel crystals were successfully confirmed. The algorithm proposed removes one of the final major bottlenecks to ML-based exploration of hypothetical materials entirely.

To conclude, the works fulfilled not only advance the understanding of relative strengths and weaknesses of major ML-IAPs for materials optimization as well as the mechanism of plastic deformation in RHEAs where ML-IAP applies, but also provide new protocol in accelerating materials discovery. We hope that these works may serve as inspiration for future efforts in materials design as a whole. Meanwhile, we also notice that there remain some gaps, which are possible avenues for future work. In this thesis, we have chosen only focus on only ML-IAPs based on local environment descriptors, while coverage of alternative ML-IAPs that rely on global representations may provide more insights. A guideline for methodological development is also lacking, where descriptor-model combinations can yield further values. Despite the great performance of BOWSR algorithm exhibited in materials discovery, several factors that may limit its effectiveness are yet to explore in detail. For example, while the BO yields much higher errors by removing symmetry constraints (i.e., treating all crystals as having triclinic $P1$ symmetry), preservation of symmetry remains a relatively strong assumption that constrains the identification of larger structure space for discovery.

Appendix A

Supporting information: Performance and cost sssessment of machine learning interatomic potentials

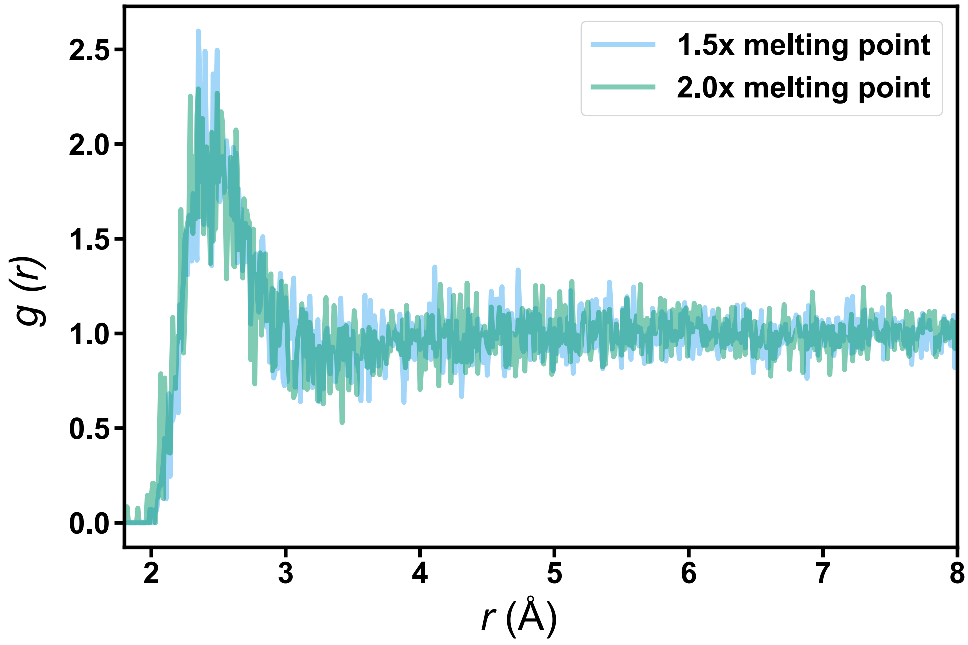

Figure A.1: The radial distribution function (RDF) of Si in high temperature (1.5×, 2.0× of the melting point) AIMD simulations.

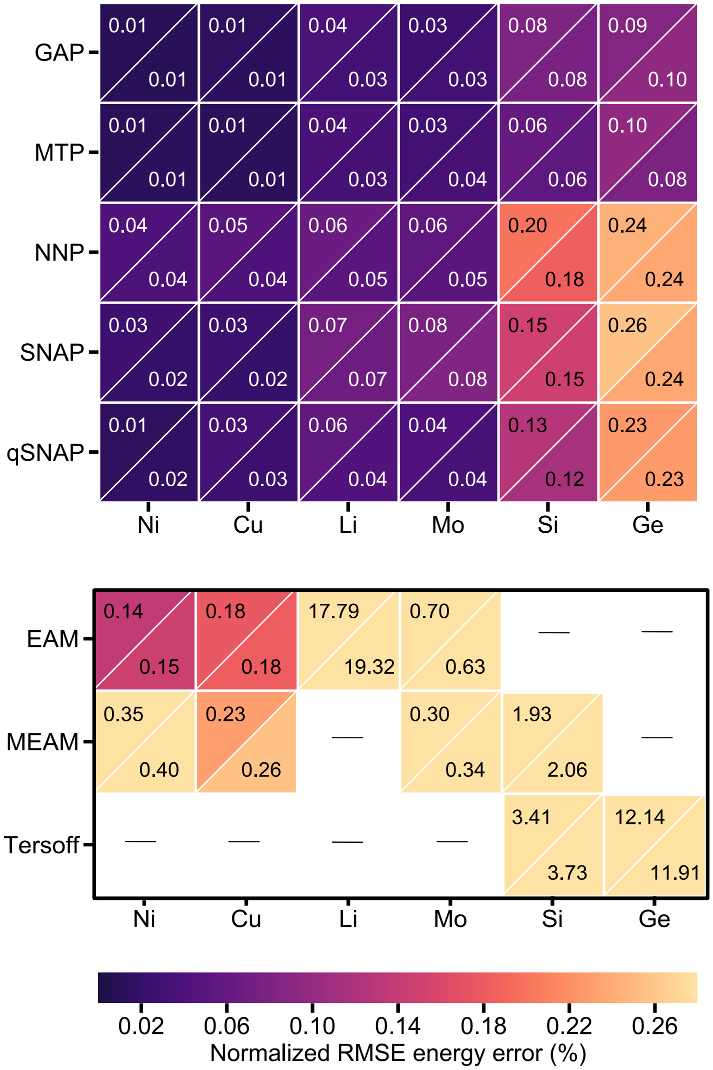

	Ni	Cu	Li	Mo	Si	Ge
GAP	0.01 0.01	0.01 0.01	0.04 0.03	0.03 0.03	0.08 0.08	0.09 0.10
MTP	0.01 0.01	0.01 0.01	0.04 0.03	0.03 0.04	0.06 0.06	0.10 0.08
NNP	0.04 0.04	0.05 0.04	0.06 0.05	0.06 0.05	0.20 0.18	0.24 0.24
SNAP	0.03 0.02	0.03 0.02	0.07 0.07	0.08 0.08	0.15 0.15	0.26 0.24
qSNAP	0.01 0.02	0.03 0.03	0.06 0.04	0.04 0.04	0.13 0.12	0.23 0.23

	Ni	Cu	Li	Mo	Si	Ge
EAM	0.14 0.15	0.18 0.18	17.79 19.32	0.70 0.63	—	—
MEAM	0.35 0.40	0.23 0.26	—	0.30 0.34	1.93 2.06	—
Tersoff	—	—	—	—	3.41 3.73	12.14 11.91

Figure A.2: Root-mean-square errors in predicted energies normalized to total energy per atom for all four ML-IAPs as well as traditional IAPs (EAM[121,122], MEAM[123–125], Tersoff[126,127]). The upper left and lower right triangles within each cell represent training and test errors, respectively.

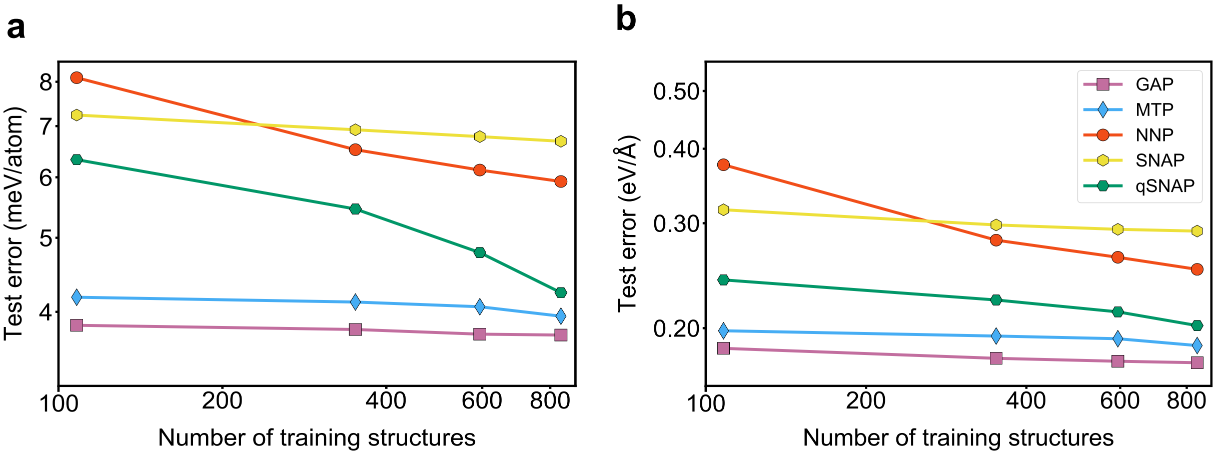

Figure A.3: Log-log plot of RMSEs in (a) energies (b) forces versus the the size of the training data for the ML-IAP Mo models. The slope of the line represents the learning rate of different ML-IAPs.

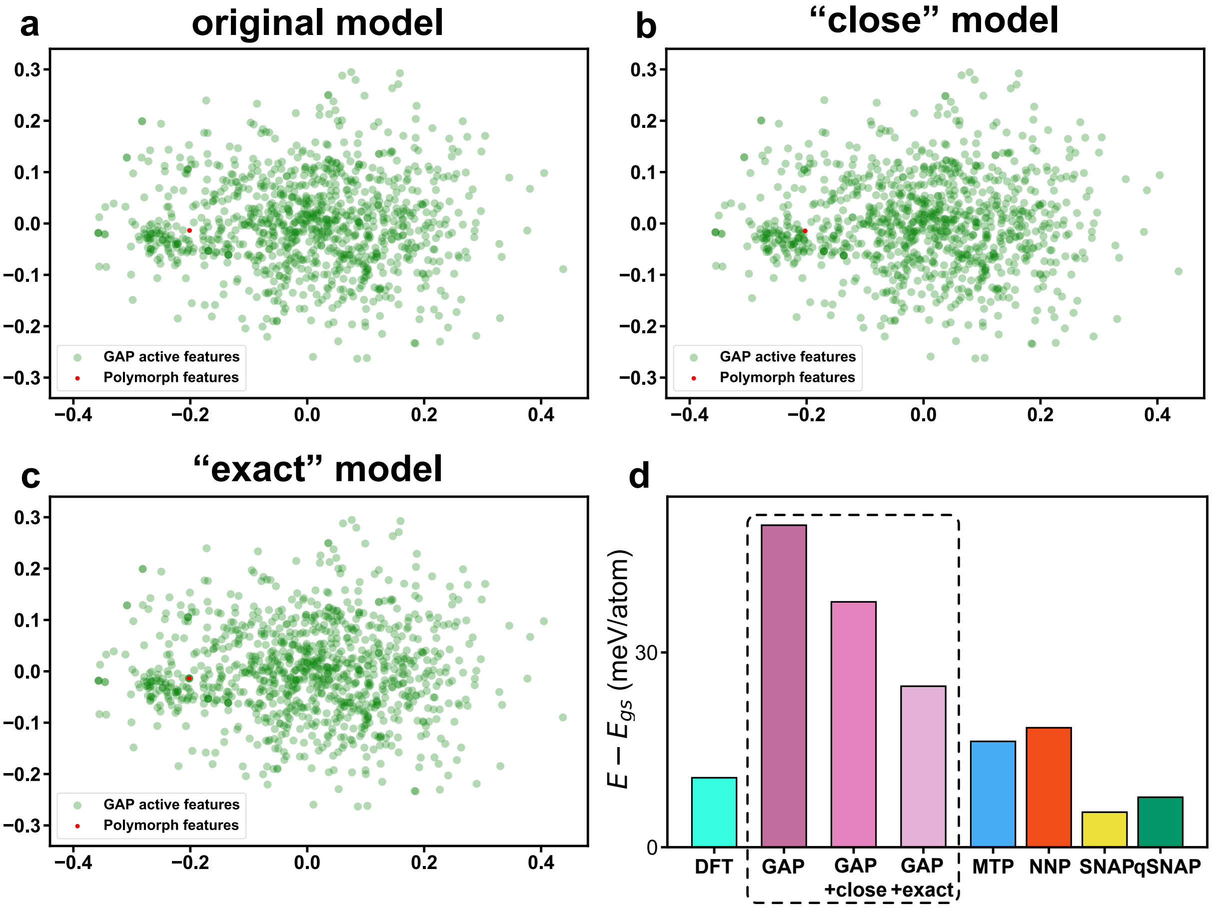

Figure A.4: Two-dimensional projection of the principal components of (a) the original model, (b) the “close” model and (c) the “exact” model. (d) Energetic differences between the wurtzite and diamond polymorph for Si of the original GAP model and augmented GAP models compared to DFT and other ML-IAPs.

Appendix B

Supporting information: Atomistic simulations of dislocation mobility in refractory high-entropy alloys and the effect of chemical short-range order

Table B.1: Basic materials property predictions of the MTP model. The predicted melting points (T_m), unstable stacking fault energy γ_{us} of (011) γ surface along the $[\bar{1}\bar{1}1]$ direction, elastic constants (c_{ij}), and Voigt-Reuss-Hill[129] bulk modulus (B_VRH) for bcc Nb, Mo, Ta, and W are compared with DFT and experimental values.

	T_m (K)	γ_{us} (mJ/m^2)	c_{11} (GPa)	c_{12} (GPa)	c_{44} (GPa)	B_VRH (GPa)
Nb						
Expt.[230]	2750	—	247	135	29	172
DFT	—	827	249	135	19	173
MTP	2700	789 (−4.6%)	238 (−4.4%)	159 (17.8%)	24 (26.3%)	185 (6.9%)
Mo						
Expt.[231]	2896	—	479	165	108	270
DFT	—	1468	472	158	106	263
MTP	2860	1256 (−14.4%)	390 (−17.4%)	174 (10.1%)	85 (−19.8%)	246 (−6.5%)
Ta						
Expt.[232]	3290	—	266	158	87	194
DFT	—	835	264	161	74	195
MTP	3040	809 (−3.1%)	257 (−2.7%)	161 (0.0%)	67 (−9.5%)	193 (−1.0%)
W						
Expt.[232]	3695	—	533	205	163	314
DFT	—	1661	511	200	142	304
MTP	3680	1557 (−6.3%)	480 (−6.1%)	187 (−6.5%)	122 (−14.1%)	285 (−6.3%)

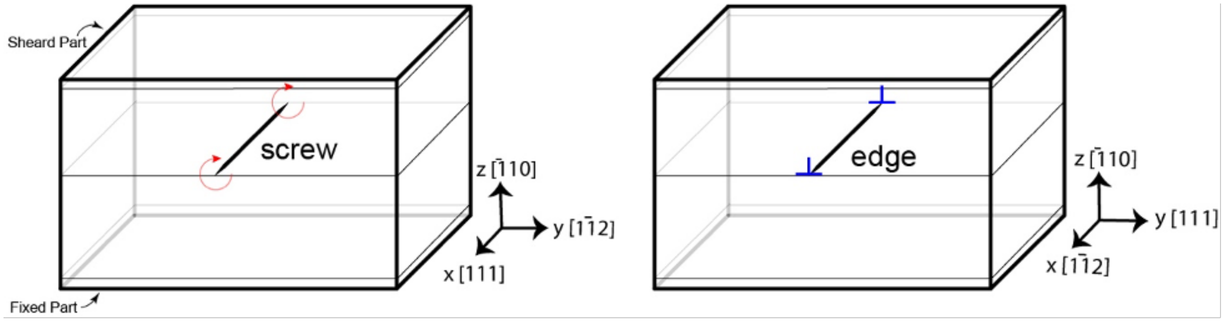

Figure B.1: MD Simulation cell for dislocation mobility simulations. Crystalline orientations of the cells are shown, with the screw and edge dislocations gliding on the $(1\bar{1}0)$ plane.

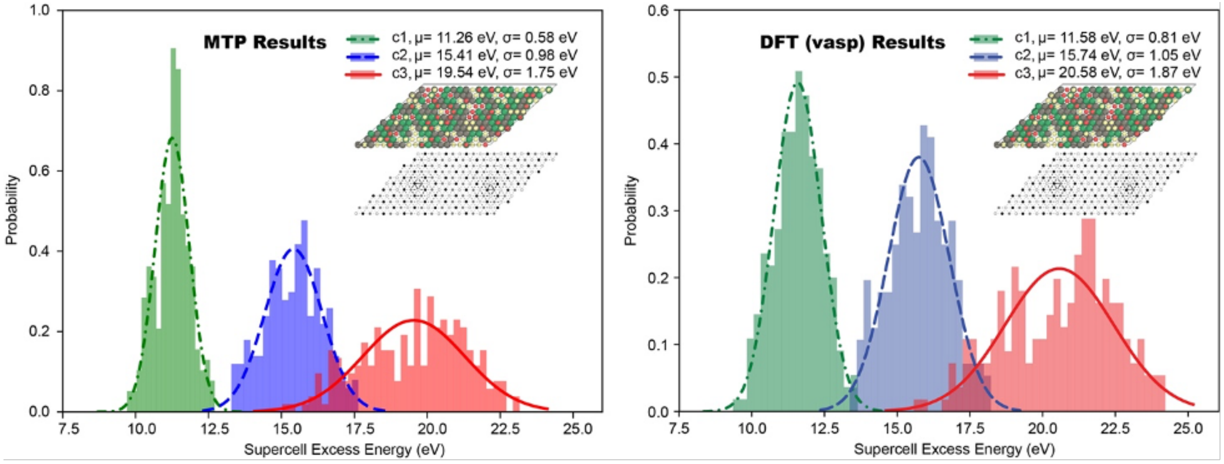

Figure B.2: Comparison of dislocation dipole energies calculated from MTP and DFT. Distributions of dislocation dipole energies for varying local environments, calculated through the MTP potential and compared with DFT data. The results were obtained by inserting a dislocation dipole to supercells with three different levels of randomness: c1, c2 and c3. Each configuration contains 231 different individual samples. For the DFT results the positions of the atoms are relaxed through DFT. For the MTP results these positions are relaxed in MD based on the MTP forces using the DFT relaxed cells. The histogram of supercell excess energies of different configuration calculated by MD and DFT are plotted in green, blue and red, and fitted with a Gaussian distribution, where μ is the average value and σ is the standard deviation. The results calculated by MTP agree well with the DFT results. (The supercell excess energy is defined as the energy difference between the supercell with and without the dislocation dipole. The detailed dipole cell construction and VASP parameters for the DFT calculations are described in previous work[162]).

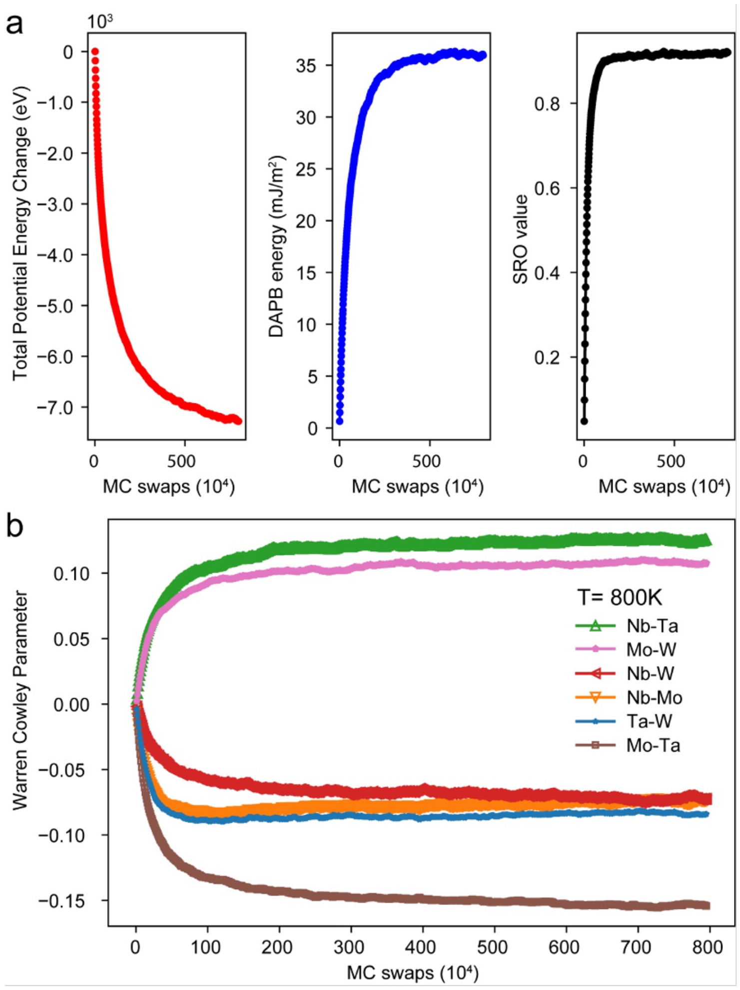

Figure B.3: Evolution of potential energy, diffuse antiphase boundary (DAPB) energy and local chemical SRO in the MoNbTaW RHEA from hybrid MC/MD simulations. a, Change in the total potential energy of the simulation cell containing 0.5 million atoms, DAPB energy and cumulative SRO parameter (see Methods section) as a function of the number of MC swaps during equilibration at 800K. b, The detailed values of Warren Cowley parameter α_{ij} for different pair types as a function of the MC swaps at the same temperature.

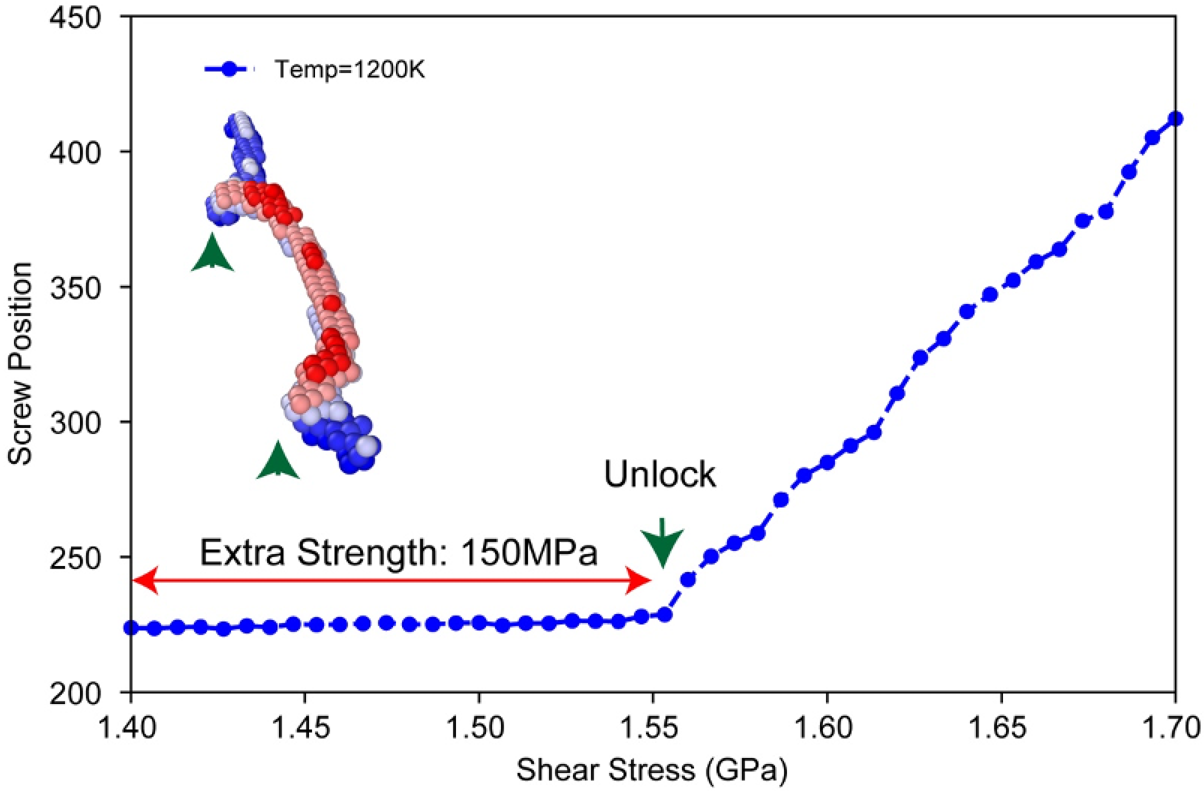

Figure B.4: Extra stress required to break the interlocking kinks. Restart from the final configuration shown in Figure 3.3c, the applied shear stress is increasing at the rate of 1.2 MPa/ps. The screw dislocation stays immobile until the shear stress reaches approximately 1.55 GPa, and the interlocking kinks are unlocked, as shown by the green arrow.

Appendix C

Supporting information: Accelerating materials discovery with bayesian optimization and graph deep learning

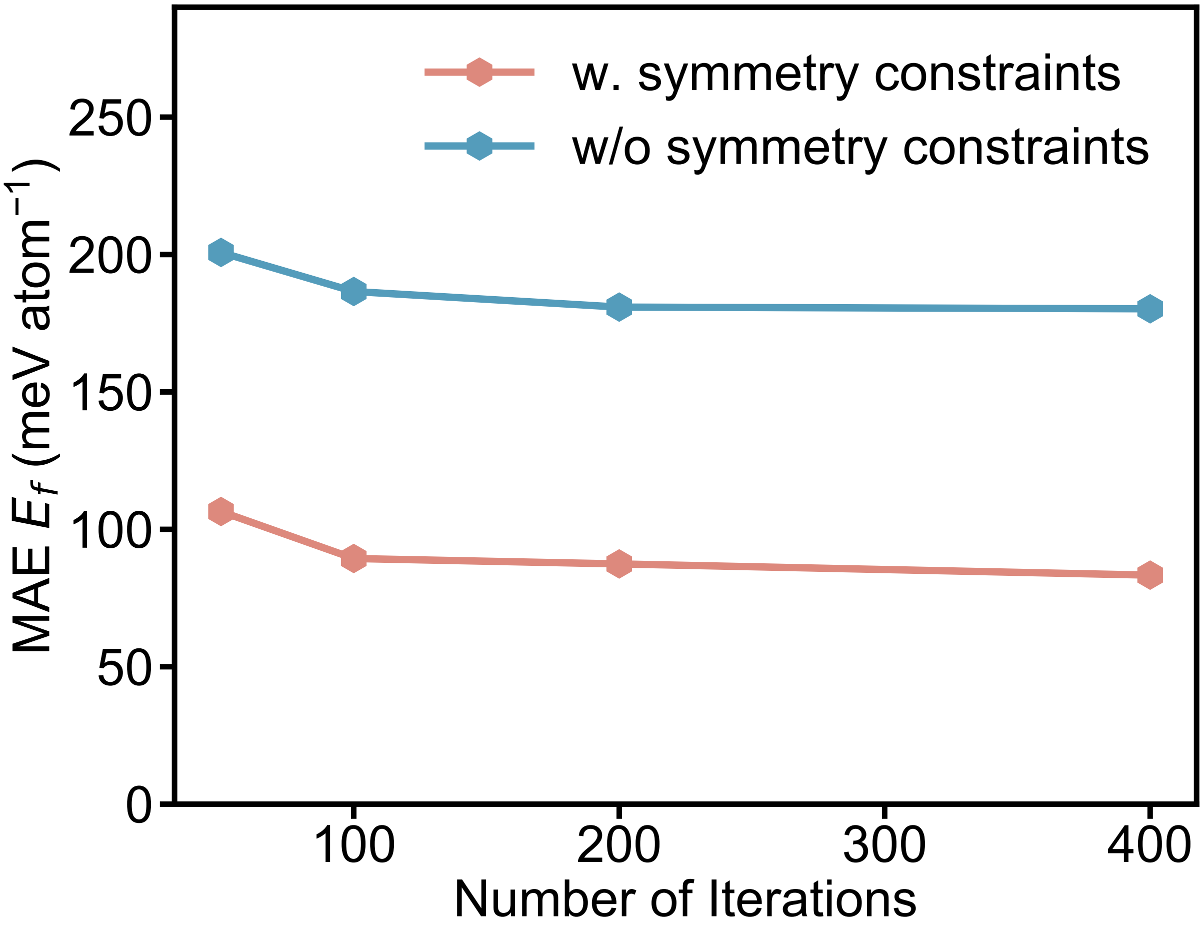

Figure C.1: Comparison of mean absolute errors (MAEs) of MEGNet predictions compared to DFT in formation energies of crystals relaxed using Bayesian optimization with and without symmetry constraints. The MAEs are plotted with respect to the number of iterations.

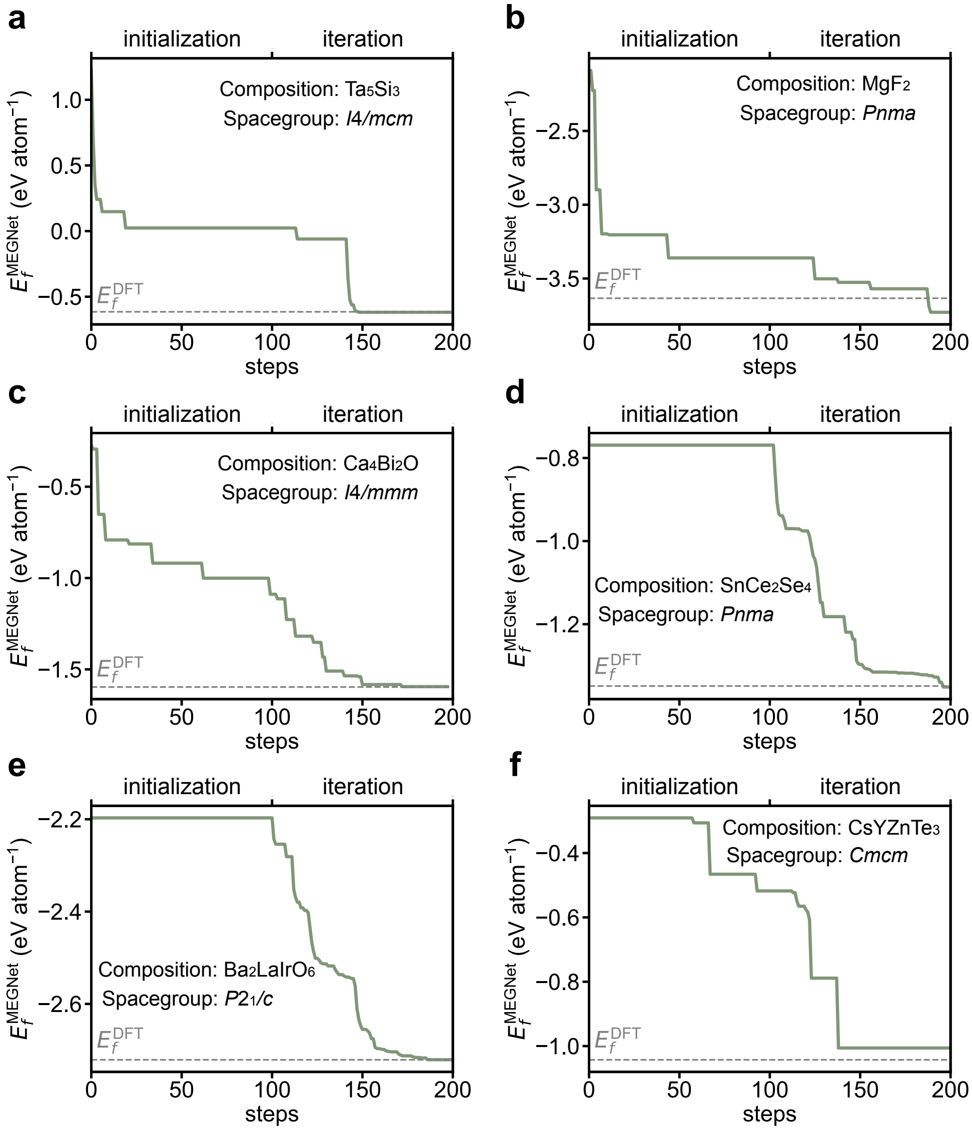

Figure C.2: Convergence of the BOWSR algorithm using the MEGNet energy model for six structures in the dataset of properties prediction. These structures comprise two binary, two ternary, and two quaternary crystals obtained from elemental substitution in commonly occurring structure prototypes. The structure prototypes for **a,** Ta_5Si_3, **b,** MgF_2, **c,** Ca_4Bi_2O, **d,** $SnCe_2Se_4$, **e,** Ba_2LaIrO_6, **f,** $CsYZnTe_3$ are Cr_5B_3 (ICSD# 27124), Sr_2Si (ICSD# 422), K_2NiF_4 (ICSD# 15576), $CaFe_2O_4$ (ICSD# 28177), La_2ZnIrO_6 (ICSD# 75596), and $KZrCuS_3$ (ICSD# 80624), respectively. All structures were relaxed via the BOWSR algorithm using the default number of initialization samples (100) and iterations (100).

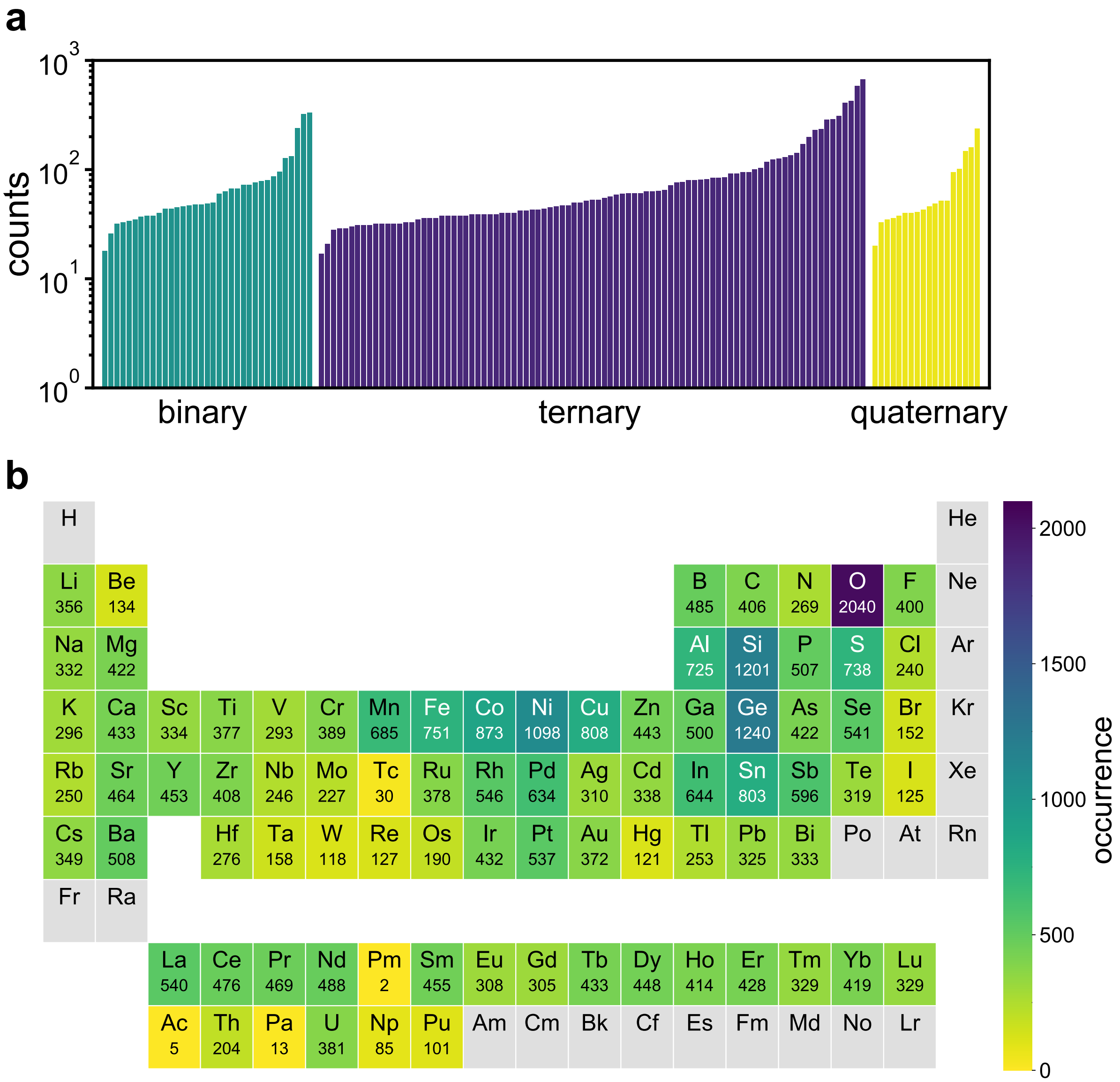

Figure C.3: Statistical distribution of dataset used for property predictions. a, The distribution of 35 binary, 91 ternary, and 18 quaternary commonly occurring structure prototypes in the dataset. Each bar represents one structure prototype and there are at least 30 unique compositions for each structure prototype. b, Frequency of each element occurring in the dataset. Elements are color-coded according to the number of occurrences. Oxygen is the most common element. The relatively high frequencies of the transition metal elements Fe, Co, Ni, Cu can be attributed to the commonly occurring intermetallic structure prototypes. The three most commonly occurring structure prototypes are the ternary intermetallic ($ThCr_2Si_2$,[233] TiNiSi,[234] and ZrNiAl[235]) and have 633, 619, and 484 compositions, respectively.

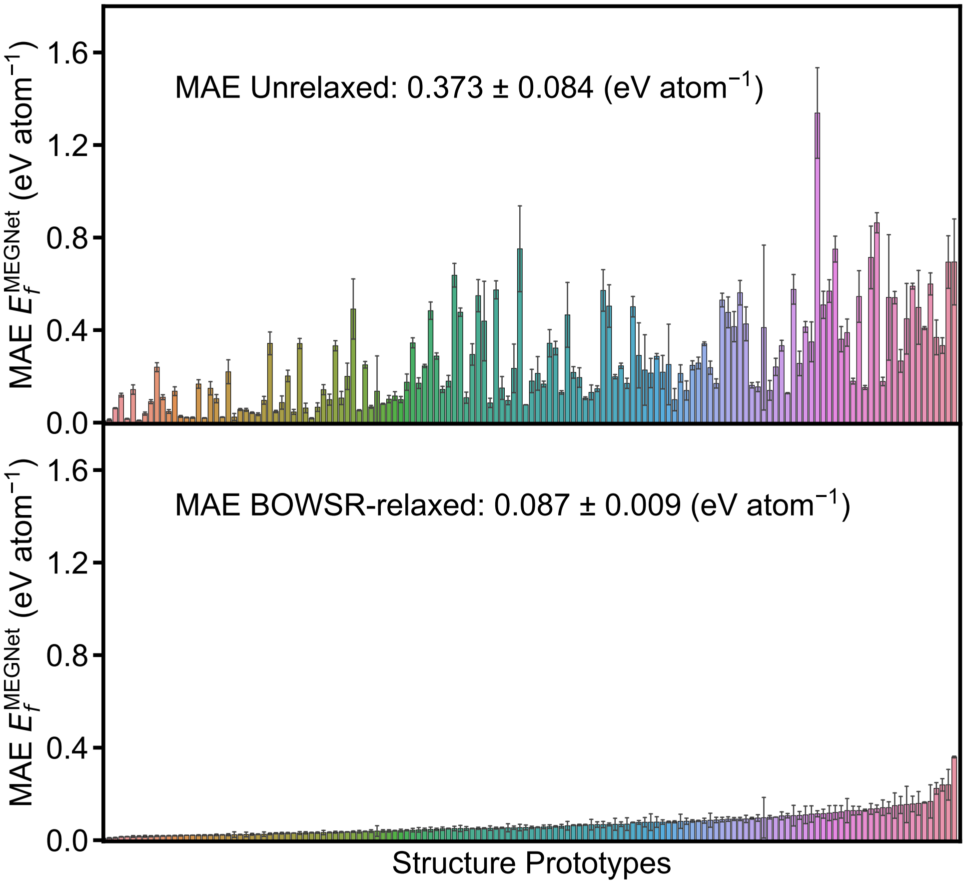

Figure C.4: Mean absolute errors (MAEs) of MEGNet prediction compared to DFT ground state calculations in formation energies using unrelaxed and BOWSR-relaxed structures grouped by structure prototypes. To test the sensitivity of the BOWSR algorithm to the initial structures, within each structure prototype, we selected four parent structures with different lattice parameters for elemental substitution to obtain the unrelaxed structures (i.e., same composition with different lattice parameters). The mean and standard deviation in the MAEs of the MEGNet formation energy prediction with respect to DFT-computed values for each prototype are plotted in the ascending order of mean MAE for the BOWSR-relaxed structures. While the unrelaxed structures obtained from elemental substitution have large MAEs, relaxation via the BOWSR algorithm consistently yields structures with much lower and less noisy MAEs in the formation energies.

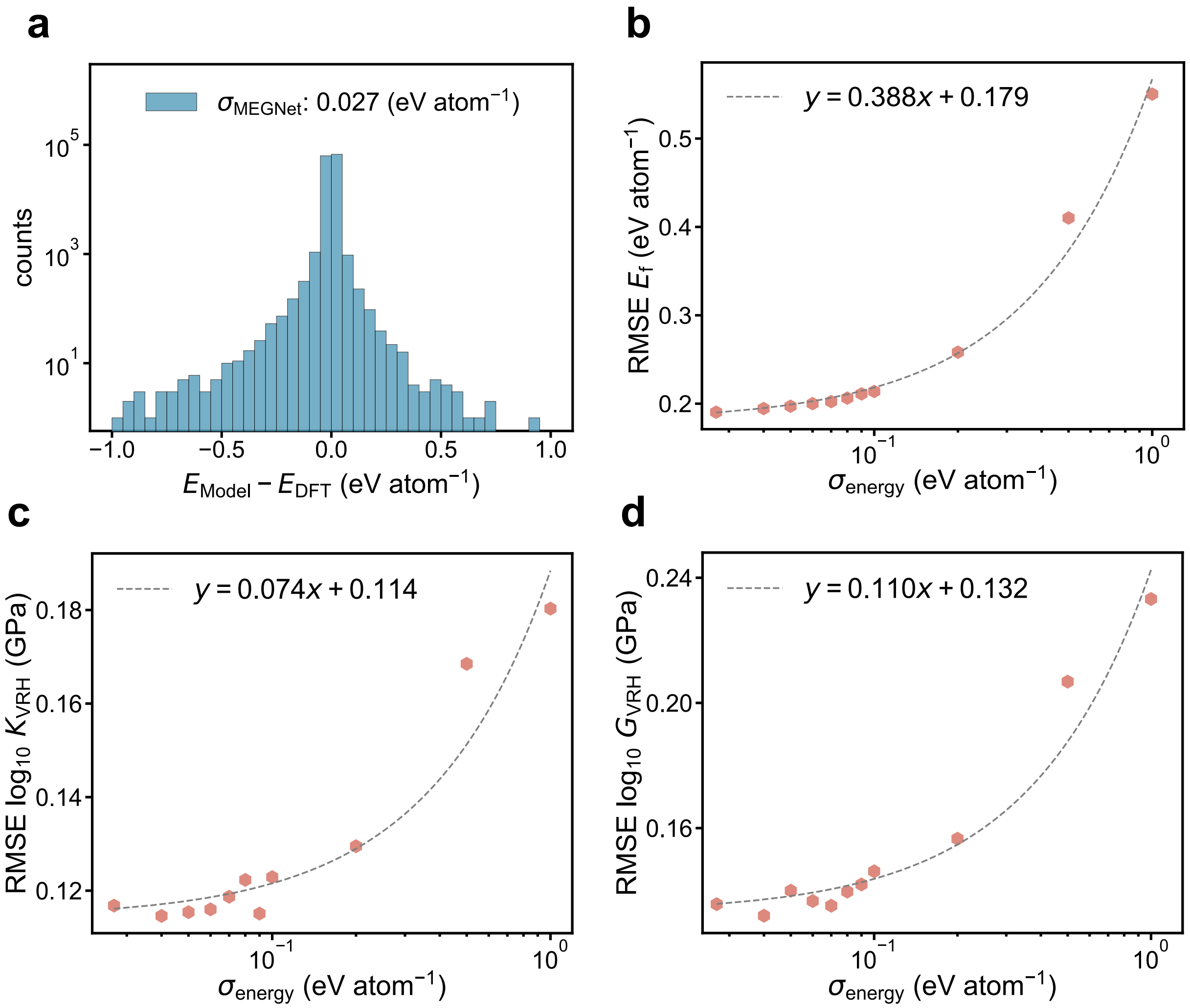

Figure C.5: Sensitivity of the BOWSR algorithm to the accuracy of the energy model. a, Error distributions of the MEGNet formation energy model on the training and test data. Both the standard deviation (σ) and root mean squre error (RMSE) are 27 meV atom^{-1}. Varying amounts of Gaussian noise are added to the MEGNet formation energy prediction during the BOWSR relaxation process. The error of the energy model σ_{energy} is then given by $\sqrt{\sigma^2_{\mathrm{MEGNet}} + \sigma^2_{\mathrm{noise}}}$, where σ_{noise} is the standard deviation of the added noise. The RMSEs of the MEGNet-predicted b, formation energy, c, bulk modulus, and d, shear modulus for the BOWSR-relaxed structures are plotted against the error in the energy model. In all cases, linear correlations are observed between the RMSE of the MEGNet prediction and the error of the energy model, and reasonably low RMSEs in prediction are obtained when $\sigma_{\mathrm{energy}} < 0.1$ eV atom^{-1}.

Bibliography

[1] P. Hohenberg and W. Kohn. Inhomogeneous electron gas. *Phys. Rev.*, 136(3B):B864, 1964. doi: 10.1103/physrev.136.b864.

[2] W. Kohn and L. J. Sham. Self-Consistent Equations Including Exchange and Correlation Effects. *Phys. Rev.*, 140(4A):A1133–A1138, November 1965. ISSN 0031-899X. doi: 10.1103/PhysRev.140.A1133.

[3] I. Y. Zhang, X. Xu, Y. Jung, and W. A. Goddard. A fast doubly hybrid density functional method close to chemical accuracy using a local opposite spin ansatz. *Proc. Natl. Acad. Sci.*, 108(50):19896–19900, December 2011. ISSN 0027-8424, 1091-6490. doi: 10.1073/pnas.1115123108.

[4] Y. Zhang, X. Xu, and W. A. Goddard. Doubly hybrid density functional for accurate descriptions of nonbond interactions, thermochemistry, and thermochemical kinetics. *Proc. Natl. Acad. Sci.*, 106(13):4963–4968, March 2009. ISSN 0027-8424, 1091-6490. doi: 10.1073/pnas.0901093106.

[5] Hyunjun Ji, Yihan Shao, William A. Goddard, and Yousung Jung. Analytic Derivatives of Quartic-Scaling Doubly Hybrid XYGJ-OS Functional: Theory, Implementation, and Benchmark Comparison with M06-2X and MP2 Geometries for Nonbonded Complexes. *J. Chem. Theory Comput.*, 9(4):1971–1976, April 2013. ISSN 1549-9618, 1549-9626. doi: 10.1021/ct400050d.

[6] Francesco Maresca and William A. Curtin. Theory of screw dislocation strengthening in random BCC alloys from dilute to "High-Entropy" alloys. *Acta Materialia*, 182:144–162, January 2020. ISSN 13596454. doi: 10.1016/j.actamat.2019.10.007.

[7] Xiang-Guo Li, Chi Chen, Hui Zheng, Yunxing Zuo, and Shyue Ping Ong. Complex strengthening mechanisms in the NbMoTaW multi-principal element alloy. *npj Comput Mater*, 6(1):70, December 2020. ISSN 2057-3960. doi: 10.1038/s41524-020-0339-0.

[8] Erik A Wu, Swastika Banerjee, Hanmei Tang, Peter M Richardson, Jean-Marie Doux, Ji Qi, Zhuoying Zhu, Antonin Grenier, Yixuan Li, Enyue Zhao, et al. A stable cathode-solid electrolyte composite for high-voltage, long-cycle-life solid-state sodium-ion batteries. *Nature communications*, 12(1):1–11, 2021. doi: 10.1038/s41467-021-21488-7.

[9] Daniel W. Davies, Keith T. Butler, Adam J. Jackson, Andrew Morris, Jarvist M. Frost, Jonathan M. Skelton, and Aron Walsh. Computational Screening of All Stoichiometric Inorganic Materials. *Chem*, 1(4):617–627, October 2016. ISSN 24519294. doi: 10.1016/j.chempr.2016.09.010.

[10] Geoffroy Hautier. Finding the needle in the haystack: Materials discovery and design through computational ab initio high-throughput screening. *Computational Materials Science*, 163:108–116, June 2019. ISSN 09270256. doi: 10.1016/j.commatsci.2019.02.040.

[11] Keith T. Butler, Daniel W. Davies, Hugh Cartwright, Olexandr Isayev, and Aron Walsh. Machine learning for molecular and materials science. *Nature*, 559(7715):547–555, July 2018. ISSN 0028-0836, 1476-4687. doi: 10.1038/s41586-018-0337-2.

[12] Chi Chen, Yunxing Zuo, Weike Ye, Xiangguo Li, Zhi Deng, and Shyue Ping Ong. A Critical Review of Machine Learning of Energy Materials. *Adv. Energy Mater.*, 10(8): 1903242, February 2020. ISSN 1614-6832, 1614-6840. doi: 10.1002/aenm.201903242.

[13] J.-W. Yeh, S.-K. Chen, S.-J. Lin, J.-Y. Gan, T.-S. Chin, T.-T. Shun, C.-H. Tsau, and S.-Y. Chang. Nanostructured High-Entropy Alloys with Multiple Principal Elements: Novel Alloy Design Concepts and Outcomes. *Adv. Eng. Mater.*, 6(5):299–303, May 2004. ISSN 1438-1656, 1527-2648. doi: 10.1002/adem.200300567.

[14] Jian-Hao Chen, Chaun Jang, Shudong Xiao, Masa Ishigami, and Michael S Fuhrer. Intrinsic and extrinsic performance limits of graphene devices on sio2. *Nature nanotechnology*, 3 (4):206–209, 2008. doi: 10.1038/nnano.2008.58.

[15] Zhong-Shuai Wu, Wencai Ren, Li Xu, Feng Li, and Hui-Ming Cheng. Doped graphene sheets as anode materials with superhigh rate and large capacity for lithium ion batteries. *ACS nano*, 5(7):5463–5471, 2011. doi: 10.1021/nn2006249.

[16] Rebecca L Milot, Giles E Eperon, Henry J Snaith, Michael B Johnston, and Laura M Herz. Temperature-dependent charge-carrier dynamics in ch3nh3pbi3 perovskite thin films. *Advanced Functional Materials*, 25(39):6218–6227, 2015. doi: 10.1002/adfm.201502340.

[17] Steve Plimpton. Fast Parallel Algorithms for Short-Range Molecular Dynamics. *J. Comput. Phys.*, 117:1 – 19, 1995. ISSN 0021-9991. doi: https://doi.org/10.1006/jcph.1995.1039.

[18] A. K. Rappe, C. J. Casewit, K. S. Colwell, W. A. Goddard, and W. M. Skiff. UFF, a full periodic table force field for molecular mechanics and molecular dynamics simulations. *J. Am. Chem. Soc.*, 114(25):10024–10035, December 1992. ISSN 0002-7863. doi: 10.1021/ja00051a040.

[19] Stephen L. Mayo, Barry D. Olafson, and William A. Goddard. DREIDING: A generic force field for molecular simulations. *J. Phys. Chem.*, 94(26):8897–8909, December 1990. ISSN 0022-3654, 1541-5740. doi: 10.1021/j100389a010.

[20] Adri C. T. Van Duin, Siddharth Dasgupta, Francois Lorant, and William A. Goddard. ReaxFF: A Reactive Force Field for Hydrocarbons. *J. Phys. Chem. A*, 105(41):9396–9409, October 2001. ISSN 1089-5639, 1520-5215. doi: 10.1021/jp004368u.

[21] Murray S Daw and Michael I Baskes. Embedded-atom method: Derivation and application to impurities, surfaces, and other defects in metals. *Physical Review B*, 29(12):6443, 1984. doi: 10.1103/PhysRevB.29.6443.

[22] Michael I Baskes. Modified embedded-atom potentials for cubic materials and impurities. *Physical review B*, 46(5):2727, 1992. doi: 10.1103/PhysRevB.46.2727.

[23] Chi Chen, Zhi Deng, Richard Tran, Hanmei Tang, Iek-Heng Chu, and Shyue Ping Ong. Accurate force field for molybdenum by machine learning large materials data. *Phys. Rev. Materials*, 1(4):043603, September 2017. ISSN 2475-9953. doi: 10.1103/PhysRevMaterials.1.043603.

[24] Albert P Bartók, Sandip De, Carl Poelking, Noam Bernstein, James R Kermode, Gábor Csányi, and Michele Ceriotti. Machine learning unifies the modeling of materials and molecules. *Science advances*, 3(12):e1701816, 2017. doi: 10.1126/sciadv.1701816.

[25] Yunxing Zuo, Chi Chen, Xiangguo Li, Zhi Deng, Yiming Chen, Jörg Behler, Gábor Csányi, Alexander V. Shapeev, Aidan P. Thompson, Mitchell A. Wood, and Shyue Ping Ong. Performance and Cost Assessment of Machine Learning Interatomic Potentials. *J. Phys. Chem. A*, 124(4):731–745, January 2020. ISSN 1089-5639, 1520-5215. doi: 10.1021/acs.jpca.9b08723.

[26] Jörg Behler. Atom-centered symmetry functions for constructing high-dimensional neural network potentials. *J. Chem. Phys.*, 134(7):074106, February 2011. ISSN 0021-9606, 1089-7690. doi: 10.1063/1.3553717.

[27] Albert P. Bartók, Mike C. Payne, Risi Kondor, and Gábor Csányi. Gaussian Approximation Potentials: The Accuracy of Quantum Mechanics, without the Electrons. *Phys. Rev. Lett.*, 104(13):136403, April 2010. ISSN 0031-9007, 1079-7114. doi: 10.1103/PhysRevLett.104.136403.

[28] Albert P. Bartók, Risi Kondor, and Gábor Csányi. On representing chemical environments. *Phys. Rev. B*, 87(18):184115, May 2013. ISSN 1098-0121, 1550-235X. doi: 10.1103/PhysRevB.87.184115.

[29] Alexander V. Shapeev. Moment Tensor Potentials: A Class of Systematically Improvable Interatomic Potentials. *Multiscale Model. Simul.*, 14(3):1153–1173, January 2016. ISSN 1540-3459, 1540-3467. doi: 10.1137/15M1054183.

[30] A.P. Thompson, L.P. Swiler, C.R. Trott, S.M. Foiles, and G.J. Tucker. Spectral neighbor analysis method for automated generation of quantum-accurate interatomic potentials. *J. Comput. Phys.*, page 15, 2015. doi: 10.1016/j.jcp.2014.12.018.

[31] V. Botu and R. Ramprasad. Learning scheme to predict atomic forces and accelerate materials simulations. *Phys. Rev. B*, 92(9):094306, September 2015. ISSN 1098-0121, 1550-235X. doi: 10.1103/PhysRevB.92.094306.

[32] Jörg Behler. Perspective: Machine learning potentials for atomistic simulations. *J. Chem. Phys.*, 145(17):170901, 2016. doi: 10.1063/1.4966192.

[33] Volker L. Deringer and Gábor Csányi. Machine learning based interatomic potential for amorphous carbon. *Phys. Rev. B*, 95(9):094203, March 2017. ISSN 2469-9950, 2469-9969. doi: 10.1103/PhysRevB.95.094203.

[34] Albert P. Bartók, James Kermode, Noam Bernstein, and Gábor Csányi. Machine Learning a General-Purpose Interatomic Potential for Silicon. *Phys. Rev. X*, 8(4):041048, December 2018. ISSN 2160-3308. doi: 10.1103/PhysRevX.8.041048.

[35] Nongnuch Artrith, Björn Hiller, and Jörg Behler. Neural network potentials for metals and oxides–first applications to copper clusters at zinc oxide. *physica status solidi (b)*, 250(6): 1191–1203, 2013. doi: 10.1002/pssb.201248370.

[36] Jörg Behler and Michele Parrinello. Generalized Neural-Network Representation of High-Dimensional Potential-Energy Surfaces. *Phys. Rev. Lett.*, 98(14):146401, April 2007. ISSN 0031-9007, 1079-7114. doi: 10.1103/PhysRevLett.98.146401.

[37] Jörg Behler. Neural network potential-energy surfaces in chemistry: A tool for large-scale simulations. *Phys. Chem. Chem. Phys.*, 13(40):17930, 2011. ISSN 1463-9076, 1463-9084. doi: 10.1039/c1cp21668f.

[38] Wojciech J. Szlachta, Albert P. Bartók, and Gábor Csányi. Accuracy and transferability of Gaussian approximation potential models for tungsten. *Phys. Rev. B*, 90(10):104108, September 2014. ISSN 1098-0121, 1550-235X. doi: 10.1103/PhysRevB.90.104108.

[39] Daniele Dragoni, Thomas D. Daff, Gábor Csányi, and Nicola Marzari. Achieving DFT accuracy with a machine-learning interatomic potential: Thermomechanics and defects in bcc ferromagnetic iron. *Phys. Rev. Mater.*, 2(1):013808, January 2018. ISSN 2475-9953. doi: 10.1103/PhysRevMaterials.2.013808.

[40] Chi Chen, Zhi Deng, Richard Tran, Hanmei Tang, Iek-Heng Chu, and Shyue Ping Ong. Accurate force field for molybdenum by machine learning large materials data. *Phys. Rev. Mater.*, 1(4):043603, September 2017. ISSN 2475-9953. doi: 10.1103/PhysRevMaterials.1.043603.

[41] Xiang-Guo Li, Chongze Hu, Chi Chen, Zhi Deng, Jian Luo, and Shyue Ping Ong. Quantum-accurate spectral neighbor analysis potential models for Ni-Mo binary alloys and fcc metals. *Phys. Rev. B*, 98(9):094104, September 2018. ISSN 2469-9950, 2469-9969. doi: 10.1103/PhysRevB.98.094104.

[42] Zhi Deng, Chi Chen, Xiang-Guo Li, and Shyue Ping Ong. An electrostatic spectral neighbor analysis potential for lithium nitride. *npj Comput. Mater.*, 5(1):75, December 2019. ISSN 2057-3960. doi: 10.1038/s41524-019-0212-1.

[43] Evgeny V. Podryabinkin and Alexander V. Shapeev. Active learning of linearly parametrized interatomic potentials. *Comput. Mater. Sci.*, 140:171–180, December 2017. ISSN 09270256. doi: 10.1016/j.commatsci.2017.08.031.

[44] Konstantin Gubaev, Evgeny V. Podryabinkin, Gus L. W. Hart, and Alexander V. Shapeev. Accelerating high-throughput searches for new alloys with active learning of interatomic potentials. *Comput. Mater. Sci.*, 156(24):148–156, 2019. doi: 10.1016/j.commatsci.2018.09.031.

[45] Linfeng Zhang, Jiequn Han, Han Wang, Roberto Car, and E Weinan. Deep potential molecular dynamics: a scalable model with the accuracy of quantum mechanics. *Physical review letters*, 120(14):143001, 2018. doi: 10.1103/PhysRevLett.120.143001.

[46] Vanessa Quaranta, Matti Hellström, and Jörg Behler. Proton-transfer mechanisms at the water–zno interface: the role of presolvation. *J. Phys. Chem. Lett.*, 8(7):1476–1483, 2017. doi: 10.1021/acs.jpclett.7b00358.

[47] Volker L Deringer, Noam Bernstein, Gábor Csányi, Chiheb Ben Mahmoud, Michele Ceriotti, Mark Wilson, David A Drabold, and Stephen R Elliott. Origins of structural and electronic transitions in disordered silicon. *Nature*, 589(7840):59–64, 2021. doi: 10.1038/s41586-020-03072-z.

[48] Chuhong Wang, Koutarou Aoyagi, Pandu Wisesa, and Tim Mueller. Lithium ion conduction in cathode coating materials from on-the-fly machine learning. *Chemistry of Materials*, 32(9):3741–3752, 2020. doi: 10.1021/acs.chemmater.9b04663.

[49] Artem R Oganov and Colin W Glass. Crystal structure prediction using ab initio evolutionary techniques: Principles and applications. *The Journal of chemical physics*, 124(24): 244704, 2006. doi: 10.1063/1.2210932.

[50] Yanchao Wang, Jian Lv, Li Zhu, and Yanming Ma. Crystal structure prediction via particle-swarm optimization. *Phys. Rev. B*, 82(9):094116, September 2010. ISSN 1098-0121, 1550-235X. doi: 10.1103/PhysRevB.82.094116.

[51] Geoffroy Hautier, Chris Fischer, Virginie Ehrlacher, Anubhav Jain, and Gerbrand Ceder. Data Mined Ionic Substitutions for the Discovery of New Compounds. *Inorg. Chem.*, 50 (2):656–663, January 2011. ISSN 0020-1669, 1520-510X. doi: 10.1021/ic102031h.

[52] Weike Ye, Chi Chen, Zhenbin Wang, Iek-Heng Chu, and Shyue Ping Ong. Deep neural networks for accurate predictions of crystal stability. *Nat Commun*, 9(1):3800, December 2018. ISSN 2041-1723. doi: 10.1038/s41467-018-06322-x.

[53] Jeff Greeley, Thomas F. Jaramillo, Jacob Bonde, Ib Chorkendorff, and Jens K. Nørskov. Computational high-throughput screening of electrocatalytic materials for hydrogen evolution. *Nature Mater*, 5(11):909–913, November 2006. ISSN 1476-1122, 1476-4660. doi: 10.1038/nmat1752.

[54] Yabi Wu, Predrag Lazic, Geoffroy Hautier, Kristin Persson, and Gerbrand Ceder. First principles high throughput screening of oxynitrides for water-splitting photocatalysts. *Energy & environmental science*, 6(1):157–168, 2013. doi: 10.1039/C2EE23482C.

[55] Juhwan Noh, Jaehoon Kim, Helge S. Stein, Benjamin Sanchez-Lengeling, John M. Gregoire, Alan Aspuru-Guzik, and Yousung Jung. Inverse Design of Solid-State Materials via a Continuous Representation. *Matter*, 1(5):1370–1384, November 2019. ISSN 25902385. doi: 10.1016/j.matt.2019.08.017.

[56] Sungwon Kim, Juhwan Noh, Geun Ho Gu, Alan Aspuru-Guzik, and Yousung Jung. Generative adversarial networks for crystal structure prediction. *ACS central science*, 6(8): 1412–1420, 2020. doi: 10.1021/acscentsci.0c00426.

[57] Anubhav Jain, Shyue Ping Ong, Geoffroy Hautier, Wei Chen, William Davidson Richards, Stephen Dacek, Shreyas Cholia, Dan Gunter, David Skinner, Gerbrand Ceder, and Kristin A. Persson. Commentary: The Materials Project: A materials genome approach to accelerating materials innovation. *APL Mater.*, 1(1):011002, July 2013. ISSN 2166-532X. doi: 10.1063/1.4812323.

[58] James E. Saal, Scott Kirklin, Muratahan Aykol, Bryce Meredig, and C. Wolverton. Materials Design and Discovery with High-Throughput Density Functional Theory: The Open Quantum Materials Database (OQMD). *JOM*, 65(11):1501–1509, November 2013. ISSN 1047-4838, 1543-1851. doi: 10.1007/s11837-013-0755-4.

[59] Stefano Curtarolo, Wahyu Setyawan, Shidong Wang, Junkai Xue, Kesong Yang, Richard H. Taylor, Lance J. Nelson, Gus L.W. Hart, Stefano Sanvito, Marco Buongiorno-Nardelli, Natalio Mingo, and Ohad Levy. AFLOWLIB.ORG: A distributed materials properties repository from high-throughput ab initio calculations. *Computational Materials Science*, 58:227–235, June 2012. ISSN 09270256. doi: 10.1016/j.commatsci.2012.02.002.

[60] Shyue Ping Ong, Lei Wang, Byoungwoo Kang, and Gerbrand Ceder. Li-Fe-P-O $_2$ Phase Diagram from First Principles Calculations. *Chem. Mater.*, 20(5):1798–1807, March 2008. ISSN 0897-4756, 1520-5002. doi: 10.1021/cm702327g.

[61] Wenhao Sun, Stephen T. Dacek, Shyue Ping Ong, Geoffroy Hautier, Anubhav Jain, William D. Richards, Anthony C. Gamst, Kristin A. Persson, and Gerbrand Ceder. The thermodynamic scale of inorganic crystalline metastability. *Sci. Adv.*, 2(11):e1600225, November 2016. ISSN 2375-2548. doi: 10.1126/sciadv.1600225.

[62] Rhys E. A. Goodall and Alpha A. Lee. Predicting materials properties without crystal structure: Deep representation learning from stoichiometry. *Nat Commun*, 11(1):6280, December 2020. ISSN 2041-1723. doi: 10.1038/s41467-020-19964-7.

[63] Dipendra Jha, Logan Ward, Arindam Paul, Wei-keng Liao, Alok Choudhary, Chris Wolverton, and Ankit Agrawal. ElemNet: Deep Learning the Chemistry of Materials From Only Elemental Composition. *Sci Rep*, 8(1):17593, December 2018. ISSN 2045-2322. doi: 10.1038/s41598-018-35934-y.

[64] Logan Ward, Ankit Agrawal, Alok Choudhary, and Christopher Wolverton. A general-purpose machine learning framework for predicting. *npj Comput. Mater.*, page 7, 2016. doi: 10.1038/npjcompumats.2016.28.

[65] Zonghan Wu, Shirui Pan, Fengwen Chen, Guodong Long, Chengqi Zhang, and S Yu Philip. A comprehensive survey on graph neural networks. *IEEE transactions on neural networks and learning systems*, 2020. doi: 10.1109/TNNLS.2020.2978386.

[66] Steven Kearnes, Kevin McCloskey, Marc Berndl, Vijay Pande, and Patrick Riley. Molecular graph convolutions: Moving beyond fingerprints. *J Comput Aided Mol Des*, 30(8):595–608, August 2016. ISSN 0920-654X, 1573-4951. doi: 10.1007/s10822-016-9938-8.

[67] Justin Gilmer, Samuel S Schoenholz, Patrick F Riley, Oriol Vinyals, and George E Dahl. Neural message passing for quantum chemistry. In *International Conference on Machine Learning*, pages 1263–1272. PMLR, 2017.

[68] Connor W. Coley, Regina Barzilay, William H. Green, Tommi S. Jaakkola, and Klavs F. Jensen. Convolutional Embedding of Attributed Molecular Graphs for Physical Property Prediction. *J. Chem. Inf. Model.*, 57(8):1757–1772, August 2017. ISSN 1549-9596, 1549-960X. doi: 10.1021/acs.jcim.6b00601.

[69] David Duvenaud, Dougal Maclaurin, Jorge Aguilera-Iparraguirre, Rafael Gomez-Bombarelli, Timothy Hirzel, Alan Aspuru-Guzik, and Ryan P Adams. Convolutional networks on graphs for learning molecular fingerprints. *Adv. Neural Info. Proces. Syst.*, 2: 2224–2232, 2015.

[70] K. T. Schütt, H. E. Sauceda, P.-J. Kindermans, A. Tkatchenko, and K.-R. Müller. SchNet – A deep learning architecture for molecules and materials. *The Journal of Chemical Physics*, 148(24):241722, June 2018. ISSN 0021-9606, 1089-7690. doi: 10.1063/1.5019779.

[71] Tian Xie and Jeffrey C. Grossman. Crystal Graph Convolutional Neural Networks for an Accurate and Interpretable Prediction of Material Properties. *Phys. Rev. Lett.*, 120(14): 145301, April 2018. ISSN 0031-9007, 1079-7114. doi: 10.1103/PhysRevLett.120.145301.

[72] Chi Chen, Weike Ye, Yunxing Zuo, Chen Zheng, and Shyue Ping Ong. Graph Networks as a Universal Machine Learning Framework for Molecules and Crystals. *Chem. Mater.*, 31 (9):3564–3572, May 2019. ISSN 0897-4756, 1520-5002. doi: 10.1021/acs.chemmater.9b 01294.

[73] L. J. Sham and M. Schlüter. Density-Functional Theory of the Energy Gap. *Phys. Rev. Lett.*, 51(20):1888–1891, November 1983. ISSN 0031-9007. doi: 10.1103/PhysRevLett.51.1888.

[74] Venkatesh Botu and Rampi Ramprasad. Adaptive machine learning framework to accelerate *ab initio* molecular dynamics. *Int. J. Quantum Chem.*, 115(16):1074–1083, August 2015. ISSN 00207608. doi: 10.1002/qua.24836.

[75] Zhenwei Li, James R. Kermode, and Alessandro De Vita. Molecular Dynamics with On-the-Fly Machine Learning of Quantum-Mechanical Forces. *Phys. Rev. Lett.*, 114(9):096405, March 2015. ISSN 0031-9007, 1079-7114. doi: 10.1103/PhysRevLett.114.096405.

[76] Matthias Rupp. Machine learning for quantum mechanics in a nutshell. *Int. J. Quantum Chem.*, 115(16):1058–1073, August 2015. ISSN 00207608. doi: 10.1002/qua.24954.

[77] Yufeng Huang, Jun Kang, William A. Goddard, and Lin-Wang Wang. Density functional theory based neural network force fields from energy decompositions. *Phys. Rev. B*, 99(6): 064103, February 2019. ISSN 2469-9950, 2469-9969. doi: 10.1103/PhysRevB.99.064103.

[78] Katja Hansen, Franziska Biegler, Raghunathan Ramakrishnan, Wiktor Pronobis, O. Anatole von Lilienfeld, Klaus-Robert Müller, and Alexandre Tkatchenko. Machine Learning Predictions of Molecular Properties: Accurate Many-Body Potentials and Nonlocality in Chemical Space. *J. Phys. Chem. Lett.*, 6(12):2326–2331, June 2015. ISSN 1948-7185. doi: 10.1021/acs.jpclett.5b00831.

[79] Matthias Rupp, Alexandre Tkatchenko, Klaus-Robert Müller, and O. Anatole von Lilienfeld. Fast and Accurate Modeling of Molecular Atomization Energies with Machine Learning. *Phys. Rev. Lett.*, 108(5):058301, January 2012. ISSN 0031-9007, 1079-7114. doi: 10.1103/PhysRevLett.108.058301.

[80] Thuong T. Nguyen, Eszter Székely, Giulio Imbalzano, Jörg Behler, Gábor Csányi, Michele Ceriotti, Andreas W. Götz, and Francesco Paesani. Comparison of permutationally invariant polynomials, neural networks, and Gaussian approximation potentials in representing water interactions through many-body expansions. *J. Chem. Phys.*, 148(24):241725, June 2018. ISSN 0021-9606, 1089-7690. doi: 10.1063/1.5024577.

[81] Lauri Himanen, Marc O.J. Jäger, Eiaki V. Morooka, Filippo Federici Canova, Yashasvi S. Ranawat, David Z. Gao, Patrick Rinke, and Adam S. Foster. DScribe: Library of descriptors for machine learning in materials science. *Computer Physics Communications*, 247:106949, February 2020. ISSN 00104655. doi: 10.1016/j.cpc.2019.106949.

[82] Chandramouli Nyshadham, Matthias Rupp, Brayden Bekker, Alexander V. Shapeev, Tim Mueller, Conrad W. Rosenbrock, Gábor Csányi, David W. Wingate, and Gus L. W. Hart. Machine-learned multi-system surrogate models for materials prediction. *npj Comput. Mater.*, 5(1):51, December 2019. ISSN 2057-3960. doi: 10.1038/s41524-019-0189-9.

[83] H. Balamane, T. Halicioglu, and W. A. Tiller. Comparative study of silicon empirical interatomic potentials. *Phys. Rev. B*, 46:2250–2279, Jul 1992. doi: 10.1103/PhysRevB.46.2250.

[84] DJ O'connor and JP Biersack. Comparison of theoretical and empirical interatomic potentials. *Nucl. Instrum. Methods Phys. Res., Sect. B*, 15(1-6):14–19, 1986. doi: 10.1016/0168-583X(86)90243-0.

[85] Julien Godet, Laurent Pizzagalli, Sandrine Brochard, and Pierre Beauchamp. Comparison between classical potentials and ab initio methods for silicon under large shear. *J. Phys.: Condens. Matter*, 15(41):6943, 2003. doi: 10.1088/0953-8984/15/41/004.

[86] Jörg Behler. Constructing high-dimensional neural network potentials: A tutorial review. *Int. J. Quantum Chem.*, 115(16):1032–1050, August 2015. ISSN 00207608. doi: 10.1002/qua.24890.

[87] Jörg Behler. First principles neural network potentials for reactive simulations of large molecular and condensed systems. *Angew. Chem., Int. Ed.*, 56(42):12828–12840, 2017. doi: 10.1002/anie.201703114.

[88] Felix C. Mocanu, Konstantinos Konstantinou, Tae Hoon Lee, Noam Bernstein, Volker L. Deringer, Gábor Csányi, and Stephen R. Elliott. Modeling the Phase-Change Memory Material, $Ge_2Sb_2Te_5$, with a Machine-Learned Interatomic Potential. *J. Phys. Chem. B*, 122(38):8998–9006, September 2018. ISSN 1520-6106, 1520-5207. doi: 10.1021/acs.jpcb.8b06476.

[89] M. A. Wood, M. A. Cusentino, B. D. Wirth, and A. P. Thompson. Data-driven material models for atomistic simulation. *Phys. Rev. B*, 99(18):184305, May 2019. ISSN 2469-9950, 2469-9969. doi: 10.1103/PhysRevB.99.184305.

[90] Nongnuch Artrith and Alexander Urban. An implementation of artificial neural-network potentials for atomistic materials simulations: Performance for TiO2. *Comput. Mater. Sci.*, 114:135–150, March 2016. ISSN 09270256. doi: 10.1016/j.commatsci.2015.11.047.

[91] Tobias Morawietz, Andreas Singraber, Christoph Dellago, and Jörg Behler. How van der waals interactions determine the unique properties of water. *Proc. Natl. Acad. Sci.*, 113(30):8368–8373, 2016. doi: 10.1073/pnas.1602375113.

[92] Marco Eckhoff and Jörg Behler. From molecular fragments to the bulk: Development of a neural network potential for mof-5. *J. Chem. Theory Comput.*, 2019. doi: 10.1021/acs.jctc.8b01288.

[93] Nongnuch Artrith, Tobias Morawietz, and Jörg Behler. High-dimensional neural-network potentials for multicomponent systems: Applications to zinc oxide. *Phys. Rev. B*, 83(15):153101, 2011. doi: 10.1103/PhysRevB.83.153101.

[94] Wenwen Li, Yasunobu Ando, Emi Minamitani, and Satoshi Watanabe. Study of Li atom diffusion in amorphous Li3PO4 with neural network potential. *J. Chem. Phys.*, 147(21):214106, December 2017. ISSN 0021-9606, 1089-7690. doi: 10.1063/1.4997242.

[95] Volker L. Deringer, Chris J. Pickard, and Gábor Csányi. Data-Driven Learning of Total and Local Energies in Elemental Boron. *Phys. Rev. Lett.*, 120(15):156001, April 2018. ISSN 0031-9007, 1079-7114. doi: 10.1103/PhysRevLett.120.156001.

[96] Patrick Rowe, Gábor Csányi, Dario Alfè, and Angelos Michaelides. Development of a machine learning potential for graphene. *Phys. Rev. B*, 97(5):054303, February 2018. ISSN 2469-9950, 2469-9969. doi: 10.1103/PhysRevB.97.054303.

[97] Volker L. Deringer, Noam Bernstein, Albert P. Bartók, Matthew J. Cliffe, Rachel N. Kerber, Lauren E. Marbella, Clare P. Grey, Stephen R. Elliott, and Gábor Csányi. Realistic Atomistic Structure of Amorphous Silicon from Machine-Learning-Driven Molecular Dynamics. *J. Phys. Chem. Lett.*, 9(11):2879–2885, June 2018. ISSN 1948-7185. doi: 10.1021/acs.jpclett.8b00902.

[98] Mitchell A. Wood and Aidan P. Thompson. Extending the accuracy of the SNAP interatomic potential form. *J. Chem. Phys.*, 148(24):241721, June 2018. ISSN 0021-9606, 1089-7690. doi: 10.1063/1.5017641.

[99] I.I. Novoselov, A.V. Yanilkin, A.V. Shapeev, and E.V. Podryabinkin. Moment tensor potentials as a promising tool to study diffusion processes. *Comput. Mater. Sci.*, 164:46–56, June 2019. ISSN 09270256. doi: 10.1016/j.commatsci.2019.03.049.

[100] Evgeny V Podryabinkin, Evgeny V Tikhonov, Alexander V Shapeev, and Artem R Oganov. Accelerating crystal structure prediction by machine-learning interatomic potentials with active learning. *Phys. Rev. B*, 99(6):064114, 2019. doi: 10.1103/PhysRevB.99.064114.

[101] Ivan S Novikov, Yury V Suleimanov, and Alexander V Shapeev. Automated calculation of thermal rate coefficients using ring polymer molecular dynamics and machine-learning interatomic potentials with active learning. *Phys. Chem. Chem. Phys.*, 20(46):29503–29512, 2018. doi: 10.1039/C8CP06037A.

[102] Maarten de Jong, Wei Chen, Thomas Angsten, Anubhav Jain, Randy Notestine, Anthony Gamst, Marcel Sluiter, Chaitanya Krishna Ande, Sybrand van der Zwaag, Jose J Plata, Cormac Toher, Stefano Curtarolo, Gerbrand Ceder, Kristin A. Persson, and Mark Asta. Charting the complete elastic properties of inorganic crystalline compounds. *Sci. Data*, 2: 150009, March 2015. ISSN 2052-4463. doi: 10.1038/sdata.2015.9.

[103] Richard Tran, Zihan Xu, Balachandran Radhakrishnan, Donald Winston, Wenhao Sun, Kristin A. Persson, and Shyue Ping Ong. Data Descriptor: Surface energies of elemental crystals. *Sci. Data*, 23:1–13, 2016. ISSN 20524463. doi: 10.1038/cgt.2016.38.

[104] Richard Tran and Shyue Ping Ong. An exploration of the grain boundaries, surfaces, and wulff shapes of the elements. http://crystalium.materialsvirtuallab.org/ (accessed 2016).

[105] G. Kresse and J. Furthmüller. Efficient iterative schemes for *ab initio* total-energy calculations using a plane-wave basis set. *Phys. Rev. B*, 54(16):11169–11186, October 1996. ISSN 0163-1829, 1095-3795. doi: 10.1103/PhysRevB.54.11169.

[106] P. E. Blöchl. Projector augmented-wave method. *Phys. Rev. B*, 50(24):17953–17979, December 1994. ISSN 0163-1829, 1095-3795. doi: 10.1103/PhysRevB.50.17953.

[107] John P. Perdew, Kieron Burke, and Matthias Ernzerhof. Generalized Gradient Approximation Made Simple. *Phys. Rev. Lett.*, 77(18):3865–3868, October 1996. ISSN 0031-9007, 1079-7114. doi: 10.1103/PhysRevLett.77.3865.

[108] Shyue Ping Ong, William Davidson Richards, Anubhav Jain, Geoffroy Hautier, Michael Kocher, Shreyas Cholia, Dan Gunter, Vincent L. Chevrier, Kristin A. Persson, and Gerbrand Ceder. Python Materials Genomics (pymatgen): A robust, open-source python library for materials analysis. *Comput. Mater. Sci.*, 68:314–319, February 2013. ISSN 09270256. doi: 10.1016/j.commatsci.2012.10.028.

[109] Anubhav Jain, Shyue Ping Ong, Wei Chen, Bharat Medasani, Xiaohui Qu, Michael Kocher, Miriam Brafman, Guido Petretto, Gian-Marco Rignanese, Geoffroy Hautier, Daniel Gunter, and Kristin A. Persson. FireWorks: A dynamic workflow system designed for high-throughput applications: FireWorks: A Dynamic Workflow System Designed for High-Throughput Applications. *Concurrency Computat.: Pract. Exp.*, 27(17):5037–5059, December 2015. ISSN 15320626. doi: 10.1002/cpe.3505.

[110] Byeong-Joo Lee, Jae-Hyeok Shim, and M. I. Baskes. Semiempirical atomic potentials for the fcc metals Cu, Ag, Au, Ni, Pd, Pt, Al, and Pb based on first and second nearest-neighbor modified embedded atom method. *Phys. Rev. B*, 68(14):144112, October 2003. ISSN 0163-1829, 1095-3795. doi: 10.1103/PhysRevB.68.144112.

[111] S. M. Foiles, M. I. Baskes, and M. S. Daw. Embedded-atom-method functions for the fcc metals Cu, Ag, Au, Ni, Pd, Pt, and their alloys. *Phys. Rev. B*, 33(12):7983–7991, June 1986. ISSN 0163-1829. doi: 10.1103/PhysRevB.33.7983.

[112] Y. Song, R. Yang, D. Li, W. T. Wu, and Z. X. Guo. Calculation of theoretical strengths and bulk moduli of bcc metals. *Phys. Rev. B*, 59(22):14220–14225, June 1999. ISSN 0163-1829, 1095-3795. doi: 10.1103/PhysRevB.59.14220.

[113] James B. Adams and Stephen M. Foiles. Development of an embedded-atom potential for a bcc metal: Vanadium. *Phys. Rev. B*, 41(6):3316–3328, February 1990. ISSN 0163-1829, 1095-3795. doi: 10.1103/PhysRevB.41.3316.

[114] Sandip De, Albert P. Bartók, Gábor Csányi, and Michele Ceriotti. Comparing molecules and solids across structural and alchemical space. *Phys. Chem. Chem. Phys.*, 18(20): 13754–13769, 2016. ISSN 1463-9076, 1463-9084. doi: 10.1039/C6CP00415F.

[115] M. I. Baskes, J. S. Nelson, and A. F. Wright. Semiempirical modified embedded-atom potentials for silicon and germanium. *Phys. Rev. B*, 40(9):6085–6100, September 1989. ISSN 0163-1829. doi: 10.1103/PhysRevB.40.6085.

[116] Andreas Singraber, Jörg Behler, and Christoph Dellago. Library-Based *LAMMPS* Implementation of High-Dimensional Neural Network Potentials. *J. Chem. Theory Comput.*, 15 (3):1827–1840, March 2019. ISSN 1549-9618, 1549-9626. doi: 10.1021/acs.jctc.8b00770.

[117] Yaolong Zhang, Ce Hu, and Bin Jiang. Embedded Atom Neural Network Potentials: Efficient and Accurate Machine Learning with a Physically Inspired Representation. *J. Phys. Chem. Lett.*, 10(17):4962–4967, September 2019. ISSN 1948-7185, 1948-7185. doi: 10.1021/acs.jpclett.9b02037.

[118] Jonathan Huang, Vivek Rathod, Chen Sun, Menglong Zhu, Anoop Korattikara, Alireza Fathi, Ian Fischer, Zbigniew Wojna, Yang Song, Sergio Guadarrama, and Kevin Murphy. Speed/Accuracy Trade-Offs for Modern Convolutional Object Detectors. *Proceedings of IEEE Conference on Computer Vision and Pattern Recognition*, pages 3296–3297, July 2017. doi: 10.1109/CVPR.2017.351.

[119] Linfeng Zhang, Jiequn Han, Han Wang, Wissam A Saidi, and Roberto Car. End-to-end Symmetry Preserving Inter-atomic Potential Energy Model for Finite and Extended Systems. *Proceedings of the 32nd International Conference on Neural Information Processing Systems; Curran Associates Inc.: Montreal, Canada*, pages 4441–4451, 2018.

[120] Bingqing Cheng, Edgar A. Engel, Jörg Behler, Christoph Dellago, and Michele Ceriotti. Ab initio thermodynamics of liquid and solid water. *Proc. Natl. Acad. Sci.*, 116(4):1110–1115, January 2019. ISSN 0027-8424, 1091-6490. doi: 10.1073/pnas.1815117116.

[121] X. W. Zhou, R. A. Johnson, and H. N. G. Wadley. Misfit-energy-increasing dislocations in vapor-deposited CoFe/NiFe multilayers. *Phys. Rev. B*, 69(14):144113, April 2004. ISSN 1098-0121, 1550-235X. doi: 10.1103/PhysRevB.69.144113.

[122] A. Nichol and G. J. Ackland. Property trends in simple metals: An empirical potential approach. *Phys. Rev. B*, 93:184101, May 2016. doi: 10.1103/PhysRevB.93.184101.

[123] Ebrahim Asadi, Mohsen Asle Zaeem, Sasan Nouranian, and Michael I. Baskes. Two-phase solid–liquid coexistence of Ni, Cu, and Al by molecular dynamics simulations using the modified embedded-atom method. *Acta Mater.*, 86:169–181, March 2015. ISSN 13596454. doi: 10.1016/j.actamat.2014.12.010.

[124] Hyoungki Park, Michael R. Fellinger, Thomas J. Lenosky, William W. Tipton, Dallas R. Trinkle, Sven P. Rudin, Christopher Woodward, John W. Wilkins, and Richard G. Hennig. *Ab Initio* based empirical potential used to study the mechanical properties of molybdenum. *Phys. Rev. B*, 85(21):214121, June 2012. ISSN 1098-0121, 1550-235X. doi: 10.1103/PhysRevB.85.214121.

[125] Thomas J Lenosky, Babak Sadigh, Eduardo Alonso, Vasily V Bulatov, Tomas Diaz de la Rubia, Jeongnim Kim, Arthur F Voter, and Joel D Kress. Highly optimized empirical potential model of silicon. *Modell. Simul. Mater. Sci. Eng.*, 8(6):825–841, oct 2000. doi: 10.1088/0965-0393/8/6/305.

[126] T. Kumagai, S. Izumi, S. Hara, and S. Sakai. Development of bond-order potentials that can reproduce the elastic constants and melting point of silicon for classical molecular dynamics simulation. *Comput. Mater. Sci.*, 39(2):457 – 464, 2007. ISSN 0927-0256. doi: 10.1016/j.commatsci.2006.07.013.

[127] Sayyed Jalil Mahdizadeh and Golnoosh Akhlamadi. Optimized tersoff empirical potential for germanene. *J. Mol. Graphics Modell.*, 72:1 – 5, 2017. ISSN 1093-3263. doi: 10.1016/j.jmgm.2016.11.009.

[128] Graeme Henkelman and Hannes Jónsson. Improved tangent estimate in the nudged elastic band method for finding minimum energy paths and saddle points. *J. Chem. Phys.*, 113 (22):9978–9985, 2000. doi: 10.1063/1.1323224.

[129] R Hill. The Elastic Behaviour of a Crystalline Aggregate. *Proc. Phys. Soc., London, Sect. A*, 65(5):349–354, May 1952. ISSN 0370-1298. doi: 10.1088/0370-1298/65/5/307.

[130] Søren L. Frederiksen and Karsten W. Jacobsen. Density functional theory studies of screw dislocation core structures in bcc metals. *Philos. Mag.*, 83(3):365–375, January 2003. ISSN 1478-6435, 1478-6443. doi: 10.1080/0141861021000034568.

[131] Yu-Min Juan and Efthimios Kaxiras. Generalized stacking fault energy surfaces and dislocation properties of silicon: A first-principles theoretical study. *Philos. Mag. A*, 74(6): 1367–1384, December 1996. ISSN 0141-8610, 1460-6992. doi: 10.1080/01418619608240729.

[132] Jonathan A Zimmerman, Huajian Gao, and Farid F Abraham. Generalized stacking fault energies for embedded atom FCC metals. *Modell. Simul. Mater. Sci. Eng.*, 8(2):103–115, March 2000. ISSN 0965-0393, 1361-651X. doi: 10.1088/0965-0393/8/2/302.

[133] A. Hunter, R. F. Zhang, and I. J. Beyerlein. The core structure of dislocations and their relationship to the material γ-surface. *J. Appl. Phys.*, 115(13):134314, April 2014. ISSN 0021-8979, 1089-7550. doi: 10.1063/1.4870462.

[134] K. Lejaeghere, V. Van Speybroeck, G. Van Oost, and S. Cottenier. Error Estimates for Solid-State Density-Functional Theory Predictions: An Overview by Means of the Ground-State Elemental Crystals. *Crit. Rev. Solid State Mater. Sci.*, 39(1):1–24, January 2014. ISSN 1040-8436, 1547-6561. doi: 10.1080/10408436.2013.772503.

[135] Gábor I. Csonka, John P. Perdew, Adrienn Ruzsinszky, Pier H. T. Philipsen, Sébastien Lebègue, Joachim Paier, Oleg A. Vydrov, and János G. Ángyán. Assessing the performance of recent density functionals for bulk solids. *Phys. Rev. B*, 79(15):155107, April 2009. ISSN 1098-0121, 1550-235X. doi: 10.1103/PhysRevB.79.155107.

[136] Viktor N. Staroverov, Gustavo E. Scuseria, Jianmin Tao, and John P. Perdew. Tests of a ladder of density functionals for bulk solids and surfaces. *Phys. Rev. B*, 69(7):075102, February 2004. ISSN 1098-0121, 1550-235X. doi: 10.1103/PhysRevB.69.075102.

[137] K. Lejaeghere, G. Bihlmayer, T. Bjorkman, P. Blaha, S. Blugel, V. Blum, D. Caliste, I. E. Castelli, S. J. Clark, A. Dal Corso, and et al. Reproducibility in density functional theory calculations of solids. *Science*, 351(6280):1–11, March 2016. ISSN 0036-8075, 1095-9203. doi: 10.1126/science.aad3000.

[138] Stefan Chmiela, Alexandre Tkatchenko, Huziel E. Sauceda, Igor Poltavsky, Kristof T. Schütt, and Klaus-Robert Müller. Machine learning of accurate energy-conserving molecular force fields. *Sci. Adv.*, 3(5):e1603015, May 2017. ISSN 2375-2548. doi: 10.1126/sciadv.1603015.

[139] Easo P. George, Dierk Raabe, and Robert O. Ritchie. High-entropy alloys. *Nat Rev Mater*, 4(8):515–534, August 2019. ISSN 2058-8437. doi: 10.1038/s41578-019-0121-4.

[140] Daniel B Miracle and Oleg N Senkov. A critical review of high entropy alloys and related concepts. *Acta Materialia*, 122:448–511, 2017. doi: 10.1016/j.actamat.2016.08.081.

[141] B. Cantor, I.T.H. Chang, P. Knight, and A.J.B. Vincent. Microstructural development in equiatomic multicomponent alloys. *Materials Science and Engineering: A*, 375-377: 213–218, July 2004. ISSN 09215093. doi: 10.1016/j.msea.2003.10.257.

[142] Zhiming Li, Konda Gokuldoss Pradeep, Yun Deng, Dierk Raabe, and Cemal Cem Tasan. Metastable high-entropy dual-phase alloys overcome the strength–ductility trade-off. *Nature*, 534(7606):227–230, June 2016. ISSN 0028-0836, 1476-4687. doi: 10.1038/nature17981.

[143] T. Yang, Y. L. Zhao, Y. Tong, Z. B. Jiao, J. Wei, J. X. Cai, X. D. Han, D. Chen, A. Hu, J. J. Kai, K. Lu, Y. Liu, and C. T. Liu. Multicomponent intermetallic nanoparticles and superb mechanical behaviors of complex alloys. *Science*, 362(6417):933–937, November 2018. ISSN 0036-8075, 1095-9203. doi: 10.1126/science.aas8815.

[144] B. Gludovatz, A. Hohenwarter, D. Catoor, E. H. Chang, E. P. George, and R. O. Ritchie. A fracture-resistant high-entropy alloy for cryogenic applications. *Science*, 345(6201): 1153–1158, September 2014. ISSN 0036-8075, 1095-9203. doi: 10.1126/science.1254581.

[145] Bernd Gludovatz, Anton Hohenwarter, Keli V. S. Thurston, Hongbin Bei, Zhenggang Wu, Easo P. George, and Robert O. Ritchie. Exceptional damage-tolerance of a medium-entropy alloy CrCoNi at cryogenic temperatures. *Nat Commun*, 7(1):10602, April 2016. ISSN 2041-1723. doi: 10.1038/ncomms10602.

[146] O.N. Senkov, G.B. Wilks, D.B. Miracle, C.P. Chuang, and P.K. Liaw. Refractory high-entropy alloys. *Intermetallics*, 18(9):1758–1765, September 2010. ISSN 09669795. doi: 10.1016/j.intermet.2010.05.014.

[147] O.N. Senkov, G.B. Wilks, J.M. Scott, and D.B. Miracle. Mechanical properties of Nb25Mo25Ta25W25 and V20Nb20Mo20Ta20W20 refractory high entropy alloys. *Intermetallics*, 19(5):698–706, May 2011. ISSN 09669795. doi: 10.1016/j.intermet.2011.01.004.

[148] Oleg N. Senkov, Daniel B. Miracle, Kevin J. Chaput, and Jean-Philippe Couzinie. Development and exploration of refractory high entropy alloys—A review. *J. Mater. Res.*, 33 (19):3092–3128, October 2018. ISSN 0884-2914, 2044-5326. doi: 10.1557/jmr.2018.153.

[149] Bronislava Gorr, Steven Schellert, Franz Müller, Hans-Jürgen Christ, Alexander Kauffmann, and Martin Heilmaier. Current Status of Research on the Oxidation Behavior of Refractory High Entropy Alloys. *Adv. Eng. Mater.*, page 2001047, February 2021. ISSN 1438-1656, 1527-2648. doi: 10.1002/adem.202001047.

[150] Zibing An, Shengcheng Mao, Tao Yang, Chain Tsuan Liu, Bin Zhang, Evan Ma, Hao Zhou, Ze Zhang, Lihua Wang, and Xiaodong Han. Spinodal-modulated solid solution delivers a strong and ductile refractory high-entropy alloy. *Mater. Horiz.*, 8(3):948–955, 2021. ISSN 2051-6347, 2051-6355. doi: 10.1039/D0MH01341B.

[151] Qi-Jun Hong, Jan Schroers, Douglas Hofmann, Stefano Curtarolo, Mark Asta, and Axel van de Walle. Theoretical prediction of high melting temperature for a Mo–Ru–Ta–W HCP multiprincipal element alloy. *npj Comput Mater*, 7(1):1, December 2021. ISSN 2057-3960. doi: 10.1038/s41524-020-00473-6.

[152] Michael A. Melia, Shaun R. Whetten, Raymond Puckett, Morgan Jones, Michael J. Heiden, Nicolas Argibay, and Andrew B. Kustas. High-throughput additive manufacturing and characterization of refractory high entropy alloys. *Applied Materials Today*, 19:100560, June 2020. ISSN 23529407. doi: 10.1016/j.apmt.2020.100560.

[153] Fulin Wang, Glenn H. Balbus, Shuozhi Xu, Yanqing Su, Jungho Shin, Paul F. Rottmann, Keith E. Knipling, Jean-Charles Stinville, Leah H. Mills, Oleg N. Senkov, Irene J. Beyerlein, Tresa M. Pollock, and Daniel S. Gianola. Multiplicity of dislocation pathways in a refractory multiprincipal element alloy. *Science*, 370(6512):95–101, October 2020. ISSN 0036-8075, 1095-9203. doi: 10.1126/science.aba3722.

[154] Shaolou Wei, Sang Jun Kim, Jiyun Kang, Yong Zhang, Yongjie Zhang, Tadashi Furuhara, Eun Soo Park, and Cemal Cem Tasan. Natural-mixing guided design of refractory high-entropy alloys with as-cast tensile ductility. *Nat. Mater.*, 19(11):1175–1181, November 2020. ISSN 1476-1122, 1476-4660. doi: 10.1038/s41563-020-0750-4.

[155] G. Dirras, J. Gubicza, A. Heczel, L. Lilensten, J.-P. Couzinié, L. Perrière, I. Guillot, and A. Hocini. Microstructural investigation of plastically deformed Ti20Zr20Hf20Nb20Ta20 high entropy alloy by X-ray diffraction and transmission electron microscopy. *Materials Characterization*, 108:1–7, October 2015. ISSN 10445803. doi: 10.1016/j.matchar.2015.08.007.

[156] L. Lilensten, J.-P. Couzinié, L. Perrière, A. Hocini, C. Keller, G. Dirras, and I. Guillot. Study of a bcc multi-principal element alloy: Tensile and simple shear properties and underlying deformation mechanisms. *Acta Materialia*, 142:131–141, January 2018. ISSN 13596454. doi: 10.1016/j.actamat.2017.09.062.

[157] J.-Ph. Couzinié, L. Lilensten, Y. Champion, G. Dirras, L. Perrière, and I. Guillot. On the room temperature deformation mechanisms of a TiZrHfNbTa refractory high-entropy alloy. *Materials Science and Engineering: A*, 645:255–263, October 2015. ISSN 09215093. doi: 10.1016/j.msea.2015.08.024.

[158] Francesco Maresca and William A Curtin. Mechanistic origin of high strength in refractory bcc high entropy alloys up to 1900k. *Acta Materialia*, 182:235–249, 2020. doi: 10.1016/j.actamat.2019.10.015.

[159] Wu-Rong Jian, Zhuocheng Xie, Shuozhi Xu, Yanqing Su, Xiaohu Yao, and Irene J. Beyerlein. Effects of lattice distortion and chemical short-range order on the mechanisms of deformation in medium entropy alloy CoCrNi. *Acta Materialia*, 199:352–369, October 2020. ISSN 13596454. doi: 10.1016/j.actamat.2020.08.044.

[160] S.I. Rao, B. Akdim, E. Antillon, C. Woodward, T.A. Parthasarathy, and O.N. Senkov. Modeling solution hardening in BCC refractory complex concentrated alloys: NbTiZr, Nb1.5TiZr0.5 and Nb0.5TiZr1.5. *Acta Materialia*, 168:222–236, April 2019. ISSN 13596454. doi: 10.1016/j.actamat.2019.02.013.

[161] Shuozhi Xu, Yanqing Su, Wu-Rong Jian, and Irene J. Beyerlein. Local slip resistances in equal-molar MoNbTi multi-principal element alloy. *Acta Materialia*, 202:68–79, January 2021. ISSN 13596454. doi: 10.1016/j.actamat.2020.10.042.

[162] Sheng Yin, Jun Ding, Mark Asta, and Robert O. Ritchie. Ab initio modeling of the energy landscape for screw dislocations in body-centered cubic high-entropy alloys. *npj Comput Mater*, 6(1):110, December 2020. ISSN 2057-3960. doi: 10.1038/s41524-020-00377-5.

[163] A. Fernández-Caballero, J. S. Wróbel, P. M. Mummery, and D. Nguyen-Manh. Short-Range Order in High Entropy Alloys: Theoretical Formulation and Application to Mo-Nb-Ta-V-W System. *J. Phase Equilib. Diffus.*, 38(4):391–403, August 2017. ISSN 1547-7037, 1863-7345. doi: 10.1007/s11669-017-0582-3.

[164] William Paul Huhn and Michael Widom. Prediction of A2 to B2 Phase Transition in the High-Entropy Alloy Mo-Nb-Ta-W. *JOM*, 65(12):1772–1779, December 2013. ISSN 1047-4838, 1543-1851. doi: 10.1007/s11837-013-0772-3.

[165] Fritz Körmann, Andrei V. Ruban, and Marcel H.F. Sluiter. Long-ranged interactions in bcc NbMoTaW high-entropy alloys. *Materials Research Letters*, 5(1):35–40, January 2017. ISSN 2166-3831. doi: 10.1080/21663831.2016.1198837.

[166] Tatiana Kostiuchenko, Andrei V. Ruban, Jörg Neugebauer, Alexander Shapeev, and Fritz Körmann. Short-range order in face-centered cubic VCoNi alloys. *Phys. Rev. Materials*, 4 (11):113802, November 2020. ISSN 2475-9953. doi: 10.1103/PhysRevMaterials.4.113802.

[167] Yue Ma, Qing Wang, Chunling Li, Louis J. Santodonato, Mikhail Feygenson, Chuang Dong, and Peter K. Liaw. Chemical short-range orders and the induced structural transition in high-entropy alloys. *Scripta Materialia*, 144:64–68, February 2018. ISSN 13596462. doi: 10.1016/j.scriptamat.2017.09.049.

[168] Artur Tamm, Alvo Aabloo, Mattias Klintenberg, Malcolm Stocks, and Alfredo Caro. Atomic-scale properties of Ni-based FCC ternary, and quaternary alloys. *Acta Materialia*, 99:307–312, October 2015. ISSN 13596454. doi: 10.1016/j.actamat.2015.08.015.

[169] Flynn Walsh, Mark Asta, and Robert O. Ritchie. Magnetically driven short-range order can explain anomalous measurements in CrCoNi. *Proc Natl Acad Sci USA*, 118(13): e2020540118, March 2021. ISSN 0027-8424, 1091-6490. doi: 10.1073/pnas.2020540118.

[170] F. X. Zhang, Shijun Zhao, Ke Jin, H. Xue, G. Velisa, H. Bei, R. Huang, J. Y. P. Ko, D. C. Pagan, J. C. Neuefeind, W. J. Weber, and Yanwen Zhang. Local Structure and Short-Range Order in a NiCoCr Solid Solution Alloy. *Phys. Rev. Lett.*, 118(20):205501, May 2017. ISSN 0031-9007, 1079-7114. doi: 10.1103/PhysRevLett.118.205501.

[171] E. Antillon, C. Woodward, S.I. Rao, B. Akdim, and T.A. Parthasarathy. Chemical short range order strengthening in a model FCC high entropy alloy. *Acta Materialia*, 190:29–42, May 2020. ISSN 13596454. doi: 10.1016/j.actamat.2020.02.041.

[172] Jun Ding, Qin Yu, Mark Asta, and Robert O. Ritchie. Tunable stacking fault energies by tailoring local chemical order in CrCoNi medium-entropy alloys. *Proc Natl Acad Sci USA*, 115(36):8919–8924, September 2018. ISSN 0027-8424, 1091-6490. doi: 10.1073/pnas.1808660115.

[173] Ruopeng Zhang, Shiteng Zhao, Colin Ophus, Yu Deng, Shraddha J. Vachhani, Burak Ozdol, Rachel Traylor, Karen C. Bustillo, J. W. Morris, Daryl C. Chrzan, Mark Asta, and Andrew M. Minor. Direct imaging of short-range order and its impact on deformation in Ti-6Al. *Sci. Adv.*, 5(12):eaax2799, December 2019. ISSN 2375-2548. doi: 10.1126/sciadv.aax2799.

[174] Gordon E. Lakso and M. J. Marcinkowski. Plastic deformation in Fe-Si alloys. *MT*, 5(4): 839–845, April 1974. ISSN 0360-2133, 1543-1916. doi: 10.1007/BF02643136.

[175] Ruopeng Zhang, Shiteng Zhao, Jun Ding, Yan Chong, Tao Jia, Colin Ophus, Mark Asta, Robert O. Ritchie, and Andrew M. Minor. Short-range order and its impact on the CrCoNi medium-entropy alloy. *Nature*, 581(7808):283–287, May 2020. ISSN 0028-0836, 1476-4687. doi: 10.1038/s41586-020-2275-z.

[176] Xuefei Chen, Qi Wang, Zhiying Cheng, Mingliu Zhu, Hao Zhou, Ping Jiang, Lingling Zhou, Qiqi Xue, Fuping Yuan, Jing Zhu, Xiaolei Wu, and En Ma. Direct observation of chemical short-range order in a medium-entropy alloy. *Nature*, 592(7856):712–716, April 2021. ISSN 0028-0836, 1476-4687. doi: 10.1038/s41586-021-03428-z.

[177] Tatiana Kostiuchenko, Fritz Körmann, Jörg Neugebauer, and Alexander Shapeev. Impact of lattice relaxations on phase transitions in a high-entropy alloy studied by machine-learning potentials. *npj Comput Mater*, 5(1):55, December 2019. ISSN 2057-3960. doi: 10.1038/s41524-019-0195-y.

[178] J. M. Cowley. An Approximate Theory of Order in Alloys. *Phys. Rev.*, 77(5):669–675, March 1950. ISSN 0031-899X. doi: 10.1103/PhysRev.77.669.

[179] Alexander Stukowski. Visualization and analysis of atomistic simulation data with OVITO–the Open Visualization Tool. *Modelling Simul. Mater. Sci. Eng.*, 18(1):015012, January 2010. ISSN 0965-0393, 1361-651X. doi: 10.1088/0965-0393/18/1/015012.

[180] Ryan B. Sills, Michael E. Foster, and Xiaowang W. Zhou. Line-length-dependent dislocation mobilities in an FCC stainless steel alloy. *International Journal of Plasticity*, 135: 102791, December 2020. ISSN 07496419. doi: 10.1016/j.ijplas.2020.102791.

[181] Francesco Maresca, Daniele Dragoni, Gábor Csányi, Nicola Marzari, and William A. Curtin. Screw dislocation structure and mobility in body centered cubic Fe predicted by a Gaussian Approximation Potential. *npj Comput Mater*, 4(1):69, December 2018. ISSN 2057-3960. doi: 10.1038/s41524-018-0125-4.

[182] J.C. Fisher. On the strength of solid solution alloys. *Acta Metallurgica*, 2(1):9–10, January 1954. ISSN 00016160. doi: 10.1016/0001-6160(54)90087-5.

[183] Wei Cai, Vasily V Bulatov, Jinpeng Chang, Ju Li, and Sidney Yip. Dislocation core effects on mobility. *Dislocations in solids*, 12:1–80, 2004.

[184] John E Dora and Stanley Rajnak. Nucleation of kink pairs and the peierls'mechanism of plastic deformation. *Trans. AIME*, 1963.

[185] Wei Cai, Vasily V Bulatov, Sidney Yip, and Ali S Argon. Kinetic Monte Carlo modeling of dislocation motion in BCC metals. *Materials Science and Engineering: A*, 309-310: 270–273, July 2001. ISSN 09215093. doi: 10.1016/S0921-5093(00)01689-0.

[186] P. B. Hirsch. A new theory of the anomalous yield stress in l12 alloys. *Phil. Mag. A*, 65(3): 569–612, March 1992. ISSN 0141-8610. doi: 10.1080/01418619208201539.

[187] D. C. Chrzan and Murray S. Daw. Pinning-depinning transition in dislocation dynamics. *Phys. Rev. B*, 55(2):798–811, January 1997. ISSN 0163-1829, 1095-3795. doi: 10.1103/PhysRevB.55.798.

[188] S.I. Rao, C. Varvenne, C. Woodward, T.A. Parthasarathy, D. Miracle, O.N. Senkov, and W.A. Curtin. Atomistic simulations of dislocations in a model BCC multicomponent concentrated solid solution alloy. *Acta Materialia*, 125:311–320, February 2017. ISSN 13596454. doi: 10.1016/j.actamat.2016.12.011.

[189] Giacomo Po, Yinan Cui, David Rivera, David Cereceda, Tom D. Swinburne, Jaime Marian, and Nasr Ghoniem. A phenomenological dislocation mobility law for bcc metals. *Acta Materialia*, 119:123–135, October 2016. ISSN 13596454. doi: 10.1016/j.actamat.2016.08.016.

[190] UF Kocks. Termodynamics and kinetics of slip. *Prog. in Mater. Sci.*, 242, 1975.

[191] David L Olmsted, Louis G HectorJr, W A Curtin, and R J Clifton. Atomistic simulations of dislocation mobility in Al, Ni and Al/Mg alloys. *Modelling Simul. Mater. Sci. Eng.*, 13(3): 371–388, April 2005. ISSN 0965-0393, 1361-651X. doi: 10.1088/0965-0393/13/3/007.

[192] J. Marian and A. Caro. Moving dislocations in disordered alloys: Connecting continuum and discrete models with atomistic simulations. *Phys. Rev. B*, 74(2):024113, July 2006. ISSN 1098-0121, 1550-235X. doi: 10.1103/PhysRevB.74.024113.

[193] Chanho Lee, Gian Song, Michael C. Gao, Rui Feng, Peiyong Chen, Jamieson Brechtl, Yan Chen, Ke An, Wei Guo, Jonathan D. Poplawsky, Song Li, A.T. Samaei, Wei Chen, Alice Hu, Hahn Choo, and Peter K. Liaw. Lattice distortion in a strong and ductile refractory high-entropy alloy. *Acta Materialia*, 160:158–172, November 2018. ISSN 13596454. doi: 10.1016/j.actamat.2018.08.053.

[194] A. Lawley and H. L. Gaigher. Deformation structures in zone-melted molybdenum. *Philosophical Magazine*, 10(103):15–33, July 1964. ISSN 0031-8086. doi: 10.1080/14786436408224204.

[195] F. Louchet, L. P. Kubin, and D. Vesely. In situ deformation of b.c.c. crystals at low temperatures in a high-voltage electron microscope Dislocation mechanisms and strain-rate equation. *Philosophical Magazine A*, 39(4):433–454, April 1979. ISSN 0141-8610, 1460-6992. doi: 10.1080/01418617908239283.

[196] Bing Chen, Suzhi Li, Hongxiang Zong, Xiangdong Ding, Jun Sun, and Evan Ma. Unusual activated processes controlling dislocation motion in body-centered-cubic high-entropy alloys. *Proc Natl Acad Sci USA*, 117(28):16199–16206, July 2020. ISSN 0027-8424, 1091-6490. doi: 10.1073/pnas.1919136117.

[197] Romain Gautier, Xiuwen Zhang, Linhua Hu, Liping Yu, Yuyuan Lin, Tor O. L. Sunde, Danbee Chon, Kenneth R. Poeppelmeier, and Alex Zunger. Prediction and accelerated laboratory discovery of previously unknown 18-electron ABX compounds. *Nature Chem*, 7(4):308–316, April 2015. ISSN 1755-4330, 1755-4349. doi: 10.1038/nchem.2207.

[198] Qimin Yan, Jie Yu, Santosh K. Suram, Lan Zhou, Aniketa Shinde, Paul F. Newhouse, Wei Chen, Guo Li, Kristin A. Persson, John M. Gregoire, and Jeffrey B. Neaton. Solar fuels photoanode materials discovery by integrating high-throughput theory and experiment. *Proc Natl Acad Sci USA*, 114(12):3040–3043, March 2017. ISSN 0027-8424, 1091-6490. doi: 10.1073/pnas.1619940114.

[199] Zhenbin Wang, Jungmin Ha, Yoon Hwa Kim, Won Bin Im, Joanna McKittrick, and Shyue Ping Ong. Mining Unexplored Chemistries for Phosphors for High-Color-Quality White-Light-Emitting Diodes. *Joule*, 2(5):914–926, May 2018. ISSN 25424351. doi: 10.1016/j.joule.2018.01.015.

[200] Atsuto Seko, Atsushi Togo, Hiroyuki Hayashi, Koji Tsuda, Laurent Chaput, and Isao Tanaka. Prediction of Low-Thermal-Conductivity Compounds with First-Principles Anharmonic Lattice-Dynamics Calculations and Bayesian Optimization. *Phys. Rev. Lett.*, 115 (20):205901, November 2015. ISSN 0031-9007, 1079-7114. doi: 10.1103/PhysRevLett.115.205901.

[201] Dezhen Xue, Prasanna V. Balachandran, John Hogden, James Theiler, Deqing Xue, and Turab Lookman. Accelerated search for materials with targeted properties by adaptive design. *Nat Commun*, 7(1):11241, September 2016. ISSN 2041-1723. doi: 10.1038/ncomms11241.

[202] Felix A. Faber, Alexander Lindmaa, O. Anatole von Lilienfeld, and Rickard Armiento. Machine Learning Energies of 2 Million Elpasolite (A B C 2 D 6) Crystals. *Phys. Rev. Lett.*, 117(13):135502, September 2016. ISSN 0031-9007, 1079-7114. doi: 10.1103/PhysRevLett.117.135502.

[203] Benjamin Sanchez-Lengeling and Alán Aspuru-Guzik. Inverse molecular design using machine learning: Generative models for matter engineering. *Science*, 361(6400):360–365, July 2018. ISSN 0036-8075, 1095-9203. doi: 10.1126/science.aat2663.

[204] Jonathan Schmidt, Mário R. G. Marques, Silvana Botti, and Miguel A. L. Marques. Recent advances and applications of machine learning in solid-state materials science. *npj Comput Mater*, 5(1):83, December 2019. ISSN 2057-3960. doi: 10.1038/s41524-019-0221-0.

[205] Baekjun Kim, Sangwon Lee, and Jihan Kim. Inverse design of porous materials using artificial neural networks. *Sci. Adv.*, 6(1):eaax9324, January 2020. ISSN 2375-2548. doi: 10.1126/sciadv.aax9324.

[206] Chi Chen, Yunxing Zuo, Weike Ye, Xiangguo Li, and Shyue Ping Ong. Learning properties of ordered and disordered materials from multi-fidelity data. *Nat Comput Sci*, 1(1):46–53, January 2021. ISSN 2662-8457. doi: 10.1038/s43588-020-00002-x.

[207] Peter Bjørn Jørgensen, Karsten Wedel Jacobsen, and Mikkel N. Schmidt. Neural Message Passing with Edge Updates for Predicting Properties of Molecules and Materials. *ArXiv180603146 Cs Stat*, June 2018.

[208] K. T. Schütt, P. Kessel, M. Gastegger, K. A. Nicoli, A. Tkatchenko, and K.-R. Müller. SchNetPack: A Deep Learning Toolbox For Atomistic Systems. *J. Chem. Theory Comput.*, 15(1):448–455, January 2019. ISSN 1549-9618, 1549-9626. doi: 10.1021/acs.jctc.8b00908.

[209] Gowoon Cheon, Lusann Yang, Kevin McCloskey, Evan J. Reed, and Ekin D. Cubuk. Crystal Structure Search with Random Relaxations Using Graph Networks. *ArXiv201202920 Cond-Mat Physicsphysics*, December 2020.

[210] Colin W. Glass, Artem R. Oganov, and Nikolaus Hansen. USPEX—Evolutionary crystal structure prediction. *Computer Physics Communications*, 175(11-12):713–720, December 2006. ISSN 00104655. doi: 10.1016/j.cpc.2006.07.020.

[211] Maja-Olivia Lenz, Thomas A. R. Purcell, David Hicks, Stefano Curtarolo, Matthias Scheffler, and Christian Carbogno. Parametrically constrained geometry relaxations for high-throughput materials science. *npj Comput Mater*, 5(1):123, December 2019. ISSN 2057-3960. doi: 10.1038/s41524-019-0254-4.

[212] Atsushi Togo and Isao Tanaka. Spglib: A software library for crystal symmetry search. *ArXiv180801590 Cond-Mat*, August 2018.

[213] Turab Lookman, Prasanna V. Balachandran, Dezhen Xue, and Ruihao Yuan. Active learning in materials science with emphasis on adaptive sampling using uncertainties for targeted design. *npj Comput Mater*, 5(1):21, December 2019. ISSN 2057-3960. doi: 10.1038/s41524-019-0153-8.

[214] Carl Edward Rasmussen and Christopher K. I. Williams. *Gaussian Processes for Machine Learning*. Adaptive Computation and Machine Learning. MIT Press, Cambridge, Mass, 2006. ISBN 978-0-262-18253-9.

[215] Ruben Martinez-Cantin, Nando de Freitas, Eric Brochu, José Castellanos, and Arnaud Doucet. A Bayesian exploration-exploitation approach for optimal online sensing and planning with a visually guided mobile robot. *Auton Robot*, 27(2):93–103, August 2009. ISSN 0929-5593, 1573-7527. doi: 10.1007/s10514-009-9130-2.

[216] Bobak Shahriari, Kevin Swersky, Ziyu Wang, Ryan P. Adams, and Nando de Freitas. Taking the Human Out of the Loop: A Review of Bayesian Optimization. *Proc. IEEE*, 104(1): 148–175, January 2016. ISSN 0018-9219, 1558-2256. doi: 10.1109/JPROC.2015.2494218.

[217] Prasanna V. Balachandran, Dezhen Xue, James Theiler, John Hogden, and Turab Lookman. Adaptive Strategies for Materials Design using Uncertainties. *Sci Rep*, 6(1):19660, April 2016. ISSN 2045-2322. doi: 10.1038/srep19660.

[218] Donald R Jones, Matthias Schonlau, and William J Welch. Efficient global optimization of expensive black-box functions. *Journal of Global optimization*, 13(4):455–492, 1998. doi: 10.1023/A:1008306431147.

[219] Turab Lookman, Francis J. Alexander, and Krishna Rajan, editors. *Information Science for Materials Discovery and Design*, volume 225 of *Springer Series in Materials Science*. Springer International Publishing, Cham, 2016. ISBN 978-3-319-23870-8 978-3-319-23871-5. doi: 10.1007/978-3-319-23871-5.

[220] Maarten de Jong, Wei Chen, Thomas Angsten, Anubhav Jain, Randy Notestine, Anthony Gamst, Marcel Sluiter, Chaitanya Krishna Ande, Sybrand van der Zwaag, Jose J Plata, Cormac Toher, Stefano Curtarolo, Gerbrand Ceder, Kristin A. Persson, and Mark Asta. Charting the complete elastic properties of inorganic crystalline compounds. *Sci Data*, 2 (1):150009, December 2015. ISSN 2052-4463. doi: 10.1038/sdata.2015.9.

[221] G. Bergerhoff, R. Hundt, R. Sievers, and I. D. Brown. The inorganic crystal structure data base. *J. Chem. Inf. Model.*, 23(2):66–69, May 1983. ISSN 1549-9596. doi: 10.1021/ci00038a003.

[222] Alec Belsky, Mariette Hellenbrandt, Vicky Lynn Karen, and Peter Luksch. New developments in the Inorganic Crystal Structure Database (ICSD): Accessibility in support of materials research and design. *Acta Cryst Sect A Found Cryst*, 58(3):364–369, June 2002. ISSN 0108-7681. doi: 10.1107/S0108768102006948.

[223] Georgiy Akopov, Michael T. Yeung, and Richard B. Kaner. Rediscovering the Crystal Chemistry of Borides. *Adv. Mater.*, 29(21):1604506, June 2017. ISSN 09359648. doi: 10.1002/adma.201604506.

[224] Michael T. Yeung, Reza Mohammadi, and Richard B. Kaner. Ultraincompressible, Superhard Materials. *Annu. Rev. Mater. Res.*, 46(1):465–485, July 2016. ISSN 1531-7331, 1545-4118. doi: 10.1146/annurev-matsci-070115-032148.

[225] H. B. Huntington. Ultrasonic Measurements on Single Crystals. *Phys. Rev.*, 72(4):321–331, August 1947. ISSN 0031-899X. doi: 10.1103/PhysRev.72.321.

[226] David Lazarus. The Variation of the Adiabatic Elastic Constants of KCl, NaCl, CuZn, Cu, and Al with Pressure to 10,000 Bars. *Phys. Rev.*, 76(4):545–553, August 1949. ISSN 0031-899X. doi: 10.1103/PhysRev.76.545.

[227] Xing-Qiu Chen, Haiyang Niu, Dianzhong Li, and Yiyi Li. Intrinsic Correlation between Hardness and Elasticity in Polycrystalline Materials and Bulk Metallic Glasses. *Intermetallics*, 19(9):1275–1281, September 2011. ISSN 09669795. doi: 10.1016/j.intermet.2011.03.026.

[228] G. Pilania, J.E. Gubernatis, and T. Lookman. Multi-fidelity machine learning models for accurate bandgap predictions of solids. *Computational Materials Science*, 129:156–163, March 2017. ISSN 09270256. doi: 10.1016/j.commatsci.2016.12.004.

[229] Dipendra Jha, Kamal Choudhary, Francesca Tavazza, Wei-keng Liao, Alok Choudhary, Carelyn Campbell, and Ankit Agrawal. Enhancing materials property prediction by leveraging computational and experimental data using deep transfer learning. *Nat Commun*, 10(1):5316, December 2019. ISSN 2041-1723. doi: 10.1038/s41467-019-13297-w.

[230] J Trivisonno, S Vatanayon, M Wilt, J Washick, and R Reifenberger. Temperature dependence of the elastic constants of niobium and lead in the normal and superconducting states. *Journal of Low Temperature Physics*, 12(1):153–169, 1973. doi: 10.1007/BF00654733.

[231] Gene Simmons. Single crystal elastic constants and calculated aggregate properties. Technical report, Southern Methodist Univ Dallas Tex, 1965.

[232] Frank H Featherston and JR Neighbours. Elastic constants of tantalum, tungsten, and molybdenum. *Phys. Rev.*, 130(4):1324, 1963. doi: 10.1103/PhysRev.130.1324.

[233] Z. Ban and M. Sikirica. The crystal structure of ternary silicides ThM $_2$ Si $_2$ (M = Cr, Mn, Fe, Co, Ni and Cu). *Acta Cryst*, 18(4):594–599, April 1965. ISSN 0365-110X. doi: 10.1107/S0365110X6500141X.

[234] C. B. Shoemaker and D. P. Shoemaker. A ternary alloy with PbCl2-type structure: TiNiSi(E). *Acta Cryst*, 18(5):900–905, May 1965. ISSN 0365110X. doi: 10.1107/S0365110X65002189.

[235] A. E. Dwight, M. H. Mueller, R. Conner, J. W. Downey, and H. Knott. Ternary compounds with the fe$_2$p-type structure. *Trans. Metall. Soc. AIME*, 242(4):10, August 1968.